

Numerical modelling of fatigue crack propagation and stress-assisted pitting corrosion

Dekker, R.

DOI

[10.4233/uuid:da88e4d8-035b-4e69-806c-6909411d19b3](https://doi.org/10.4233/uuid:da88e4d8-035b-4e69-806c-6909411d19b3)

Publication date

2021

Document Version

Final published version

Citation (APA)

Dekker, R. (2021). *Numerical modelling of fatigue crack propagation and stress-assisted pitting corrosion*. [Dissertation (TU Delft), Delft University of Technology]. <https://doi.org/10.4233/uuid:da88e4d8-035b-4e69-806c-6909411d19b3>

Important note

To cite this publication, please use the final published version (if applicable). Please check the document version above.

Copyright

Other than for strictly personal use, it is not permitted to download, forward or distribute the text or part of it, without the consent of the author(s) and/or copyright holder(s), unless the work is under an open content license such as Creative Commons.

Takedown policy

Please contact us and provide details if you believe this document breaches copyrights. We will remove access to the work immediately and investigate your claim.

Numerical modelling of fatigue crack propagation and stress-assisted pitting corrosion

Richard Dekker

Numerical modelling of fatigue crack propagation and stress-assisted pitting corrosion

Proefschrift

ter verkrijging van de graad van doctor
aan de Technische Universiteit Delft,
op gezag van de Rector Magnificus prof. dr. ir. T.H.J.J. van der Hagen,
voorzitter van het College voor Promoties,
in het openbaar te verdedigen op
maandag 27 september 2021 om 12:30 uur

door

Richard Dekker

Ingenieur Lucht- en Ruimtevaart
Technische Universiteit Delft, Nederland
geboren te Katwijk, Nederland

Dit proefschrift is goedgekeurd door de

promotor: prof. dr. ir. L.J. Sluys
promotor: prof. dr. ir. J. Maljaars
copromotor: dr. ir. F.P. van der Meer

Samenstelling promotiecommissie:

Rector Magnificus,	voorzitter
Prof. dr. ir. L.J. Sluys,	Technische Universiteit Delft
Prof. dr. ir. J. Maljaars,	Technische Universiteit Eindhoven
Dr. ir. F.P. van der Meer,	Technische Universiteit Delft

Onafhankelijke leden:

Prof. dr. A. Metrikine,	Technische Universiteit Delft
Prof. dr. ir. J.M.C Mol,	Technische Universiteit Delft
Prof. ir. H.H. Snijder,	Technische Universiteit Eindhoven
Prof. dipl.-ing dr. C. Hellmich	Technische Universität Wien



Cover photo: Janine van Duijn

Printer: Optima, Rotterdam, The Netherlands

Copyright © 2021 by Richard Dekker

This research is part of the EUROS program, which is supported by NWO domain Applied and Engineering Sciences and partly funded by the Dutch Ministry of Economic Affairs.

ISBN 978-94-6361-598-3

An electronic version of this dissertation is available at
<http://repository.tudelft.nl/>.

"It's the questions we can't answer that teach us the most. They teach us how to think. If you give a man an answer, all he gains is a little fact. But give him a question and he'll look for his own answers."

Patrick Rothfuss, *The Wise Man's Fear*

Contents

Summary	xi
Samenvatting	xiii
1 General Introduction	1
1 Societal background	2
2 Research scope and goal	3
3 Thesis outline	4
References	6
2 A cohesive XFEM model for simulating fatigue crack growth	9
1 Introduction	11
2 Numerical framework.	13
2.1 Phantom node technique	14
2.2 Adaptive meshing	14
3 Material behaviour	15
3.1 Bulk material.	16
3.2 Cohesive zone model	16
3.3 Interfacial thick level set	18
3.4 Fatigue crack relation	19
4 Crack tip propagation.	19
4.1 Numerical crack tip	20
4.2 Physical crack tip	21

5	Numerical examples	22
5.1	Mode I linear elastic	23
5.2	Mixed-mode linear elastic	25
5.3	Mode I elastic plastic.	26
6	Conclusions.	29
	References	31
3	A model for simulating fatigue crack growth under various load conditions	37
1	Introduction	39
2	Numerical framework.	40
3	Material behaviour	41
3.1	Bulk material.	41
3.2	Cohesive zone model	41
3.3	Fatigue crack relation	43
4	Crack tip propagation.	44
5	Model calibration	46
5.1	Cohesive stiffness	47
5.2	Critical energy release rate	47
5.3	Tensile strength and Paris parameters	48
6	Validation	50
6.1	Constant amplitude loading	50
6.2	Biaxial loading with a single overload	55
7	Conclusions.	56
	References	57
4	A level set model for stress-dependent corrosion pit propagation	61
1	Introduction	63
2	Problem description	64

3	Mechanical behaviour	65
4	Corrosion behaviour	66
4.1	Activation control	66
4.2	Diffusion control.	68
4.3	Passivation.	69
5	Numerical framework.	69
5.1	Level set update	70
5.2	Level set reinitialization	70
5.3	Mechanical problem.	72
5.4	Diffusion/corrosion problem	73
5.5	Velocity extension	74
6	Numerical examples	75
6.1	1D pencil test	76
6.2	Initial pit shape	76
6.3	Lacy cover formation.	78
6.4	Influence of mechanical load	79
7	Conclusions.	82
	References	84
5	A three dimensional level set model for stress-assisted pitting corrosion	89
1	Introduction	91
2	Numerical framework.	92
3	Corrosion problem	93
3.1	Activation control	95
3.2	Diffusion control.	95
3.3	Corrosion regime control	96
4	Mechanical problem	96

5	Level set processes	98
5.1	Reinitialization.	98
5.2	Velocity extension	98
5.3	Level set update	99
6	Numerical examples	99
6.1	1D pencil test	99
6.2	3D pitting corrosion	100
7	Conclusions.	107
	References	110
6	Conclusions	115
1	Outlook	118

Summary

The world is currently in a severe man-made climate crisis, creating the need for using renewable energy sources such as offshore wind farms. Offshore wind turbines do not take up any valuable space on land and can use the greater wind resource at sea. The downside is, however, that they are exposed to a much harsher environment at sea, which could result in more failures and also lead to a smaller accessibility window for maintenance and repair. The structural components of offshore wind turbines are subjected to a corrosive environment and are exposed to cyclic loads that come in the form of wind and waves, which can cause significant corrosion and fatigue damage. Having accurate numerical models that can capture the physics of these damage processes could help reducing uncertainties on the structural performance of these components and therefore improve the position of offshore wind energy as a competitive renewable energy source.

In this thesis, two such models are developed, of which the first is a 2D model for capturing fatigue crack growth in ductile materials under mixed-mode loading and overloading. The approach is built upon a phantom node framework, such that a crack can grow through the elements and not only along element boundaries. The fracture process zone ahead of the physical crack tip is represented by means of cohesive tractions from which the energy release rate, and thus the stress intensity factor, can be extracted for an elastic-plastic bulk material. The approach relies on the separation between plasticity around the crack tip and fatigue crack growth at the crack tip, such that the influence of plasticity on fatigue driving forces is predicted. An extensive calibration method of the numerical model is presented in which the maximum tensile stress and the effective Paris parameters are tuned to a fatigue test with a single overload. The model has been validated for overloading and in-phase and out-of-phase biaxial fatigue loading in terms of crack path and crack growth rate.

The second model that has been developed concerns 2D stress-assisted pitting corrosion. This model uses the level set method combined with the finite element method, such that the domain can be split into a pit and a solid domain. In the pit domain the metal ion concentration distribution is computed by solving a diffusion equation. In the solid domain static equilibrium is solved in order to obtain the strains and stresses. The pit front can experience three regimes of corrosion, namely activation control, diffusion control and passivation. Under activation control, the front velocity is affected by the amount of mechanical stress and strain present in the solid. The model is verified and validated, and also a study is presented that shows the effect of different loading and corrosion scenarios on the pit growth rate. The pitting corrosion model has also been extended to 3D. The extension was natural because of the use of field equations for the level set reinitialization and velocity extension. The numerical model is compared against 3D

pitting experiments with and without mechanical cyclic loading. It was found that the pit grows fastest in the direction perpendicular to the applied loading. Furthermore, according to the numerical model, smaller anodic current densities result in a larger difference in pit growth rate between the loaded and non-loaded specimen.

Samenvatting

De wereld is momenteel in een ernstige mens-gemaakte klimaat crisis, wat de vraag naar groene energiebronnen zoals offshore windparken versterkt. Offshore wind turbines bezetten geen waardevolle ruimte op land. Daarbovenop, kunnen ze de grote hoeveelheid windenergie op zee benutten. Het nadeel is wel dat ze blootgesteld worden aan een veel ruigere omgeving wat resulteert in een grotere kans op falen van componenten, en moeilijkere toegankelijkheid voor onderhoud en reparatie. De structurele componenten van offshore wind turbines staan in een corrosieve omgeving en worden cyclisch belast door de aanwezigheid van wind en golven, wat kan zorgen voor corrosie en vermoeiingsschade. Computermodellen die de fysica van deze schade processen kan simuleren kunnen helpen om de onzekerheden in de structurele prestaties van deze componenten te verminderen en daarmee de positie van offshore windenergie als een competitieve groene energiebron te verbeteren.

In dit proefschrift zijn twee van zulke modellen ontwikkeld, waaronder een 2D scheurgroei model voor ductiele materialen onder *mixed mode* en overbelaste vermoeiingsbelasting. De methode maakt gebruik van het *phantom node* raamwerk zodat een scheur niet alleen langs de elementranden kan groeien, maar ook dwars door de elementen heen. Het scheurproces gebied dat voor de fysische scheurtip ligt is gerepresenteerd door middel van cohesieve tracties, waaruit de vrijlatingsenergie snelheid, en daarmee de spannings-intensiteitsfactor, kan worden bepaald voor een elastisch-plastisch bulk materiaal. De methode creëert daarom een scheiding tussen de plasticiteit om de scheurtip en scheurgroei van de scheurtip zodat de invloed van plasticiteit op de vermoeiings-drijvende krachten voorspeld kan worden. Daarnaast is een uitgebreide kalibratiemethode gepresenteerd waarin de maximale trekspanning en de effectieve Paris parameters zijn gekalibreerd door middel van een vermoeiingstest met één enkele overbelasting. De door het model voorspelde scheurpad en scheursnelheid zijn gevalideerd in het geval van overbelasting, en in-fase en uit-fase bi-axiale vermoeiingsbelasting.

De tweede numerieke methode is ontwikkeld om spannings-afhankelijke pit corrosie te modelleren. Het model combineert de *level set methode* met de eindige elementen methode zodat het numerieke domein opgesplitst kan worden in een pit en een vastestofdomein. In het pit domein wordt de concentratie verdeling bepaald door middel van een diffusie vergelijking. In het vaste-stofdomein wordt het statische evenwicht opgelost zodat de spanning en de rek uitgerekend kunnen worden. Het pitfront kan worden blootgesteld aan drie verschillende regimes, namelijk activatie gecontroleerd, diffusie gecontroleerd en passivatie. In het geval van activatie gecontroleerde corrosie is de front snelheid afhankelijk van de mechanische spanning en rek aanwezig in het materiaal gelegen nabij het pitfront. Het model is geverifieerd en gevalideerd, en een studie is gepre-

senteerd waarin de effecten van verschillende soorten belasting en corrosie scenario's op de pitgroei-snelheid worden besproken. Het pitgroei-model is ook uitgebreid naar drie dimensies. De uitbreiding was vereenvoudigd door het gebruik van veldvergelijkingen voor de level set re-initialisatie en de pitfront-snelheidsextensie. Het numerieke model is vergeleken met 3D pitgroei-experimenten met en zonder mechanisch cyclische belasting. Er is geconstateerd dat een pit het snelst groeit loodrecht op de richting van de belasting. Daarnaast, laat het numeriek model zien dat een kleine anodische stroomdichtheid resulteert in een groter verschil in pitgroei-snelheid tussen een belast en een onbelast specimen.

1

General Introduction

1. Societal background

The world is currently in a severe man-made climate crisis causing, amongst others, extreme weather conditions [1], a decline in human health [2], extinction of coral reefs [3], alarming situations for coastal cities through sea-level rise [4] and widespread extinction of amphibians [5]. In order to tackle this problem, the Paris Agreement has been adopted by almost 200 parties, with the goal to limit the total global warming below 2 °C and ideally below 1.5 °C [6] by reducing greenhouse gas emissions. However, an increase of 1.5 °C could already be reached by 2030 and 2 °C by 2050 [7], indicating the urgency of a big transformative change even beyond what has been decided upon in the agreement [8].

One of the key factors in reducing the greenhouse gas emissions is replacing fossil energy by renewable energy sources, such as wind energy. In Europe, in the year 2020, a total of 220 GW of wind turbine capacity was available, which equals to approximately 16% of the total energy demand. Most of this wind energy, about 89%, is produced by onshore turbines, and the remaining 11% by turbines placed offshore. However, in the coming 5 years these proportions will change as it is expected that offshore energy is going to make up 28% of the total wind capacity [9].

There are several advantages of using an offshore wind turbine farm with respect to one onshore. First of all, offshore turbines do not take up any valuable space on land. On top of that, good locations for onshore wind farms are often already occupied. Secondly, the noise created by the turbines is diminished through distance. Thirdly, there is a greater wind resource at sea, which is beneficial for the capacity. Fourthly, as the visual impact is smaller for turbines at sea, they are allowed to spin faster and can also be bigger such that they can capture wind at higher altitudes which result in a larger amount of operating hours [10].

However, there are also a couple of disadvantages of offshore solutions, of which the costs of installing and operating an offshore wind farm is a major example. Installing an offshore turbine is generally 20% more expensive compared to placing one onshore. Also, the costs of the foundational structure can be up to three times as much [11]. Furthermore, keeping maintenance costs low is a major challenge [12]. For example, the need of special vessels in order to perform repairs may increase the expenses significantly [13]. On top of that, offshore wind turbines are not always accessible due to the weather conditions, resulting in a waiting time and therefore a reduction in production for broken turbines [14]. Unfortunately, placing turbines too close to the coast can be considered horizon pollution, so they are preferably placed as far from the coast as possible. However, placement further from the coast results in larger installation costs as well as exposure to harsher environments, and thus more failures [15] and less accessibility [16]. Currently, the majority of wind farms are placed nearshore, which is less than 30 km from the shore. However, the current trend is to move further away from the coast where winds are stronger and more steady [17]. Finally, maintenance support is not only expensive, but is also a big contributing factor to the CO₂ emissions expelled during the life time of an offshore wind turbine [18].

2. Research scope and goal

The most common foundations used for offshore wind turbines include gravity bases, monopiles, suction buckets, tripods, jackets and high rise pile caps [19]. These foundations are placed in a corrosive environment and are exposed to stresses and strains induced by cyclic loads that come in the form of waves and wind. It is important to understand how these structures react to these conditions [20]. Availability of more information on the performance of structural components in a fatigue corrosion environment could reduce the associated risk, which could result in an extension of the inspection interval time and thus reduce the costs [21], making offshore wind a more competitive energy source.

As discussed by Schijve [22], fatigue damage can be split into two phases, namely crack initiation and crack propagation. Fatigue initiation includes the initial cyclic slip, crack nucleation and micro crack growth. In this stage, the performance of a material is commonly defined by means of an S-N curve, in which stress concentration factors play an important role. On the other hand, the fatigue crack propagation stage is concerned with macro cracks. The transition from micro crack to macro crack is defined as the point where crack growth no longer depends on the material surface conditions, but starts to depend on the bulk material properties. The rate of macro crack growth is most commonly computed using relations based on the Paris law [23], in which the stress intensity factor serves as an input. In the absence of any initial defects, the initiation phase covers the majority of the fatigue life of a structural component. However, a surface free from imperfections is not easy to guarantee as minor defects from manufacturing, transportation or installation are difficult to avoid. The structural components of wind turbines are often created by means of welding, which is notorious for causing defects. As a result the whole initiation phase is bypassed and the whole fatigue lifetime only depends on macro crack growth [22, 24].

Metal corrosion occurs in many different forms, but can roughly be divided into two major types, namely global or uniform corrosion, and local corrosion. The latter comes in various forms such as pitting, crevice corrosion, stress corrosion cracking and inter granular corrosion [25]. According to guidelines for wind turbine support structures [26, 27], the effect of corrosion should be taken into account by assuming a nominal decrease in wall thickness. In essence, this means that it is assumed that the type of corrosion is uniform. It is also mentioned that a grade of steel should be chosen which is not susceptible to pitting. However, pitting, which is a much more severe type of corrosion, is not uncommon to occur in the inner sections of offshore structures made of S355 steel [28–31]. According to the guidelines, these sections should be watertight and therefore corrosion free, but reality dictates differently. Pits are dangerous because they can quickly grow deep into the material, causing stress concentration sites and accelerating the fatigue initiation damage process, which has led to severe failures in offshore structures [32].

Stress-assisted pit propagation and fatigue crack growth under various loading conditions are damage processes that are not yet fully understood. To account for it in the design requires significant additional investments. Numerical models that can accurately simulate the relevant physics related to fatigue and corrosion could help in reducing un-

certainties. Lower uncertainties means a possible reduction in operation costs by lowering the number of inspections. This would improve the market position of offshore wind energy as a competitive renewable energy source. On top of that, a reduction in inspection could reduce the total emission of greenhouse gas during the life cycle of an offshore wind turbine.

The goal of the thesis is to develop numerical models that can accurately capture the relevant physics of two types of damage processes. The first model is concerned with fatigue crack propagation. The goal is to have a model that can not just capture crack growth under constant amplitude mode I cyclic loading, but also under multiple non-trivial loading situations such as overloading, and in-phase and out-of-phase mixed mode loading. This requires a numerical method that can correctly capture the effect of plasticity on the crack growth behaviour. Furthermore, the method should be applicable even when the crack growth direction is not known *a priori*.

1

The second model focusses on simulating stress-assisted pitting corrosion. This is a multi-physics problem in which the velocity of the moving pit front depends on the corrosion and mechanical load conditions. The model should be able to predict the effect of different type of loading and corrosion conditions on the pit growth rate and the pit shape development.

It should be noted that all experimental data used in the various chapters originate from literature. Consequently, the material in consideration is often not what is used for offshore wind turbines, or offshore structures in general. However, the methodology is such that with the appropriate material properties, the models can also be employed for offshore wind turbine structures. This means that the developed models are not just useful for offshore wind turbines, but are also applicable to all kinds of structures which are exposed to fatigue loading and/or a corrosive environment.

3. Thesis outline

In **Chapter 2** a numerical approach is presented with which fatigue crack growth in ductile materials under mixed-mode loading and overloading can be captured. The approach is built upon a phantom node framework such that a discrete crack can grow through the elements and not only along element boundaries. The fracture process zone ahead of the physical crack tip is represented by means of cohesive tractions from which the energy release rate, and thus the stress intensity factor, can be extracted for an elastic-plastic bulk material. Two different models to compute the cohesive tractions are compared. First, a cohesive zone model with a static cohesive law is used. The second model is based on the interfacial thick level set method in which tractions follow from a given damage profile.

In **Chapter 3** a calibration method for the fatigue crack growth model with cohesive law, discussed in the previous chapter, is presented. The approach relies on the separation between plasticity around the crack tip and fatigue crack growth at the crack tip such that the influence of plasticity on fatigue driving forces is predicted. Consequently, char-

acterization of crack growth requires effective crack growth parameters. It is investigated whether the calibrated model can capture fatigue crack growth behaviour in ductile materials for in-phase and out-of-phase biaxial fatigue loading as well as in-phase biaxial loading with an overload.

In **Chapter 4** a 2D numerical model for stress-assisted pitting corrosion model is presented. This model uses the level set method combined with the finite element method such that the domain can be split into a pit and a solid domain. In the pit domain the concentration distribution is computed by solving a diffusion equation. In the solid domain static equilibrium is solved in order to obtain the strains and stresses. The pit front can experience three regimes of corrosion, namely activation control, diffusion control and passivation. Under activation control, the front velocity is affected by the amount of mechanical stress and strain present in the solid. Different loading and corrosion scenarios are compared.

Chapter 5 describes the extension of the numerical pitting corrosion model of the previous chapter to three dimensions. The extension required little model adaption because of the use of field equations for the level set reinitialization and velocity extension. The numerical model is compared against 3D pitting experiments with and without mechanical cyclic loading. Furthermore, the shape evolution of a corrosion pit under mechanical loading is investigated.

Finally, in **Chapter 6** the conclusions are presented, followed by a short discussion on the future outlook.

References

- [1] D. Coumou and S. Rahmstorf, *A decade of weather extremes*, *Nature Climate Change* **2**, 491–496 (2012).
- [2] J. Patz, D. Campbell-Lendrum, T. Holloway, and J. Foley, *Impact of regional climate change on human health*, *Nature* **438**, 310–317 (2005).
- [3] O. Hoegh-Guldberg, P. J. Mumby, A. J. Hooten, R. S. Steneck, P. Greenfield, E. Gomez, C. D. Harvell, P. F. Sale, A. J. Edwards, K. Caldeira, N. Knowlton, C. M. Eakin, R. Iglesias-Prieto, N. Muthiga, R. H. Bradbury, A. Dubi, and M. E. Hatzioolos, *Coral reefs under rapid climate change and ocean acidification*, *Science* **318**, 1737 (2007).
- [4] R. Nicholls and A. Cazenave, *Sea-level rise and its impact on coastal zones*, *Science* **328**, 1517 (2010).
- [5] J. Alan Pounds, M. R. Bustamante, L. A. Coloma, J. A. Consuegra, M. P. L. Fogden, P. N. Foster, E. La Marca, K. L. Masters, A. Merino-Viteri, R. Puschendorf, S. R. Ron, G. A. Sanchez-Azofeifa, C. J. Still, and B. E. Young, *Widespread amphibian extinctions from epidemic disease driven by global warming*, *Nature* **439**, 161–167 (2006).
- [6] *Paris agreement*, United Nations (2015).
- [7] R. Watson, C. Carraro, P. Canziani, N. Nakicenovic, J. J. McCarthy, J. Goldemberg, and L. Hisas, *The truth about climate change* (FEU-US, 2016).
- [8] J. Rogelj, M. den Elzen, N. Höhne, T. Fransen, H. Fekete, H. Winkler, R. Schaeffer, F. Sha, K. Riahi, and M. Meinshausen, *Paris agreement climate proposals need a boost to keep warming well below 2° C*, *Nature* **534**, 631–639 (2016).
- [9] I. Komusanac, G. Brindley, D. Fraile, and L. Ramirez, *Wind energy in Europe: 2020 Statistics and the outlook for 2021-2025*, Tech. Rep. (Wind Europe, 2021).
- [10] A. Colmenar-Santos, J. Perera-Perez, D. Borge-Diez, and C. dePalacio Rodríguez, *Offshore wind energy: A review of the current status, challenges and future development in Spain*, *Renewable and Sustainable Energy Reviews* **64**, 1–18 (2016).
- [11] M. Bilgili, A. Yasar, and E. Simsek, *Offshore wind power development in Europe and its comparison with onshore counterpart*, *Renewable and Sustainable Energy Reviews* **15**, 905–915 (2011).
- [12] F. Blaabjerg and D. Ionel, *Renewable energy devices and systems – state-of-the-art technology, research and development, challenges and future trends*, *Electric Power Components and Systems* **43**, 1319–1328 (2015).
- [13] G. J. W. Van Bussel and M. B. Zaaijer, *Reliability, availability and maintenance aspects of large-scale offshore wind farms, a concepts study*, (2001).
- [14] S. Breton and G. Moe, *Status, plans and technologies for offshore wind turbines in Europe and North America*, *Renewable Energy* **34**, 646–654 (2009).

-
- [15] M. Shafiee, *A fuzzy analytic network process model to mitigate the risks associated with offshore wind farms*, *Expert Systems with Applications* **42**, 2143–2152 (2015).
- [16] G. J. W. Van Bussel, A. R. Henderson, C. A. Morgan, B. Smith, R. Barthelmie, K. Argyriadis, A. Arena, G. Niklasson, and E. Peltola, *State of the art and technology trends for offshore wind energy: operation and maintenance issues*, (2001).
- [17] H. Díaz and C. Guedes Soares, *Review of the current status, technology and future trends of offshore wind farms*, *Ocean Engineering* **209**, 107381 (2020).
- [18] A. Arvesen, C. Birkeland, and E. Hertwich, *The importance of ships and spare parts in lcas of offshore wind power*, *Environ. Sci. Technol.* **47**, 2948–2956 (2013).
- [19] K. Oh, W. Nam, M. Ryu, J. Kim, and B. I. Epureanu, *A review of foundations of offshore wind energy convertors: Current status and future perspectives*, *Renewable and Sustainable Energy Reviews* **88**, 16–36 (2018).
- [20] O. Adedipe, F. Brennan, and A. Kolios, *Review of corrosion fatigue in offshore structures: Present status and challenges in the offshore wind sector*, *Renewable and Sustainable Energy Reviews* **61**, 141–154 (2016).
- [21] D. Straub, J. Goyet, J. D. Sorensen, and M. H. Faber, *Benefits of risk based inspection planning for offshore structures*, (2006).
- [22] J. Schijve, *Fatigue of structures and materials* (Springer Science & Business Media, 2001).
- [23] P. Paris and F. Erdogan, *A critical analysis of crack propagation laws*, *Journal of Basic Engineering* **85**, 528–533 (1963).
- [24] L. Ziegler, S. Schafhirt, M. Scheu, and M. Muskulus, *Effect of load sequence and weather seasonality on fatigue crack growth for monopile-based offshore wind turbines*, 13th Deep Sea Offshore Wind R&D Conference, EERA DeepWind'2016 **94**, 115–123 (2016).
- [25] E. McCafferty, *Introduction to corrosion science* (Springer Science & Business Media, 2010).
- [26] *Design of Offshore Wind Turbine Structures (DNV-OS-J101)*, DNV GL-Energy, The Netherlands (2014).
- [27] *Support Structures for Wind Turbines (DNVGL-ST-0126)*, Det Norske Veritas, Norway (2016).
- [28] C. Haixiang and K. Dejun, *Microstructures and immersion corrosion performances of arc sprayed amorphous Al-Ti-Ni coating on S355 structural steel*, *Anti-Corrosion Methods and Materials* **65**, 271–280 (2018).
- [29] X. He, R. G. Song, and D. J. Kong, *Microstructure and corrosion behaviour of laser-cladding Al-Ni-TiC-CeO₂ composite coatings on S355 offshore steel*, *Journal of Alloys and Compounds* **770**, 771–783 (2019).

- [30] W. Khodabux, P. Causon, and F. Brennan, *Profiling corrosion rates for offshore wind turbines with depth in the north sea*, *Energies* **13** (2020).
- [31] W. Khodabux, C. Liao, and F. Brennan, *Characterisation of pitting corrosion for inner section of offshore wind foundation using laser scanning*, *Ocean Engineering* **230**, 109079 (2021).
- [32] J. Bhandari, F. Khan, R. Abbassi, V. Garaniya, and R. Ojeda, *Modelling of pitting corrosion in marine and offshore steel structures – a technical review*, *Journal of Loss Prevention in the Process Industries* **37**, 39–62 (2015).

2

A cohesive XFEM model for simulating fatigue crack growth under mixed-mode loading and overloading

R. Dekker^a , F.P. van der Meer^a, J. Maljaars^{b,c}, L.J. Sluys^a

^a Faculty of Civil Engineering and Geosciences, Delft University of Technology, Delft, The Netherlands

^b Faculty of Built Environment, Eindhoven University of Technology, Eindhoven, The Netherlands

^c Structural reliability, TNO ,Delft, The Netherlands

ABSTRACT

Structures are subjected to cyclic loads that can vary in direction and magnitude, causing constant amplitude mode I simulations to be too simplistic. This study presents a new approach for fatigue crack propagation in ductile materials that can capture mixed-mode loading and overloading. The extended finite element method is used to deal with arbitrary crack paths. Furthermore, adaptive meshing is applied to minimize computation time. A fracture process zone ahead of the physical crack tip is represented by means of cohesive tractions from which the energy release rate, and thus the stress intensity factor, can be extracted for an elastic-plastic material. The approach is therefore compatible with the Paris equation, which is an empirical relation to compute the fatigue crack growth rate. Two different models to compute the cohesive tractions are compared. First, a cohesive zone model with a static cohesive law is used. The second model is based on the interfacial thick level set method in which tractions follow from a given damage profile. Both models show good agreement with a mode I analytical relation and a mixed-mode experiment. Furthermore, it is shown that the presented models can capture crack growth retardation as a result of an overload.

1. Introduction

Numerous structures such as wind turbines, bridges and cars, are exposed to cyclic loading. The fatigue crack propagation behaviour of these structures is commonly simulated with models that are only valid for mode I constant amplitude loading. However, in real-life applications, the applied loads can vary in direction and magnitude. For example, a change in loading direction may cause a mixed-mode stress field around the crack tip, changing the crack growth direction [1]. Furthermore, a change in loading magnitude, such as an overload, can create a significant crack growth retardation effect by means of plasticity induced crack closure [2, 3]. This study presents a new fatigue crack growth model that can capture the effects of mixed-mode loading and overloading.

Traditionally, fatigue crack propagation is predicted by means of the Paris equation [4], which links the cyclic change in stress intensity factor (SIF) to a crack growth rate. A drawback of this method is that the SIF is only a valid measure for materials that show small scale yielding around the crack tip, otherwise linear elastic fracture mechanics (LEFM) cannot be used. A significant amount of yielding can be found for instance when considering overloading in ductile materials, making the SIF lose its validity. Furthermore, Paris parameters are generally determined for mode I loading and thus cannot readily be used for mixed-mode loading. Modifications to the Paris equation exist to extend its applicability to mixed-mode loading [5] and overloading [6, 7]. However, these methods are only valid for specific load cases.

To deal with mixed-mode scenarios for which the crack growth direction is not known a priori, extended finite element (XFEM) models have been developed for fatigue analysis [8, 9]. In these models, crack tip enrichments following from LEFM are applied to capture the strain field around the crack tip. Furthermore, the J-integral [10] is used to calculate the SIF, which is coupled to the crack growth rate by means of a modified Paris equation [5]. However, the LEFM crack tip enrichments and the J-integral are invalid for elastic-plastic materials. Therefore, the models presented in [8, 9] cannot readily be extended by simply using an elastic-plastic material around the crack to capture the effects of overloading. XFEM can also be used with a cohesive zone (CZ) approach instead of with crack tip enrichment [11, 12]. This is more suitable in combination with plasticity [13], but has not yet been used for fatigue problems.

Cohesive zone models were originally developed for quasi-static crack growth predictions [14, 15] and have been successfully used in the context of interface elements for cases where the crack path is known a priori [16–18]. In a CZ model, the loss of bonding strength in the fracture process zone (FPZ) ahead of the macro crack tip is captured by means of tractions. These tractions are calculated with a traction-separation or cohesive law. However, these cohesive zone models cannot readily be used to model crack growth due to cyclic loading. In fatigue crack growth cases the maximum applied load is smaller than required for quasi-static crack propagation. Consequently, under constant amplitude cyclic loading the crack will simply not grow. This problem can be solved by means of two different approaches.

In the first approach, the crack tip is forced forward and the amount of cycles required

for this jump is computed by means of the Paris equation. In these models the energy release rate (ERR) is computed by the J-integral around the zero thickness interface elements [19] or by using the local ERR extracted from the cohesive law of the most damaged point in the fracture process zone [20–22]. Since the bulk material is not considered in this J-integral, it can also be used to compute the ERR as a local driving force for propagation of a crack embedded in an elastic-plastic bulk material.

In the second approach, dissipative mechanisms are added to the traction separation law of the CZ model such that the crack can keep on growing in fatigue loading [23–28]. This circumvents the use of the Paris equation and its modifications for different loading scenarios. In some of these modified cohesive zone models the bulk plastic behaviour is separated from the creation of crack faces in which case it was shown that an overload causes the plastic zone of the bulk material around the crack tip to increase in size [24, 26, 27]. This increase in plastic zone size effectively closes the crack before the minimum load level is reached and consequently causes crack growth retardation, as is observed in experiments. The downside of these modified cohesive zone models is that the dissipative equations lack physical meaning.

2

Recently, the interfacial thick level set (ITLS) method was introduced as an alternative for CZ models [29–31]. The ITLS method is derived from the thick level set method [32, 33], which is a regularized continuum damage model. The ITLS method itself is similar to a cohesive zone model in the sense that it provides a traction-separation relation. The main difference between the ITLS method and conventional CZ models is that the damage profile over the fracture process zone for the ITLS method is given instead of being computed from a cohesive law. The shape of the damage profile and the length, which is equal to the length of the fracture process zone, should be known or estimated a priori in the ITLS method. The method allows for straightforward evaluation of the ERR which makes the ITLS particularly suitable for combining it with the Paris equation.

In this study, a cohesive XFEM model that can capture fatigue crack growth in arbitrary direction under mixed-mode loading and overloading is presented. Two different models to define cohesive tractions are compared. The first model is a CZ model that uses a static cohesive law as starting point. The CZ model is implemented with the two different ERR extraction methods given by Harper and Hallet [20] and by Bak et al. [19]. The second model uses the interfacial thick level set method where the ERR extraction method follows from Voormeeren et al. [30]. Unlike current ITLS models, the length of the fracture process zone is not a user input, but will follow automatically from the simulation. For both models, the Paris equation is used for relating the stress intensity factor, and thus the ERR, to crack growth. By separating the plastic bulk material from the creation of crack faces and by including a mixed-mode description of the fracture process zone, the Paris equation does not need any adjustments for overloading or mixed-mode loading. Furthermore, by using XFEM the crack can continuously change direction, depending on the stress field around the crack tip. Finally, adaptive meshing is used to minimize computation time.

The paper starts with the numerical framework followed by a description of the behaviour of the bulk material and the fracture process zone. The fracture process zone

behaviour for both the CZ and ITLS models is presented together with their ERR extraction methods. Subsequently, the crack tip propagation criteria are discussed. Finally, three numerical examples are presented to verify, validate and compare the accuracy of the models.

2. Numerical framework

A cracked medium as shown in Fig. 1 is considered. The specimen is subjected to cyclic loading, causing the crack to propagate. The crack can grow in an arbitrary direction depending on the specimen geometry and the applied loading.

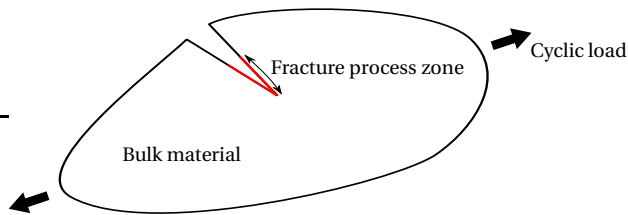


Figure 1: Cracked medium

Physically, a FPZ is present ahead of the macro or physical crack tip, which is indicated as the black area in Fig. 2. For the numerical models it is assumed that this zone can be compressed into a single line. The process zone is then represented numerically by means of traction forces across a displacement discontinuity, shown at the bottom of Fig. 2. As a result, in the numerical model the crack tip is located ahead of the FPZ, which is called the fictitious or numerical crack tip. Material ahead of the numerical crack tip does not have any damage. On the other hand, the material in the wake of the physical crack tip has maximum damage indicating traction-free separation of the crack faces.

In order to accurately and efficiently capture fatigue crack growth under general load conditions, the numerical framework needs to have two important characteristics. First of all, the crack path is not known a priori, which means that the crack needs to have the freedom to grow in any arbitrary direction. The standard finite element method will not allow this, because displacement jumps can only be present along element boundaries. For this reason, this study uses XFEM, which enables a crack to grow through the elements.

The second characteristic is also related to the unknown crack path. The FPZ for fatigue crack growth in metals is very local. Therefore, a high mesh density is required in the area around the crack tip in order to correctly capture the strain field. However, as the crack path is unknown, it means that the whole domain should consist of small elements, increasing the computation time significantly. In this study, an adaptive meshing strategy is used, which ensures a high mesh density around the fracture process zone and a low mesh density far away from this zone in order to minimize the computation time without significant loss of accuracy.

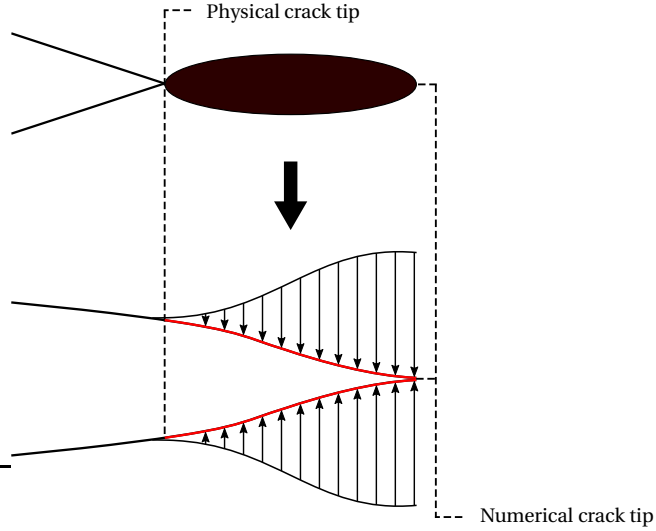


Figure 2: The real fracture process zone (top) is modelled by means of cohesive tractions (bottom)

2

2.1. Phantom node technique

XFEM was initially developed by Belytschko and Black [34], and Moës et al. [35] as a method in which a discontinuity like a crack does not necessarily have to be located along an element boundary as is the case for the standard Finite Element Method. Node enrichments are used in order to capture a discontinuity in an element without the need of re-meshing. Therefore, XFEM can be used to predict crack propagation for cases where the crack growth direction is not known a priori [11, 36, 37].

For ease of implementation, an alternative formulation of XFEM has been used in this study, which is called the phantom-node method [12, 38–41]. The phantom node method is visualized in Fig. 3. Four phantom nodes are introduced if a crack crosses an element, which initially have the same location as the original regular nodes. With these eight nodes in total, the single element is split into two elements. The first element has regular nodes above the crack and phantom nodes below, and the second element the other way around. The grey areas indicate which part of the element is active, which means that the internal force and stiffness matrix contribution of the first element are evaluated by integrating over the element subdomain above the crack line. A displacement jump between the two elements can be present, because the two elements do not share any nodes.

2.2. Adaptive meshing

In this study, four noded quadrilateral elements are considered, enabling the use of a quad-tree algorithm for the adaptive meshing process [42–44]. A simple visualization of a quad-tree algorithm is shown in Fig. 4. It starts with the original element on the

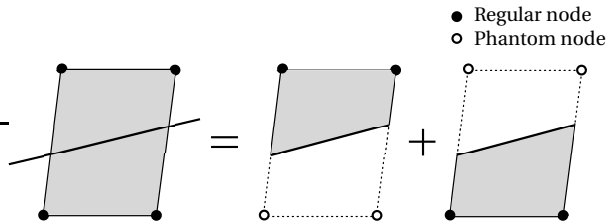


Figure 3: Phantom node method

left, which is defined as level zero. If refinement of the element is required, it is divided into four new elements, all having the same aspect ratio as the original one. These new elements are defined to be one refinement level higher than the element from which they were created, which makes them level one. This process can then be repeated until the required refinement has been achieved.

The application of the quad-tree algorithm results in nodes that end up in the middle of an element boundary, instead of only at element corners. These nodes are called hanging nodes. A hanging node is constrained to the adjacent corner nodes in order to maintain a continuous displacement field. The maximum allowable difference in refinement level between adjacent elements is one to achieve better efficiency, following Palle [42].

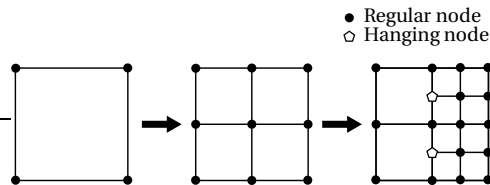


Figure 4: Mesh refinement by means of a quad-tree algorithm

Refinement is performed when an element is within a certain distance from the numerical crack tip. De-refinement is applied when the physical crack tip has run past a refined element and is a certain distance away from it. The extent of the refinement zone and the minimal required element size are thus problem specific and based on user experience. Other more general refinement criteria that use a finite element error estimation are treated in [42, 44]. It should be noted that elements crossed by a crack are not de-refined in order to keep the geometry of the crack. Consequently, the total number of elements increases for increasing crack length.

3. Material behaviour

The bulk material behaviour is considered separately from the process zone behaviour, having both their own set of constitutive relations. As a result, the crack growth process is driven by a combination of the two. First, the bulk material behaviour is discussed. Second, the fracture process zone behaviour for both the cohesive zone model and the

interfacial thick level set method are treated.

3.1. Bulk material

An elastic-plastic bulk material is considered. The elastic behaviour follows from Hooke's law. The plasticity model uses both isotropic and kinematic hardening in order to capture plastic flow under cyclic loading. The Von Mises criterion is used to describe the yield surface:

$$f = \sqrt{\frac{2}{3}(\mathbf{s} - \boldsymbol{\beta}) : (\mathbf{s} - \boldsymbol{\beta})} - \sigma_y \quad (2.1)$$

where \mathbf{s} and $\boldsymbol{\beta}$ are the deviatoric stresses and deviatoric back-stresses, respectively. The yield stress σ_y is defined with a non-linear isotropic hardening rule [45]:

$$\sigma_y = \sigma_0 + Q_\infty \left(1 - e^{-b\bar{\epsilon}^p}\right) \quad (2.2)$$

where σ_0 is the initial yield stress, Q_∞ the limit value for the yield stress increase and b is a measure for the rate of change of the yield surface. The increment in equivalent plastic strain $d\bar{\epsilon}^p$ is given as:

$$d\bar{\epsilon}^p = \sqrt{\frac{2}{3}d\epsilon^p : d\epsilon^p} \quad (2.3)$$

where $d\epsilon^p$ is the plastic strain increment. The kinematic hardening rule is given by [46]:

$$d\boldsymbol{\beta} = \sum_{i=1}^3 \left(\frac{2}{3} C_i d\epsilon^p - \gamma_i \boldsymbol{\beta}_i \bar{\epsilon}^p \right) \quad (2.4)$$

where C_i is the linear kinematic hardening coefficient and γ_i the non-linear one.

The phantom node technique and the adaptive meshing algorithm require mapping of the plasticity history variables. This mapping is performed based on the distance between the new and old integration points, following Wells et al. [47].

3.2. Cohesive zone model

The cohesive zone model uses a static cohesive law for each integration point on the crack, from which the traction, and thus the amount of damage, can be computed. A simple bilinear cohesive law is used, which is given in Fig. 5a.

The cohesive law uses a mixed-mode formulation in which the effective traction τ is a function of the effective displacement jump δ , which is given by [48, 49]:

$$\delta = \sqrt{\langle \delta_n \rangle^2 + \beta^2 \delta_s^2} \quad (2.5)$$

where δ_n and δ_s are the displacement jumps in the normal and tangential direction, respectively. Furthermore, Macaulay brackets are denoted by $\langle \cdot \rangle$. The parameter β is equal to the ratio between the tensile and shear strength of the material.

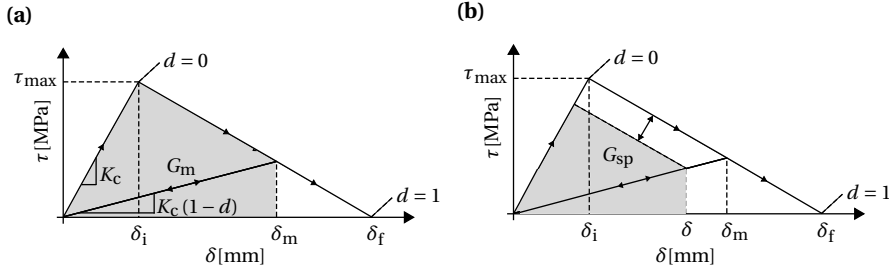


Figure 5: Cohesive law showing (a) the local maximum energy release rate, and the loading and unloading behaviour, and (b) the local energy release rate at unloading and reloading

The area below the curve of the cohesive law is equal to G_c , which is the critical ERR for mode I or cleavage failure. The parameter τ_{\max} is the maximum effective traction stress and is equal to the tensile strength of the material. The parameter δ_m is defined as the maximum effective displacement jump that has been reached for a specific material point, which has a corresponding damage d that is defined as:

$$d = \frac{\delta_f(\delta_m - \delta_i)}{\delta_m(\delta_f - \delta_i)} \quad (2.6)$$

where it can be seen that the damage d increases for increasing δ_m . Here, δ_i and δ_f are the fracture initiation and final failure displacement jumps, respectively, which follow from τ_{\max} , G_c and K_c . Damage only starts to accumulate once the effective displacement jump becomes larger than δ_i . The damage reaches its maximum value of one when δ_f has been reached. The initial cohesive stiffness K_c is adjusted for the accumulated damage by multiplying it with $(1 - d)$. The effective traction-displacement relations can therefore be written as:

$$\tau = \begin{cases} K_c \delta & \delta_m < \delta_i \\ K_c (1 - d) \delta & \delta_m \geq \delta_i \\ 0 & \delta_m \geq \delta_f \end{cases} \quad (2.7)$$

From the effective traction, the tractions in the normal direction τ_n and sliding direction τ_s can be calculated using the following equations:

$$\tau_n = \begin{cases} \frac{\tau}{\delta_m} \delta_n & \delta_n \geq 0 \\ K_c \delta_n & \delta_n < 0 \end{cases} \quad (2.8)$$

$$\tau_s = \beta^2 \frac{\tau}{\delta_m} \delta_s \quad (2.9)$$

Note that for a negative displacement jump the normal traction is calculated with the initial cohesive stiffness, irrespective of the amount of accumulated damage. The large initial stiffness ensures contact between the two crack faces by preventing any large negative normal displacement jumps. Therefore, K_c should be given a sufficiently large value. Under that condition, its exact value does not influence the global response.

The maximum local ERR of a material point having a certain combination of δ_m and d can be calculated as follows:

$$G_m = \frac{1}{2} K_c \delta_m (\delta_i d + (1-d)\delta_m) \quad (2.10)$$

which is equal to the grey area in Fig. 5a. Upon unloading and reloading, the local ERR of a single material point is given by:

$$G_{SP} = \left(\frac{\delta}{\delta_m} \right)^2 G_m \quad (2.11)$$

which comes from the consideration that G_{SP} is a quadratic function of the applied load and is equal to the grey area in Fig. 5b. Notice how the outer static curve moves inwards during unloading and reloading. Harper and Hallett [20] showed that the ERR of a specimen is equal to the local ERR G_{SP} of a single material point at the physical crack tip.

Instead of using the single point estimation, the ERR can also be extracted by computing the J-integral around the interface elements as done by Bak et al. [19]. This equals to integrating the traction-separation behaviour of the complete fracture process zone. The J-integral over the fracture process zone can be defined as follows:

$$G_J = \int_0^{\max(\delta)} \tau d\delta \quad (2.12)$$

which is computed by means of the Riemann sum.

3.3. Interfacial thick level set

The main difference between the ITLS method and the CZ model is in the definition of the damage. For the ITLS method, the damage profile over the fracture process zone should be provided, instead of having a cohesive law from which the damage is calculated. An example of such a damage profile is given in Fig. 6.

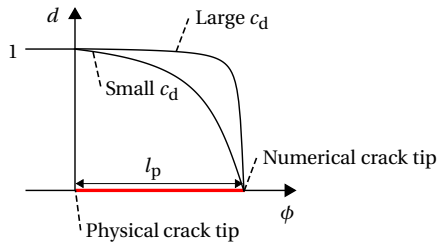


Figure 6: Damage profile over the fracture process zone for the ITLS method

Here, Eq. (2.7) is combined with the damage distribution over the fracture process zone from Voormeeren et al. [30] which is given by:

$$d(\phi) = \frac{1}{\arctan(c_d)} \arctan\left(c_d \left(\frac{l_p - \phi}{l_p}\right)\right) \quad (2.13)$$

in which ϕ has a value of zero at the physical crack tip and is equal to the fracture process zone length at the numerical crack tip. Furthermore, c_d determines the slope of the function and l_p is the fracture process zone length. Only c_d needs to be given as an input, because in the present XFEM formulation l_p automatically follows from the simulation.

The ERR is determined globally from integrating the change of the local interfacial free energy over the fracture process zone for an increase in crack length, which gives the following relation [30]:

$$G_{IE} = \int_0^{l_p} \frac{1}{2} \delta K_c \delta d' d\phi \quad (2.14)$$

Here, d' is the derivative of the damage with respect to the level set function ϕ . The effective displacement jump δ is the same as given in Eq. (2.5), which means that the ITLS method can be used for mixed-mode loading as well. It should be noted that for a given damage distribution and opening profile G_{IE} is equivalent to G_J from Eq. (2.12), but written in a form more suitable for the ITLS method.

3.4. Fatigue crack relation

The Paris equation [4] is used to compute the crack growth rate da/dN , which is defined as follows:

$$\frac{da}{dN} = c (\Delta K)^m \quad (2.15)$$

where a is the crack length, N is the number of cycles, ΔK is the SIF range, c is the Paris constant and m is the Paris exponent. Both the cohesive zone model and the interfacial thick level set method compute the ERR for a given state of the model, and not the SIF. However, for elastic materials the SIF can simply be computed from the ERR with the following equation:

$$K = \sqrt{GE} \quad (2.16)$$

where G is the ERR and E the Young's modulus. Note that the above equation is only valid for plane stress, but a similar relation exists for plane strain. The effect of different mode-mixities is captured in G by means of the effective displacement jump given in Eq. (2.5). Therefore, even for mixed-mode loading, mode I Paris parameters are used to determine the fatigue crack growth rate.

It should be noted that Eq. (2.16) cannot give a real SIF when considering an elastic-plastic material. However, the SIF obtained from the fracture process zone inside the plastic bulk can still be used as an indication of the magnitude of the crack driving force and will therefore be considered as an effective K .

4. Crack tip propagation

The physical and the numerical crack tip both have their own propagation criterion similar to [23]. As a result, the size of the fracture process zone l_p is variable, because it is

defined by the positions of the physical and the numerical crack tip. The CZ model will determine the damage over the whole process zone by means of its traction-separation law. For the ITLS model, the damage distribution is therefore re-calculated every time l_p is changed by means of Eq. (2.13). In both cases, irreversibility of damage growth is ensured.

In this study both the physical and numerical crack tip are only allowed to grow from element boundary to element boundary. Figure 7 shows an illustration of a crack with a fracture process zone in a finite element framework in which the numerical and physical crack tip are indicated. The fracture process zone is indicated with the solid line of which the arc length is equal to l_p . The dashed line indicates the part where the crack faces have been completely separated.

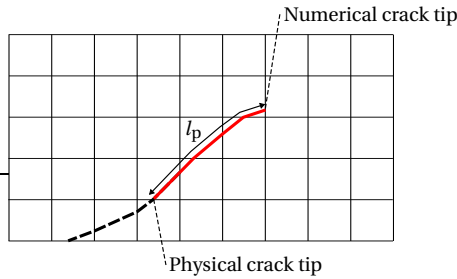


Figure 7: Crack (dashed line) with fracture process zone (solid line) in an XFEM framework.

4.1. Numerical crack tip

Numerical crack tip propagation, illustrated in Fig. 8, is the same for both quasi-static and fatigue loading. It occurs when the maximum principal stress in an integration point located in a small region around the numerical crack tip exceeds the failure stress which has the same value as τ_{\max} in Fig. 5a. This region is indicated in Fig. 8 with a circle, which generally has a radius of six times the element size.

The direction of crack growth is determined by means of the maximum principal stress criterion [50], which is valid for low and moderately high mode mixities [51], using a non-local approach [11, 12]. The non-local stress is calculated by taking the stress states of the integration points in the neighbourhood of the numerical crack tip and weighing them with the following function:

$$w = \frac{l_w}{(2\pi)^{3/2} l_w^3} \exp\left(-\frac{r_w^2}{2l_w^2}\right) \quad (2.17)$$

Here, r_w is the distance from the numerical crack tip to the specific integration point and l_w defines the rate of decay of the weight function, generally taken equal to three times a typical element size. The same region as for the maximum principle stress criterion is considered when computing the crack growth direction.

The crack extends to the next element boundary once the numerical crack tip propaga-

tion criterion is met. As a result, the fracture process zone size will increase, as shown in Fig. 8. After numerical crack tip propagation, a new equilibrium solution is found for the updated discretization. The increased process zone size results in smaller stresses ahead of the numerical crack tip. Numerical crack tip propagation is repeated until τ_{\max} is no longer exceeded at the crack tip.

Generalization of the element-by-element crack growth algorithm to a 3D situation is possible as well following Moes et al. [52, 53].

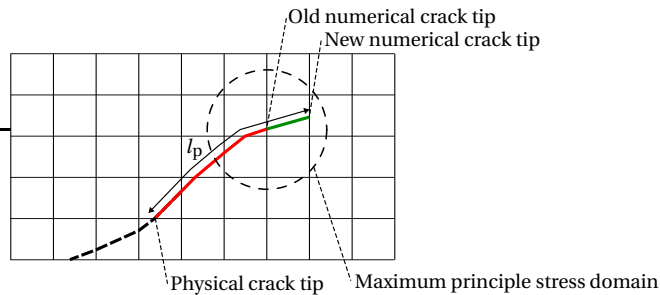


Figure 8: Numerical crack tip propagation

4.2. Physical crack tip

In simulations for static loading the physical crack tip moves forward when the local cohesive damage reaches its critical value of one. This means there is no need to keep track of the physical crack tip location. In the case of fatigue crack growth, the physical crack tip for the CZ model does not move forward without help, because a static damage of one will not be reached. In fatigue crack growth cases the maximum applied load is smaller than required for quasi-static crack propagation. Furthermore, the physical crack tip for the ITLS method does, by definition, not move forward by itself.

For both models, this is solved through forcing the physical crack tip forward by setting the damage of the process zone element that is adjacent to the current physical crack tip equal to one [22]. As a result, the fracture process zone decreases in size, as is shown in Fig. 9. Consequently, the stresses ahead of the numerical crack tip increases such that numerical crack tip propagation could occur again. Physical crack tip propagation is done after every single simulated loading cycle, indicated with the dots in Fig. 10.

During post-processing the real amount of fatigue cycles dN that a single simulated loading cycle represents is calculated by means of Eq. (2.15). The increase in crack growth length da is known, which is the distance the physical crack tip shifted forward. The ERR is extracted at every time step and thus the SIF range ΔK can be computed for every cycle with Eq. (2.16).

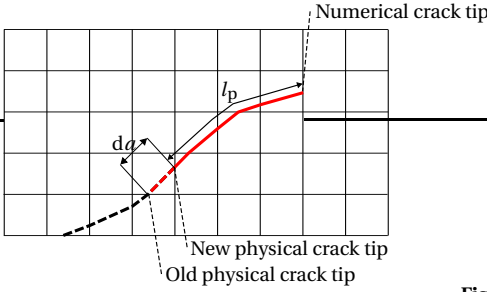


Figure 9: Physical crack tip propagation

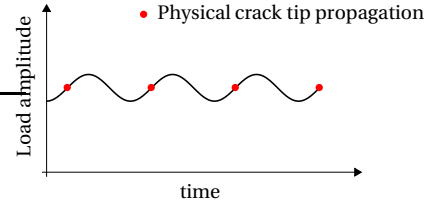


Figure 10: Loading cycles with physical crack tip propagation moments

5. Numerical examples

In this section three different numerical examples are presented. Firstly, a mode I linear elastic case is considered in which the presented models are compared against an analytical solution. An overload is included to investigate the accuracy of the different ERR extraction methods for a scenario that does not have constant amplitude loading. Secondly, a mixed-mode linear elastic case is shown where both models are compared against an experiment. Finally, an elastic-plastic mode I case is considered, which is subjected to both a constant amplitude loading and an overload to demonstrate the suitability of the method for modelling crack retardation.

For all cases the material is aluminium 2024-T4, of which the properties are given in Table 1. The plasticity parameters are taken from Abdollahi and Chakherlou [54] and the Paris parameters from Jeong [55]. The parameter β is based on the quasi-static failure stress taken from [56] and the critical ERR is taken from Dursun and Soutis[57]. The cohesive stiffness, which is a numerical parameter, should be chosen sufficiently stiff. All the given numerical examples are in a state of plane-stress.

Table 1: Material parameters

E	ν	σ_0	Q_∞	b	C_1	
71.1 GPa	0.33	310 MPa	135.5 MPa	37.32	45 GPa	
C_2	C_3	γ_1	γ_2	γ_3	τ_{\max}	
6.7 GPa	2.15 GPa	6000	290	8	500 MPa	
β	G_c	K_c^{CZ}	K_c^{ITLS}	c_d	c	m
1.66	19 Nmm^{-1}	10^7 N/mm^3	10^8 N/mm^3	30	3.634×10^{-8}	3.372

5.1. Mode I linear elastic

The centre crack specimen (CCS) given in Fig. 11 is considered for the mode I linear elastic case. Here, the half crack length a has an initial value of 5 mm. The applied cyclic stress σ has a maximum value of 100 MPa and the load ratio R is equal to 0.1. The main point of interest is the SIF. If both models can correctly capture the SIF, then their fatigue behaviour, for which the Paris equation is used, should be accurate as well. In this numerical example an elastic bulk material is considered.

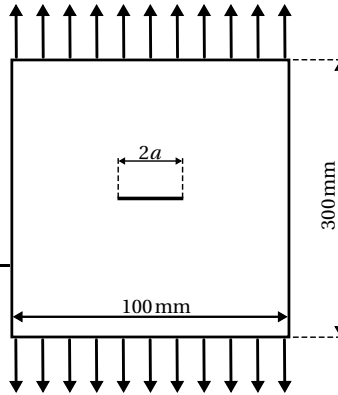


Figure 11: Centre crack specimen

The models are compared against an analytical relation from linear elastic fracture mechanics [58], indicated with "Ana" in the upcoming figures, that can determine the stress intensity factor for the presented CCS:

$$K = \sigma \sqrt{\pi a} \left(\sec \frac{\pi a}{W} \right)^{1/2} \quad (2.18)$$

where W is the width of the specimen.

The stress intensity factor versus crack length for the constant amplitude case is given in Fig. 12a. All three lines for K_{max} and K_{min} are on top of each other, showing that both the CZ model and the ITLS method are accurate. Here, the ERR, and thus the SIF for the CZ model, is calculated using the single point (SP) approach.

The overload case is similar to the constant amplitude example except for the application of an overload of 1.5 times the constant amplitude load applied at a crack length of 8 mm. The results are given in Fig. 12b. Both models and the analytical relation show an increase in the SIF when the overload is applied. After the overload, the SIF is expected to go back to the constant amplitude line, as is seen for the analytical relation and the ITLS method. However, the CZ model shows different behaviour with a temporary increase in SIF after the application of the overload.

The cause for this discrepancy is visualized in Fig. 13, which shows the traction-separation law at the physical crack tip, where the area below the curve is defined as G_{SP}

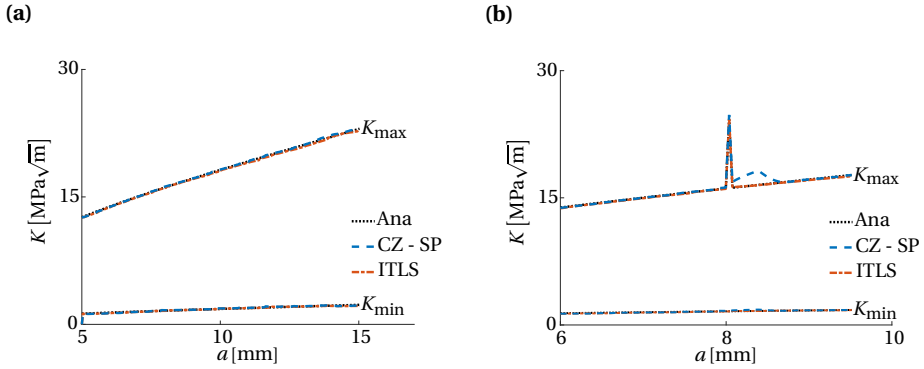


Figure 12: (a) The stress intensity factor K versus crack length for (a) a purely constant amplitude load and (b) a constant amplitude cyclic load with an overload for the linear elastic centre crack specimen subjected to a constant amplitude load.

2

in the single point method. The second curve gives the traction versus displacement jump of the whole fracture process zone (FPZ), the area below which is the physically correct ERR G_J . The single point method assumes that both curves are identical.

Before the application of the overload both curves are exactly on top of each other, see Fig. 13a. The single point method is correct because all the material points in the fracture process zone are on the static envelope of the cohesive law when considering the maximum applied load. All material points are on the traction-separation law of the physical crack tip, because there the displacement jump is largest. Therefore, only the material point at the physical crack tip has to be considered for determining the ERR. This also holds true for unloading, in which all the material points enter their unloading/reloading branch at the same time. During unloading all the material points in the FPZ are in the same unloading/reloading state of the traction-separation law as the physical crack tip point. Thus all the material points will lie on the inner contour shown in Fig. 5b.

During the overload the entire cohesive zone remains in a critical state and the single point approach still works. After returning to the original load level, all points are unloading. However, when the physical crack tip is then shifted forward, points close to the physical crack tip start to experience an increase in damage while other points remain in the unloading stage. Consequently, the traction-separation law of the physical crack tip no longer represents the whole fracture process zone, which can be seen in Fig. 13b. Therefore, the single point method loses its accuracy when overloads are considered. As soon as the distribution of damage is back to the constant amplitude state, which is reached after multiple physical crack tip propagations, the single point method is working correctly again.

As explained in Section 3.2, the J-integral can also be used to compute the ERR for the cohesive zone model. The J-integral is the area under the traction-separation curve of the whole fracture process zone in Fig. 13. Figure 14 shows that the J-integral does work correctly in the presence of an overload.

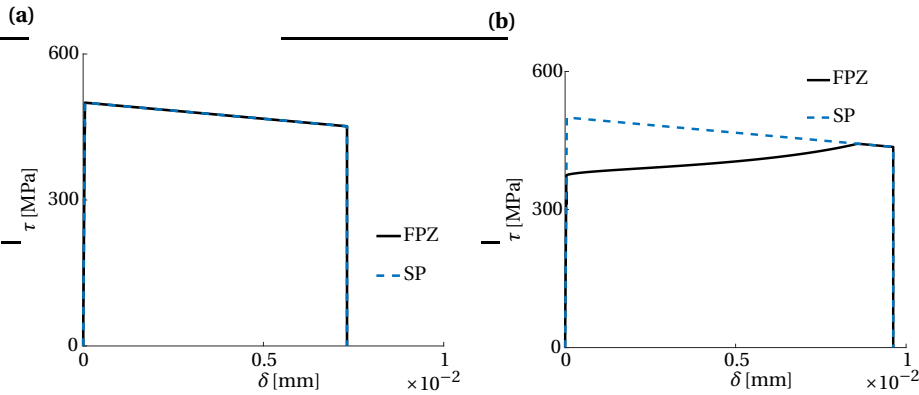


Figure 13: The state of the cohesive law for the physical crack tip and the traction-separation behaviour for the whole process zone just (a) before and (b) after the overload

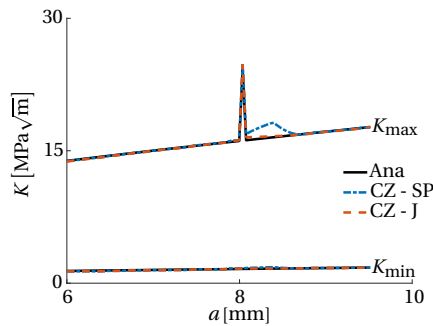


Figure 14: Stress intensity factor versus crack length with the application of an overload for the two different ERR extraction methods for the CZ model

5.2. Mixed-mode linear elastic

In the second numerical example the CZ and ITLS models are compared with a mixed-mode experiment done by Jeong [55]. The specimen with geometry as is given in Fig. 15, is subjected to a uni-axial constant cyclic loading with a maximum applied stress of 110 MPa and a load ratio of 0.1. The inclined initial crack lead to a mixed-mode stress field at the crack tip, causing the crack to grow along a non-trivial path. The initial crack angle α is equal to 22.2° and its initial length a_0 is equal to 4.22 mm. The bulk material behaviour is modelled as purely elastic.

Figure 16 shows that there is a good agreement between the experiment and the models in terms of crack growth rate and crack path. Following Jeong, the crack length is defined as the shortest distance between the physical crack tip and the circumference of the hole. The J-integral ERR and the single point method result in this case in the same curve, because of the constant amplitude loading. The mode I Paris parameters are used, which are fitted for a load ratio of 0.1. With these effective properties and constant am-

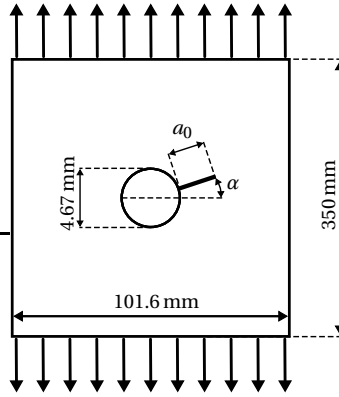


Figure 15: Mixed-mode loading specimen

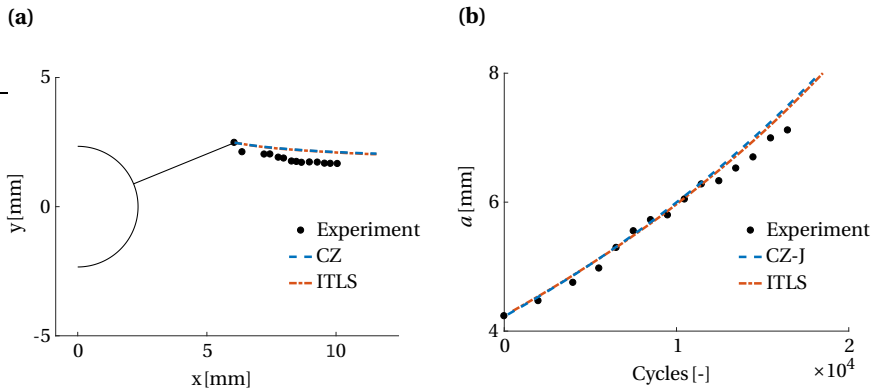


Figure 16: (a) The crack path and (b) the crack growth rate for the mixed-mode specimen for the two numerical models and experiment

plitude loading, there is no need to include plasticity. It is concluded that the maximum principal stress criterion is appropriate for determining the crack growth direction and that the mixed-mode cohesive law in combination with mode I Paris parameters gives the correct crack growth rate.

Figure 17 shows the Von Mises stress field around the crack for the mixed-mode specimen for two different magnifications. The left figure shows that the mesh refinement is only present around the fracture process zone and close to the fully separated crack faces. The right figure shows that the crack can grow through the elements because of the phantom node technique.

5.3. Mode I elastic plastic

Elastic-plastic material behaviour is considered for this numerical example. The CCS geometry from Fig. 11 is considered again. The maximum applied cyclic stress is equal to

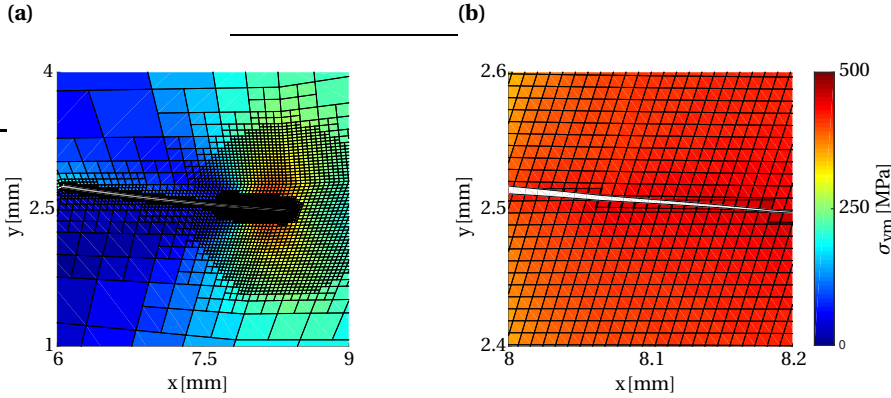


Figure 17: The Von Mises stress field around the crack for two different magnifications

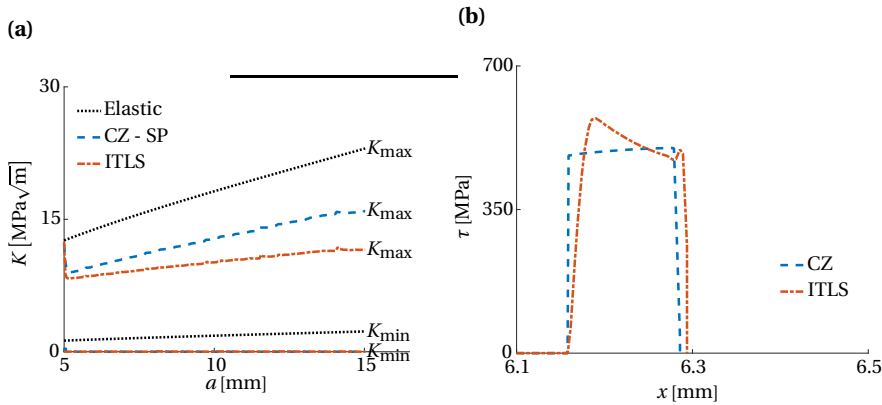


Figure 18: (a) The stress intensity factor versus crack length and (b) the fracture process zone cohesive traction distribution for the elastic-plastic centre crack specimen

100 MPa and the load ratio R is equal to 0.1. The initial crack length is 5 mm. A constant amplitude and overload case are considered. The overload is applied again at a crack length of 8 mm. As stated in Section 3.4, for an elastic-plastic material the SIF is considered to be an effective K . However, the Paris parameters c and m are not calibrated for it and the values given in Table 1 are used. The results are therefore qualitative and not quantitative.

The SIFs for a given crack length under constant amplitude loading are given in Fig. 18a. The CZ model and the ITLS method both show a lower K_{\max} , K_{\min} and ΔK than the elastic solution. Furthermore, due to plasticity the crack faces are compressed together at the minimum applied stress resulting in an ERR, and thus an effective SIF of zero. The single point and the J-integral method for the CZ model give the same SIF values for this case. This means that even for an elastic-plastic material the single point method works correctly.

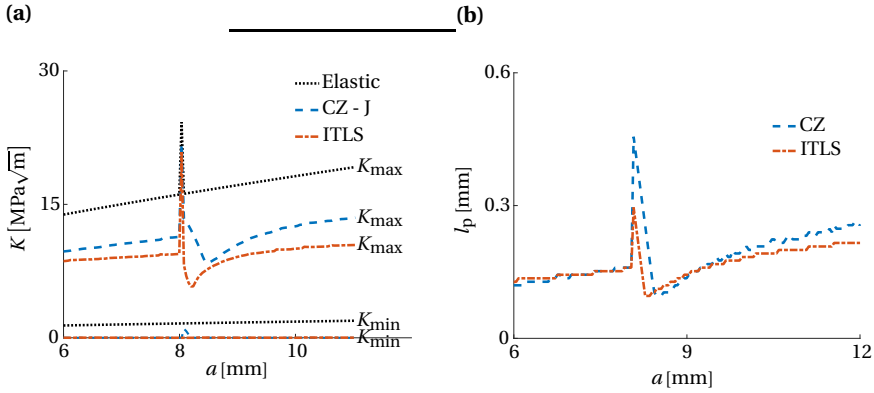


Figure 19: (a) The stress intensity factor and (b) the fracture process zone length versus crack length for the elastic-plastic centre crack specimen

It can also be seen that the CZ model and the ITLS method provide different SIFs. This can be explained by inspecting the actual traction distributions in Fig. 18b where the tractions over the fracture process zone are given for a specific crack length. In addition to having a different traction distribution, the maximum traction for the ITLS is slightly higher than that of the CZ model. Unlike the CZ model, the ITLS is not limited by a maximum stress from a traction-separation law. A larger maximum traction means larger stresses in the neighbouring elements resulting in more plasticity and thus a lower SIF. Note that by changing the damage profile parameter c_p and the cohesive stiffness K_C^{ITLS} , the traction profile can be changed and the maximum traction could be lowered or increased if required. However, obtaining a specific maximum traction is not as straightforward as for the CZ model.

The SIF and the fracture process zone size versus crack length for the overload case are given in Fig. 19. The SIF for the CZ model is now computed by means of the J-integral. At the application of the overload, the SIF increases in magnitude, leading to an increase in plastic zone size and an increase in length of the fracture process zone. After the overload, the physical crack tip has to grow through this zone of increased plasticity, which is pushing the crack faces together more severely than before the overload was applied. Consequently, a reduction in SIF is observed as well as a decrease in the FPZ size.

The stress concentration at the numerical crack tip is decreased, due to the increased plasticity and process zone length. As a result, no numerical crack tip propagation occurs. However, after a certain amount of physical crack tip propagation the stress is large enough again to obtain numerical crack tip propagation. From this point on, the SIF and FPZ size increase gradually until they reach the constant amplitude level. These qualitative observations agree with experiments with overloads [59, 60].

Figure 20 shows a comparison for both models with and without an overload. It can be seen that the crack growth rate is slowed down after the application of an overload, which is beneficial for the fatigue life. Furthermore, there is a difference between the CZ model and the ITLS method, which is attributed to both models using the same Paris

parameters. These parameters should actually be tuned separately for both models such that their model specific plastic behaviour is taken into account. However, here the comparison is purely qualitative and therefore calibration is not performed.

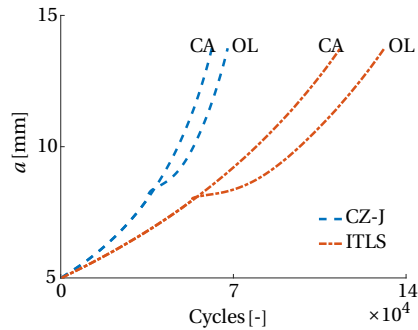


Figure 20: Comparison of the crack length versus amount of cycles with and without an overload

6. Conclusions

This study presented a new approach for fatigue crack propagation in ductile materials. The approach is built in a phantom-node framework enabling arbitrary crack growth direction. Adaptive meshing is applied to keep the simulations efficient. The FPZ ahead of the physical crack tip is captured by means of cohesive tractions. As a result, there are two different crack tips, being the macro or physical crack tip and the fictitious or numerical crack tip. The two crack tips have different criteria for propagation. Consequently, there is no need to define a fracture process zone size, as it automatically follows from the simulation.

The tractions in the FPZ are computed with two different models, being a cohesive zone model and an interfacial thick level set model. The main difference between the two is on how the damage is defined. For the cohesive zone model the damage follows from a traction-separation law, while for the interfacial thick level set the damage profile over the fracture process zone is pre-defined.

The two models result in different traction distributions over the FPZ and therefore, in the case of an elastic-plastic material, also a different distribution of plasticity. As a result, the SIFs for the two models are not the same for a given crack length and both models require a different set of Paris parameters. Furthermore, it is observed that it is not straightforward to control the maximum cohesive traction, and thus the amount of plasticity, for the ITLS method in comparison to the cohesive zone model.

Both models show good agreement with a mode I analytical relation and a mixed-mode experiment. Furthermore, it is shown that the presented models can also capture crack retardation due to an overload when the J-integral is employed for the ERR extraction. However, extracting the ERR from the traction-separation law of the physical crack tip for the cohesive zone model only gives correct results in the case of constant amplitude

loading, irrespective of using an elastic or an elastic-plastic material.

Acknowledgments

This research is part of the EUROS program, which is supported by NWO domain Applied and Engineering Sciences and partly funded by the Ministry of Economic Affairs of the Netherlands.

References

- [1] J. Qian and A. Fatemi, *Mixed mode fatigue crack growth: A literature survey*, Engineering Fracture Mechanics **55**, 969 (1996).
- [2] W. Elber, *Fatigue crack closure under cyclic tension*, Engineering Fracture Mechanics **2**, 37 (1970).
- [3] W. Elber, *The significance of fatigue crack closure*, in *Damage tolerance in aircraft structures* (ASTM International, 1971).
- [4] P. Paris and F. Erdogan, *A critical analysis of crack propagation laws*, Journal of Basic Engineering **85**, 528 (1963).
- [5] K. Tanaka, *Fatigue crack propagation from a crack inclined to the cyclic tensile axis*, Engineering Fracture Mechanics **6**, 493 (1974).
- [6] O. Wheeler, *Spectrum loading and crack growth*, Journal of Basic Engineering **94**, 181 (1972).
- [7] B. Yuen and F. Taheri, *Proposed modifications to the wheeler retardation model for multiple overloading fatigue life prediction*, International Journal of Fatigue **28**, 1803 (2006).
- [8] I. Singh, B. Mishra, S. Bhattacharya, and R. Patil, *The numerical simulation of fatigue crack growth using extended finite element method*, International Journal of Fatigue **36**, 109 (2012).
- [9] H. Pathak, A. Singh, and I. Singh, *Fatigue crack growth simulations of 3-D problems using XFEM*, International Journal of Mechanical Sciences **76**, 112 (2013).
- [10] J. Rice, *A path independent integral and the approximate analysis of strain concentration by notches and cracks*, Journal of Applied Mechanics **35**, 379 (1968).
- [11] G. Wells and L. Sluys, *A new method for modelling cohesive cracks using finite elements*, International Journal for Numerical Methods in Engineering **50**, 2667 (2001).
- [12] J. Mergheim, E. Kuhl, and P. Steinmann, *A finite element method for the computational modelling of cohesive cracks*, International Journal for Numerical Methods in Engineering **63**, 276 (2005).
- [13] F. van der Meer, C. Oliver, and L. Sluys, *Computational analysis of progressive failure in a notched laminate including shear nonlinearity and fiber failure*, Composites Science and Technology **70**, 692 (2010).
- [14] D. Dugdale, *Yielding of steel sheets containing slits*, Journal of the Mechanics and Physics of Solids **8**, 100 (1960).
- [15] G. Barenblatt, *The mathematical theory of equilibrium cracks in brittle fracture*, (Elsevier, 1962) pp. 55 – 129.

- [16] A. Needleman, *An analysis of decohesion along an imperfect interface*, International Journal of Fracture **42**, 21 (1990).
- [17] W. Li and T. Siegmund, *An analysis of crack growth in thin-sheet metal via a cohesive zone model*, Engineering Fracture Mechanics **69**, 2073 (2002).
- [18] C. Chen, O. Kolednik, J. Heerens, and F. Fischer, *Three-dimensional modeling of ductile crack growth: Cohesive zone parameters and crack tip triaxiality*, Engineering Fracture Mechanics **72**, 2072 (2005).
- [19] B. Bak, A. Turon, E. Lindgaard, and E. Lund, *A simulation method for high-cycle fatigue-driven delamination using a cohesive zone model*, International Journal for Numerical Methods in Engineering **106**, 163 (2015).
- [20] P. Harper and S. Hallett, *A fatigue degradation law for cohesive interface elements - development and application to composite materials*, International Journal of Fatigue **32**, 1774 (2010).
- [21] L. Kawashita and S. Hallett, *A crack tip tracking algorithm for cohesive interface element analysis of fatigue delamination propagation in composite materials*, International Journal of Solids and Structures **49**, 2898 (2012).
- [22] E. Iarve, K. Hoos, M. Braginsky, E. Zhou, and D. Mollenhauer, *Progressive failure simulation in laminated composites under fatigue loading by using discrete damage modeling*, Journal of Composite Materials **51**, 2143 (2017).
- [23] B. Yang, S. Mall, and K. Ravi-Chandar, *A cohesive zone model for fatigue crack growth in quasibrittle materials*, International Journal of Solids and Structures **38**, 3927 (2001).
- [24] O. Nguyen, E. Repetto, M. Ortiz, and R. Radovitzky, *A cohesive model of fatigue crack growth*, International Journal of Fracture **110**, 351 (2001).
- [25] K. Roe and T. Siegmund, *An irreversible cohesive zone model for interface fatigue crack growth simulation*, Engineering Fracture Mechanics **70**, 209 (2003).
- [26] A. Ural, V. R. Krishnan, and K. D. Papoulia, *A cohesive zone model for fatigue crack growth allowing for crack retardation*, International Journal of Solids and Structures **46**, 2453 (2009).
- [27] H. Jiang, X. Gao, and T. Srivatsan, *Predicting the influence of overload and loading mode on fatigue crack growth: A numerical approach using irreversible cohesive elements*, Finite Elements in Analysis and Design **45**, 675 (2009).
- [28] S. Silitonga, J. Maljaars, F. Soetens, and H. Snijder, *Numerical simulation of fatigue crack growth rate and crack retardation due to an overload using a cohesive zone model*, in *11th International Fatigue Congress*, Advanced Materials Research, Vol. 891 (Trans Tech Publications, 2014) pp. 777–783.
- [29] M. Latifi, F. van der Meer, and L. Sluys, *An interface thick level set model for simulating delamination in composites*, International Journal for Numerical Methods in Engineering **111**, 303 (2017).

-
- [30] L. Voormeeren, F. van der Meer, J. Maljaars, and L. Sluys, *A new method for fatigue life prediction based on the thick level set approach*, Engineering Fracture Mechanics **182**, 449 (2017).
- [31] Y. Liu, F. van der Meer, and L. Sluys, *Cohesive zone and interfacial thick level set modeling of the dynamic double cantilever beam test of composite laminate*, Theoretical and Applied Fracture Mechanics **96**, 617 (2018).
- [32] N. Moës, C. Stolz, P.-E. Bernard, and N. Chevaugeon, *A level set based model for damage growth: The thick level set approach*, International Journal for Numerical Methods in Engineering **86**, 358 (2011).
- [33] P. Bernard, N. Moës, and N. Chevaugeon, *Damage growth modeling using the thick level set (TLS) approach: Efficient discretization for quasi-static loadings*, Computer Methods in Applied Mechanics and Engineering **233 - 236**, 11 (2012).
- [34] T. Belytschko and T. Black, *Elastic crack growth in finite elements with minimal remeshing*, International Journal for Numerical Methods in Engineering **45**, 601 (1999).
- [35] N. Moës, J. Dolbow, and T. Belytschko, *A finite element method for crack growth without remeshing*, International Journal for Numerical Methods in Engineering **46**, 131 (1999).
- [36] N. Moës and T. Belytschko, *Extended finite element method for cohesive crack growth*, Engineering Fracture Mechanics **69**, 813 (2002).
- [37] J. Unger, S. Eckardt, and C. Könke, *Modelling of cohesive crack growth in concrete structures with the extended finite element method*, Computer Methods in Applied Mechanics and Engineering **196**, 4087 (2007).
- [38] A. Hansbo and P. Hansbo, *An unfitted finite element method, based on nitsche's method, for elliptic interface problems*, Computer Methods in Applied Mechanics and Engineering **191**, 5537 (2002).
- [39] A. Hansbo and P. Hansbo, *A finite element method for the simulation of strong and weak discontinuities in solid mechanics*, Computer methods in applied mechanics and engineering **193**, 3523 (2004).
- [40] J. Song, P. Areias, and T. Belytschko, *A method for dynamic crack and shear band propagation with phantom nodes*, International Journal for Numerical Methods in Engineering **67**, 868 (2006).
- [41] F. van der Meer and L. Sluys, *A phantom node formulation with mixed mode cohesive law for splitting in laminates*, International Journal of Fracture **158**, 107 (2009).
- [42] N. Palle and J. Dantzig, *An adaptive mesh refinement scheme for solidification problems*, Metallurgical and Materials Transactions A **27**, 707 (1996).
- [43] D. Greaves and A. Borthwick, *Hierarchical tree-based finite element mesh generation*, International Journal for Numerical Methods in Engineering **45**, 447 (1999).

- [44] A. Tabarraei and N. Sukumar, *Adaptive computations on conforming quadtree meshes*, Finite Elements in Analysis and Design **41**, 686 (2005), the Sixteenth Annual Robert J. Melosh Competition.
- [45] J. Chaboche, *Constitutive equations for cyclic plasticity and cyclic viscoplasticity*, International Journal of Plasticity **5**, 247 (1989).
- [46] J. Chaboche, *On some modifications of kinematic hardening to improve the description of ratchetting effects*, International Journal of Plasticity **7**, 661 (1991).
- [47] G. Wells, L. Sluys, and R. de Borst, *Simulating the propagation of displacement discontinuities in a regularized strain-softening medium*, International Journal for Numerical Methods in Engineering **53**, 1235 (2002).
- [48] G. Meschke and P. Dumstorff, *Energy-based modeling of cohesive and cohesionless cracks via X-FEM*, Computer Methods in Applied Mechanics and Engineering **196**, 2338 (2007).
- [49] G. Ruiz, A. Pandolfi, and M. Ortiz, *Three-dimensional cohesive modeling of dynamic mixed-mode fracture*, International Journal for Numerical Methods in Engineering **52**, 97 (2001).
- [50] F. Erdogan and G. C. Sih, *On the crack extension in plates under plane loading and transverse shear*, Journal of basic engineering **85**, 519 (1963).
- [51] S. Biner, *Fatigue crack growth studies under mixed-mode loading*, International Journal of Fatigue **23**, 259 (2001).
- [52] N. Moës, A. Gravouil, and T. Belytschko, *Non-planar 3D crack growth by the extended finite element and level sets - part I: Mechanical model*, International Journal for Numerical Methods in Engineering **53**, 2549 (2002).
- [53] A. Gravouil, N. Moës, and T. Belytschko, *Non-planar 3D crack growth by the extended finite element and level sets - part II: Level set update*, International Journal for Numerical Methods in Engineering **53**, 2569 (2002).
- [54] E. Abdollahi and T. N. Chakherlou, *Numerical and experimental study of ratchetting in cold expanded plate of Al-alloy 2024-T3 in double shear lap joints*, Fatigue & Fracture of Engineering Materials & Structures **41**, 41 (2018).
- [55] D. Jeong, *Mixed mode fatigue crack growth in test coupons made from 2024-T3 aluminum*, Theoretical and Applied Fracture Mechanics **42**, 35 (2004).
- [56] J. Davis, ed., *Metals handbook* (ASM International, 1998).
- [57] T. Dursun and C. Soutis, *Recent developments in advanced aircraft aluminium alloys*, Materials & Design (1980-2015) **56**, 862 (2014).
- [58] T. Anderson, *Fracture mechanics: Fundamentals and applications* (Taylor and Francis, 2005).

- [59] W. Geary, *A review of some aspects of fatigue crack growth under variable amplitude loading*, International Journal of Fatigue **14**, 377 (1992).
- [60] L. Borrego, J. Ferreira, J. P. da Cruz, and J. Costa, *Evaluation of overload effects on fatigue crack growth and closure*, Engineering Fracture Mechanics **70**, 1379 (2003).

3

A cohesive XFEM model for simulating fatigue crack growth under various load conditions

R. Dekker^a , F.P. van der Meer^a, J. Maljaars^{b,c}, L.J. Sluys^a

^a Faculty of Civil Engineering and Geosciences, Delft University of Technology, Delft, The Netherlands

^b Faculty of Built Environment, Eindhoven University of Technology, Eindhoven, The Netherlands

^c Structural reliability, TNO ,Delft, The Netherlands

ABSTRACT

This study presents calibration and validation of a cohesive extended finite element model for fatigue crack propagation in ductile materials. The approach relies on a separation between plasticity around the crack tip and fatigue crack growth at the crack tip such that the influence of plasticity on fatigue driving forces is predicted. This implies that characterization of crack growth requires effective Paris parameters. It is shown that the calibrated model can capture fatigue crack growth behaviour in ductile materials for in-phase and out-of-phase biaxial fatigue loading as well as in-phase biaxial loading with an overload.

1. Introduction

Various structures such as vehicles, bridges and wind turbines, are subjected to cyclic loading. It is common that their fatigue crack propagation behaviour is simulated with models that are only valid for mode I constant amplitude loading. However, in reality, the applied cyclic loading can vary in direction, order and magnitude. Uncertainty on how these effects should be accounted for in computational models hampers an accurate fatigue life prediction.

In literature, most research beyond standard constant amplitude loading has been done for overloading and in-phase mixed mode loading. An overload can create a significant crack growth retardation effect, often attributed to plasticity induced crack closure [1–3]. On the other hand, a change in loading direction can cause a mixed-mode stress field around the crack tip, changing the crack growth direction [4, 5].

The developed overload models generally make use of a cohesive zone [6–11]. The effect of an overload is captured by including plastic behaviour, either in the cohesive zone or in the bulk material. For these models, the calibration of parameters is generally not extensively discussed.

Mixed-mode loading models mainly utilize the eXtended Finite Element Method (XFEM) [12, 13] to enable crack growth through elements [14–17]. However, only in-phase mixed-mode loading has been considered in such models whereas out-of-phase mixed-mode has mainly been limited to experimental research [5, 18–20]. The research on modelling this behaviour is limited to an analysis of different crack path prediction methods [20, 21].

In recent work, the authors have developed a thick level set model that can capture the effect of overloads by separating plasticity around the crack tip from fatigue crack growth at the crack tip [22]. Afterwards, this approach has been used for a cohesive XFEM model, employing the phantom node version of the XFEM [23–27], such that both the effects of overloading and mixed-mode loading can be captured [28]. In this model, a cohesive zone is used to approximate the damage behaviour in front of the physical or macroscopic crack tip. The energy release rate (ERR) is determined by means of the J-integral, which is linked to the Paris equation to compute the fatigue crack growth rate. The present study takes the cohesive XFEM formulation from [28] as a starting point and investigates its validity for capturing the physics of fatigue crack growth under various loading conditions. Specifically, this paper is focused on the determination and calibration of the cohesive zone parameters in combination with the Paris equation to predict fatigue crack growth, with special attention for out-of-phase loading and bi-axial loading in combination with overloading.

The paper starts with an overview of the numerical framework followed by a description of the behaviour of the bulk material and the cohesive zone. Subsequently, the crack tip propagation criteria are discussed. Next, the fracture parameters are determined, in which the tensile strength and a set of plastic Paris parameters require calibration. Finally, two numerical examples are presented to validate the model and to show the ob-

jectivity of the parameters. The numerical examples include out-of-phase biaxial loading and in-phase biaxial loading with a single overload.

2. Numerical framework

A cracked medium with an elastic-plastic bulk material, as shown in Fig. 1, is examined. The crack propagates due to an applied cyclic loading. The non-linear fracture process zone ahead of the physical crack tip is captured by means of a cohesive zone, which is illustrated in Fig. 2. The numerical crack, i.e. the XFEM discontinuity, extends beyond the physical crack tip to include the cohesive zone. The tip of the discontinuity is referred to as the numerical crack tip. The cohesive tractions are large near the numerical crack tip and are zero at the physical crack tip.

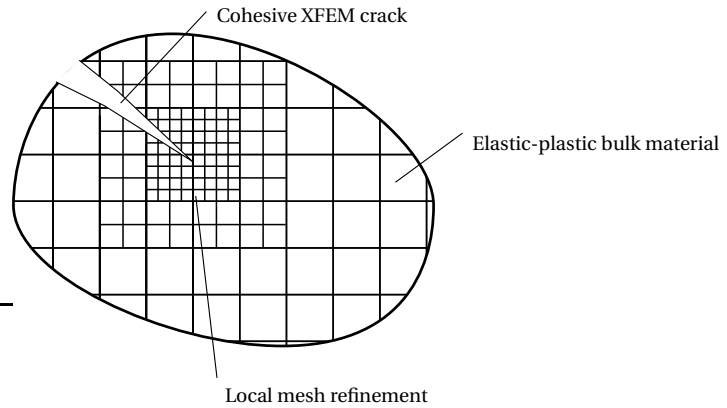


Figure 1: Numerical framework

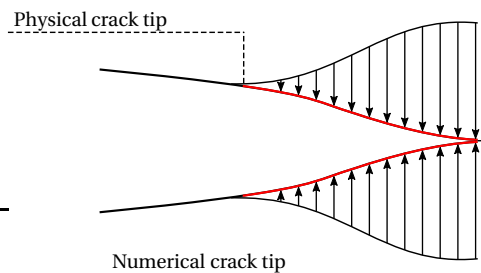


Figure 2: Cohesive zone

Fig. 1 also illustrates two characteristics of the numerical framework upon which the fatigue crack growth model is built. Both aspects follow from not knowing the crack path a priori. Firstly, there is the ability of XFEM for a discontinuity to be present along a non-predefined crack path running through the elements. Secondly, in order to correctly capture the crack tip behaviour, small elements are required in this region. However, when it

is unknown where the crack will grow, small elements are required everywhere, which increases computation time significantly. This is addressed by making use of an adaptive meshing technique [29–31], which ensures the use of small elements only around the crack tip and larger elements elsewhere in order to improve computational efficiency.

3. Material behaviour

The bulk material and the cohesive zone both have their own set of constitutive relations. Consequently, the interaction between the bulk material and the cohesive zone dictates the crack growth behaviour. This section first describes the relations used for the bulk material, followed by those employed for the cohesive zone.

3.1. Bulk material

A bulk material having an elastic-plastic material response is considered. The elastic response is captured using Hooke's law which requires the Young's modulus E and the Poisson ratio ν . The plastic response is modelled using both isotropic and kinematic hardening such that plastic flow under cyclic loading can be captured. The yield surface is described by means of the Von Mises criterion:

$$f = \sqrt{\frac{2}{3} (\mathbf{s} - \boldsymbol{\xi}) : (\mathbf{s} - \boldsymbol{\xi})} - \sigma_y \quad (3.1)$$

where \mathbf{s} is the deviatoric stress and $\boldsymbol{\xi}$ the deviatoric back-stress. A non-linear isotropic hardening rule [32] is used to describe the evolution of the yield stress σ_y :

$$\sigma_y = \sigma_0 + Q_\infty \left(1 - e^{-b\bar{\epsilon}^p}\right) \quad (3.2)$$

where σ_0 and Q_∞ are the initial yield stress and the limit value for the yield stress increase, respectively. The measure for the rate of change of the yield surface is indicated by b . The equivalent plastic strain increment $d\bar{\epsilon}^p$ is a function of the plastic strain increment $d\epsilon^p$:

$$d\bar{\epsilon}^p = \sqrt{\frac{2}{3} d\epsilon^p : d\epsilon^p} \quad (3.3)$$

The kinematic hardening rule is defined as [33]:

$$d\boldsymbol{\xi} = \sum_{i=1}^2 \left(\frac{2}{3} C_i d\epsilon^p - \gamma_i \boldsymbol{\xi}_i d\bar{\epsilon}^p \right) \quad (3.4)$$

where γ_i is the non-linear kinematic hardening coefficient and C_i is the linear one.

3.2. Cohesive zone model

In the cohesive zone model each integration point on the crack is assigned a static cohesive law from which the traction and the stiffness degradation through a damage parameter are computed. Figure 3 shows the bilinear cohesive law that is used in this study.

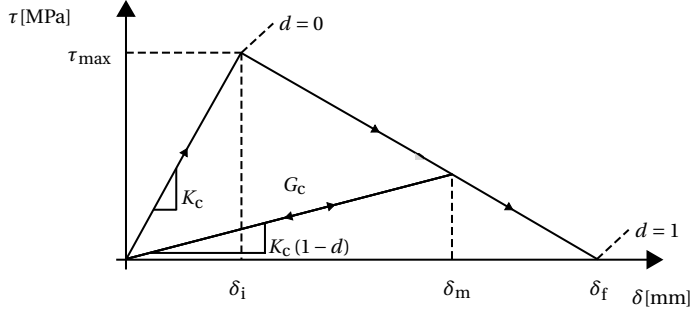


Figure 3: Bilinear cohesive law

A mixed-mode formulation is used in which the effective traction τ is a function of the effective displacement jump δ , which is defined as [34, 35]:

$$\delta = \sqrt{\langle \delta_n \rangle^2 + \beta^2 \delta_s^2} \quad (3.5)$$

where β is equal to the ratio between the tensile and shear strength of the material. The normal and tangential displacement jumps are indicated by δ_n and δ_s , respectively.

The maximum effective traction stress τ_{\max} is equal to the material tensile strength and the critical ERR for mode I, indicated by G_c , is equal to the area under the curve of the cohesive law. The maximum effective displacement jump that has been reached by a material point on the crack is defined by δ_m , which has a corresponding damage d that is given by:

$$d = \frac{\delta_f(\delta_m - \delta_i)}{\delta_m(\delta_f - \delta_i)} \quad \text{for } \delta_m \geq \delta_i \quad (3.6)$$

from which follows that an increase in δ_m results in an increase in d . Here, δ_i is the fracture initiation displacement jump and δ_f the final failure displacement jump, which are computed from the values of τ_{\max} , G_c and the initial cohesive stiffness K_c .

The damage starts to increase once the effective displacement jump exceeds δ_i and reaches its maximum value of one for a displacement jump equal to δ_f . K_c is multiplied with $(1 - d)$ to account for the accumulated damage. As a result, the effective traction-displacement relations are given by:

$$\tau = \begin{cases} K_c \delta & \delta_m < \delta_i \\ K_c (1 - d) \delta & \delta_m \geq \delta_i \\ 0 & \delta_m \geq \delta_f \end{cases} \quad (3.7)$$

The tractions in the normal direction τ_n and sliding or tangential direction τ_s are computed from the effective traction:

$$\tau_n = \begin{cases} \frac{\tau}{\delta_m} \delta_n & \delta_n \geq 0 \\ K_c \delta_n & \delta_n < 0 \end{cases} \quad (3.8)$$

$$\tau_s = \beta^2 \frac{\tau}{\delta_m} \delta_s \quad (3.9)$$

The initial cohesive stiffness is used to calculate the normal traction in the case of a negative displacement jump, irrespective of the value of accumulated damage. Contact between the two crack faces is ensured by means of a large initial stiffness which ensures that any negative normal displacement jumps remain small. Consequently, K_c should be sufficiently large such that the global response is not influenced by its exact value.

Extraction of the ERR is done by computing the J-integral around the interface elements by integrating the traction-separation relation along the fracture process zone following Bak et al. [36]:

$$G = - \int_0^{l_p} \tau \frac{\partial \delta}{\partial \phi} d\phi \quad (3.10)$$

where l_p is the total length of the cohesive zone and ϕ the variable that runs from 0 at the physical crack tip to l_p at the numerical crack tip. For a fully developed cohesive zone, as obtained during quasi-static crack growth, this G is equal to G_c . However, for fatigue crack growth G is generally lower than G_c .

3.3. Fatigue crack relation

The crack growth rate is computed by means of the Paris equation [37]:

$$\frac{da}{dN} = c (\Delta K)^m \quad (3.11)$$

where N is the number of cycles, a is the crack length and ΔK is the Stress Intensity Factor (SIF) range. The Paris constant and exponent are indicated by c and m .

The cohesive zone gives the ERR for a given state of the model. For elastic materials the SIF can simply be converted to the ERR by means of the following equation:

$$K = \sqrt{EG} \quad (3.12)$$

which is only valid for the state of plane stress, although a comparable relation exists for plane strain as well.

The effective displacement jump defined in Eq. (3.5) is used to capture the effect of different mode-mixities on G . Consequently, the mode I Paris parameters are used to determine the fatigue crack growth rate for mixed-mode loading as well. Potentially, the model can be expanded to include roughness induced crack closure by adjusting the cohesive zone behaviour. Plugging Eq. (3.12) into Eq. (3.11) gives the Paris relation as a function of the ERR:

$$\frac{da}{dN} = c_e \left(\sqrt{EG_e^{\max}} - \sqrt{EG_e^{\min}} \right)^{m_e} \quad (3.13)$$

where the subscript e has been added to the Paris parameters and the ERR G to indicate that it concerns an elastic bulk material.

Note that Eq. (3.12) does not result in a real SIF in the case of an elastic-plastic material. Nonetheless, the SIF computed from the ERR for the fracture process zone inside the

elastic-plastic bulk material could still potentially be used as a measure for the magnitude of the crack driving force. Therefore, for an elastic-plastic bulk material, Eq. (3.13) is written as:

$$\frac{da}{dN} = c_p \left(\sqrt{EG_p^{\max}} - \sqrt{EG_p^{\min}} \right)^{m_p} \quad (3.14)$$

where the parameters c_p and m_p require calibration. The subscript p is added to indicate that it holds for an elastic-plastic bulk material. Unlike the c_e and m_e from Eq. (3.13), c_p and m_p cannot be directly identified from experiments as there is no method to measure G_p from experimental observations. It should be mentioned that the common approach where K is related to the force through linear elastic fracture mechanics (LEFM) relations is not without problems either as LEFM theory fails to capture measured stress ratio effects, let alone crack retardation through overloading. In contrast, the G_p from Eq. (3.14) is a quantity that accounts for the shielding effect of the plastic zone.

4. Crack tip propagation

Figure 4 illustrates a cohesive crack in a finite element mesh in which the locations of the numerical and physical crack tip, as well as the cohesive integration points and the regular integration points for several elements are indicated. The arc length of the fracture process zone, indicated with the solid line, is equal to l_p . Complete separation of the crack faces, i.e. damage equal to one, is indicated by the thick dashed line. The magnitude of l_p is determined based on the position of the physical and the numerical crack tip, which both have their own criterion of propagation. The length of the fracture process zone changes as the crack propagates due to the changing stress field around the crack tip. It is noted that both crack tips are only allowed to grow from element boundary to element boundary.

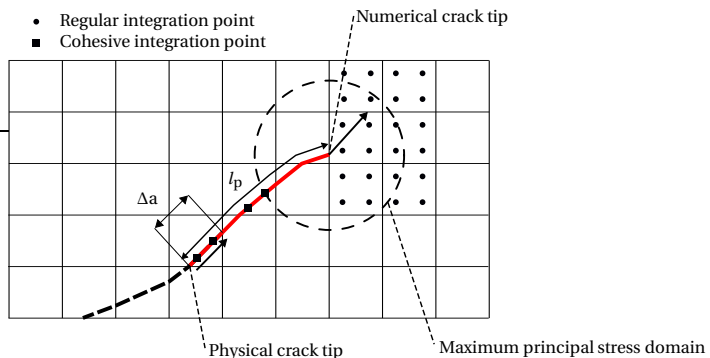


Figure 4: A crack (dashed line) with fracture process zone (solid line) in an extended finite element model framework. Note that this figure is only an illustration. Cohesive integration points are present along the whole crack and regular integration throughout the whole domain.

The numerical crack tip propagates through one element when the maximum principal

stress σ_1 in any integration point located in a small region around the numerical crack tip exceeds the failure stress. The failure stress is equal to τ_{\max} in Fig. 3 and acts as a numerical quantity rather than the value extracted from a 1D tensile test. The small region is taken to have a radius of three times the element size and is indicated in Fig. 4 with the circle around the numerical crack tip. The crack growth direction is computed using the maximum principal stress criterion [38], using a non-local approach [39]. The non-local stress is computed by weighing the state of stress of each integration point located in the neighbourhood of the numerical crack tip with the following equation:

$$w = \frac{l_w}{(2\pi)^{3/2} l_w^3} \exp\left(-\frac{r_w^2}{2l_w^2}\right) \quad (3.15)$$

Here, r_w and l_w are the distance from the numerical crack tip to the considered integration point and the rate of decay of the weight function, respectively. The arrow from the numerical crack tip in Fig. 4 indicates a possible propagation direction.

To obtain fatigue crack growth at $G < G_c$, the physical crack tip is forced forward by a crack length increment Δa by setting the damage value of the process zone element that is next to the current physical crack tip equal to one [40, 41]. The physical crack tip is following the path defined by the numerical discontinuity, as indicated by the arrow from the physical crack tip also shown in Fig. 4. The propagation process of the physical crack tip is performed after each simulated loading cycle. At the post-processing stage, the actual amount of fatigue cycles ΔN that each simulated loading cycle represents is calculated by means of Eq. (3.14) for an elastic-plastic or Eq. (3.13) for an elastic material, which requires Δa , G^{\max} and G^{\min} to be known. The crack growth length Δa is equal to the distance the physical crack tip needs to be shifted forward to reach the next element edge, and G^{\max} and G^{\min} are known because the ERR is evaluated at each time step during the simulated cycle and thus the effective stress intensity range is known as well. By computing the ERR at every time step, it is not necessary to inform the part of the code where the ERR is computed about when boundary conditions are at a maximum or minimum, or even to assume that G^{\max} is synchronized with maximum boundary conditions which would for instance not be the case in the presence of viscoelasticity.

A flow diagram of the whole crack propagation process is given in Fig. 5. Initially the physical crack tip and the numerical crack tip coincide, which means that the simulation starts with a sharp notch without cohesive zone. The numerical process starts with setting the applied loading or loadstep, after which a finite element calculation is performed to compute the displacements, strains and stresses. First, it is monitored if numerical crack tip propagation should be performed. If this is not the case, it will be checked if the current loadstep is the final step of a fatigue load cycle. If this criterion is not met, the ERR is computed and a new load step is introduced. If one of the two criteria is met, either numerical crack tip or physical crack tip propagation is performed, followed by a mesh adaptivity process. More details on the mesh refinement can be found in [28]. The displacements, strains and stresses are then calculated for the same loadstep for this new configuration. Note that it is only possible to meet the cycle end criterion only once for a specific loadstep. Furthermore, a 3D implementation for the current crack growth algorithm is possible following Moes et al. [42, 43].

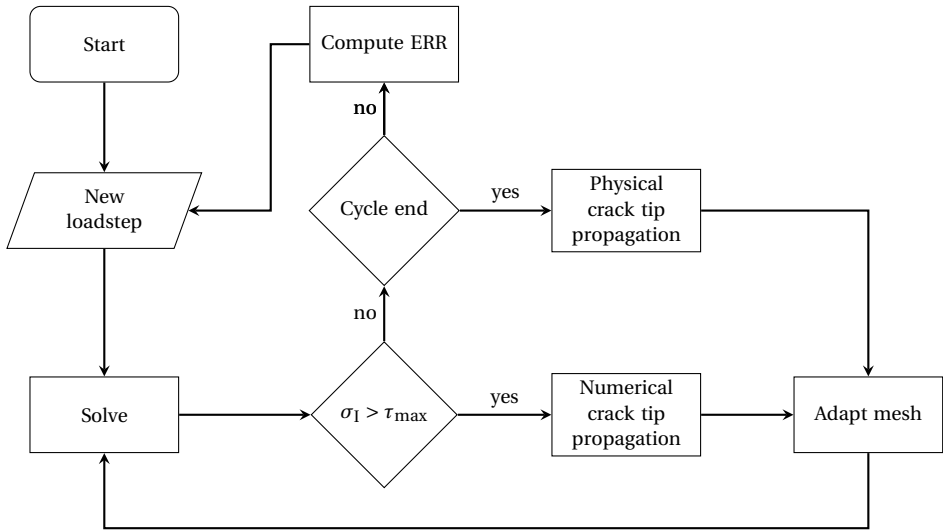


Figure 5: Flow diagram of the fatigue crack propagation model

5. Model calibration

3

Model calibration is performed on the fatigue crack growth experiments reported by Zhao et al. [3] for a 7075-T6 aluminium alloy. The tests were executed on the compact tension specimen given in Fig. 6 with a width W of 50.8 mm and a thickness of 4.76 mm. The crack has an initial length a of 12.8 mm. The applied cyclic load has a load ratio of 0.1 and a maximum applied load P_{\max} of 3 kN. The problem is considered to be in a state of plane stress. The elastic Paris parameters resulting from these tests are given in Table 1. Note that these elastic Paris parameters are computed on the assumption that linear elastic fracture mechanics can be used.

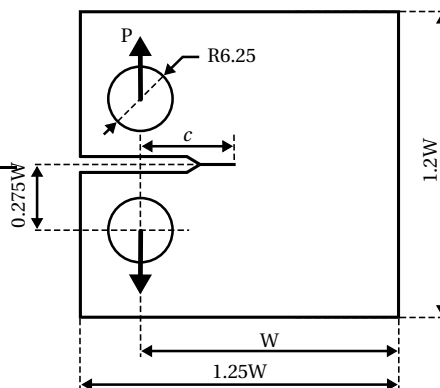


Figure 6: Compact tension specimen

Table 1: Elastic Paris parameters [3]

c_e	m_e
6.78×10^{-8}	3.32

The presented numerical model includes plasticity parameters and cohesive law parameters. The plasticity parameters are obtained from Naderi et al. [44] and are given in Table 2. The cohesive law parameters, which should be calibrated, include the cohesive stiffness K_c , the critical ERR G_c and the tensile strength τ_{\max} . Baseline values of the cohesive zone parameters are given in Table 2 as well, where the parameter β as well as G_c follow from [45]. These baseline values are used in the numerical simulations presented in this paper except when mentioned otherwise. Furthermore, the plastic Paris parameters require calibration as well. The calibration of the cohesive law parameters K_c , G_c and τ_{\max} , and the Paris parameters m_p and c_p will be discussed next.

5.1. Cohesive stiffness

The value of K_c , if chosen sufficiently stiff, should not influence the global response. In order to prove this, a simulation under constant amplitude fatigue loading on the CTS, as defined above, has been performed for varying values of cohesive stiffness. In Fig. 7a the computed ERR is plotted as a function of the crack length, which shows that the effect of the cohesive stiffness on the results is negligible for all values larger or equal to 10^8 N/mm^3 . However, it should be mentioned that choosing a too large value could result in non-convergence of the solution.

5.2. Critical energy release rate

The value of G_c can be determined experimentally. However, its value depends on the material grain direction as well as the amount of plasticity around the crack tip during the test, resulting in different sources giving different values [45–47]. In the present framework where plasticity is separately represented, G_c should not include energy dissipation in the plastic region around the fracture process zone. The value of this parameter is mainly important to determine when fatigue crack growth turns into crack growth under monotonic loading. As shown in Fig. 7b, a change in G_c results in a minimal change in ΔG . Furthermore, because the Paris parameters and τ_{\max} still need to be calibrated after choosing the values for G_c , it is safe to assume that the exact value of G_c does not influence the fatigue behaviour. As mentioned before, the G_c used in this study is taken from [45].

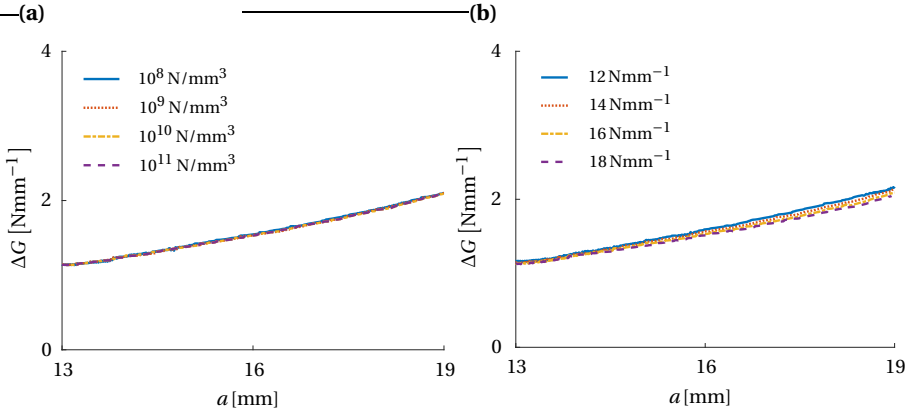


Figure 7: ERR range for different values of (a) K_c and (b) G_c

5.3. Tensile strength and Paris parameters

For fatigue crack growth simulations three parameters remain that require calibration, namely the Paris constant and exponent, and τ_{\max} . However, these parameters are not independent of each other. This is illustrated in Fig. 8, which shows the influence of τ_{\max} on the ERR range. A higher τ_{\max} allows for larger strains and therefore a larger plastic zone, which reduces the ERR. Note that τ_{\max} acts as a calibration parameter and its value does not necessarily have a physical meaning. For reference, the curve for an elastic bulk material is added as well, which can be obtained by an empirical relation [48] or numerically, independent of τ_{\max} . In the case with elastic bulk material, a value for τ_{\max} of 1200 MPa has been used, although in absence of plasticity results are insensitive to the strength as long as it results in a cohesive zone that is sufficiently small compared to specimen dimensions and yet spans several finite elements.

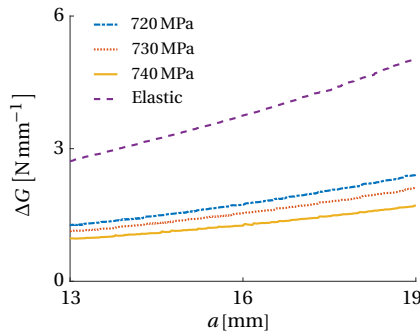


Figure 8: ERR range as function of τ_{\max}

For each value of τ_{\max} , the Paris parameters can be calibrated to a Paris curve, see Eq. (3.13), with the elastic Paris parameters given in Table 1 as input by means of a least square minimization. It should be emphasized that each value of τ_{\max} has its own tuned

set of Paris parameters, which all give the same crack growth rate in the case of constant amplitude loading.

The model parameters cannot be uniquely identified with data from a constant amplitude test. At this point it is still unknown which set of τ_{\max} and Paris parameters should be selected. This selection follows from simulating an overload case, where the data is again taken from an experiment done by Zhao et al. [3]. In this experiment, an overload of 6 kN, which is twice the maximum load in the constant amplitude part, was applied at a crack length of 14.96 mm. Note with respect to the simulation scheme shown in Fig. 5, this overload is a single cycle, and thus no physical crack propagation is done immediately after the overload. First, a constant amplitude load cycle is run before physical crack propagation is performed again.

For every combination of τ_{\max} and corresponding Paris parameters, a different amount of crack retardation is obtained when the overload case is simulated. The set that is able to quantitatively capture the experimentally observed retardation effect is selected. Figure 9 shows crack growth results from simulations where the overload experiment is modelled using different values of τ_{\max} and their respective Paris parameters, as well as using an elastic bulk material as a reference. It can be seen that all parameter sets give a good match with the experiment for the constant amplitude part, while only the parameter set with τ_{\max} equal to 730 MPa agrees with the experimental retardation behaviour. A higher value for τ_{\max} results in too much retardation and a lower value in too little. The elastic material results only in a peak in crack growth rate at the moment the overload is applied, but afterwards no effect is observed, as was expected. In Fig. 9a it can also be observed that the retardation is preceded by a short period of crack acceleration right after the application of the overload. The resolution of experimental measurements is not sufficient to determine whether this effect was also present in the test. However, depending on the material and loading conditions, crack growth acceleration after an overload is not uncommon [49]. Finally, note that the optimal combination of τ_{\max} and Paris parameters depends on the chosen plasticity parameters, of which different values can be found in literature [44, 50, 51]. Also, the numerical fracture process zone length for the specified calibration case is found to be in the order of 0.1 mm.

Table 2: Model parameters

E	ν	σ_0	Q_∞	b	C_1	C_2	γ_1	γ_2
70.94 GPa	0.33	420 MPa	140 MPa	40	175 GPa	9 GPa	3500	180

τ_{\max}	β	G_c	K_c	c_p	m_p
730 MPa	1.73	14.5 N mm ⁻¹	10 ⁸ N/mm ³	2.32 × 10 ⁻⁷	3.29

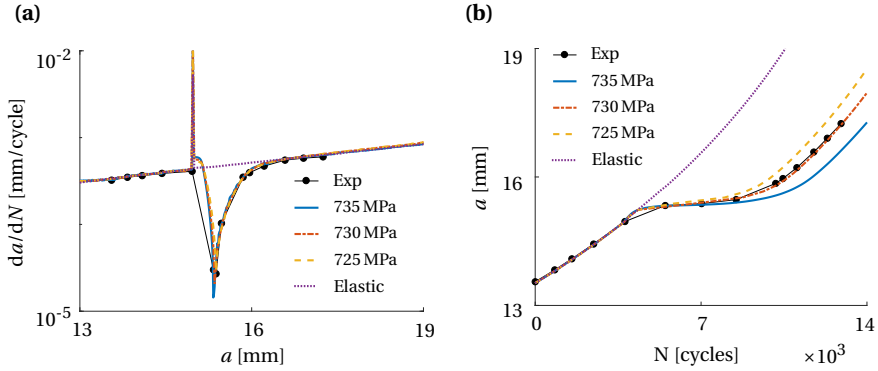


Figure 9: (a) Crack growth rate and (b) number of fatigue cycles for different tensile strength compared against a mode I fatigue overload experiment (Exp) [3]

6. Validation

Fatigue simulations for biaxial fatigue loading are performed and the results are compared against experimental data from literature [5, 52] to investigate whether the calibrated model is valid for more complex load scenarios as well. The tests were performed on the same material as the tests used for the calibration of the model in the previous section. All validation tests consider the notched cruciform specimen given in Fig. 10, which has a rounded square section around the centre which has a smaller thickness t compared to the rest of the specimen. Biaxial cyclic loading is applied where the load cycles in the two directions are either in-phase or out-of-phase with a predefined phase shift. In the case of out-of-phase loading, the vertical load is lagging behind the horizontal one. The numerical analyses are performed using the model parameters from Table 2 as calibrated in Section 5. Furthermore, the same analyses are also executed for an elastic bulk material in order to investigate the influence of plasticity. After that, a bi-axial overload example is simulated and compared against experimental observations. For all these analyses a state of plane stress is assumed.

6.1. Constant amplitude loading

The experimental data for the constant amplitude biaxial fatigue loading examples are taken from literature [5, 52]. Three different types of loading are considered, namely, in-phase loading (IP), 45° out-of-phase loading (OP45) and 90° out-of-phase loading (OP90). The loading ratio is equal to 0.1 and the maximum applied load in both directions is equal to 15 kN.

The experimental data consist out of two or three different runs of the same experiment with considerable scatter between the different runs as shown in Fig. 11a. This scatter can be substantially reduced when starting to count the fatigue cycles from a slightly larger crack length as shown in Fig. 11b, demonstrating a certain initiation life, which could be caused by variation in the notch geometry between different specimens. There-

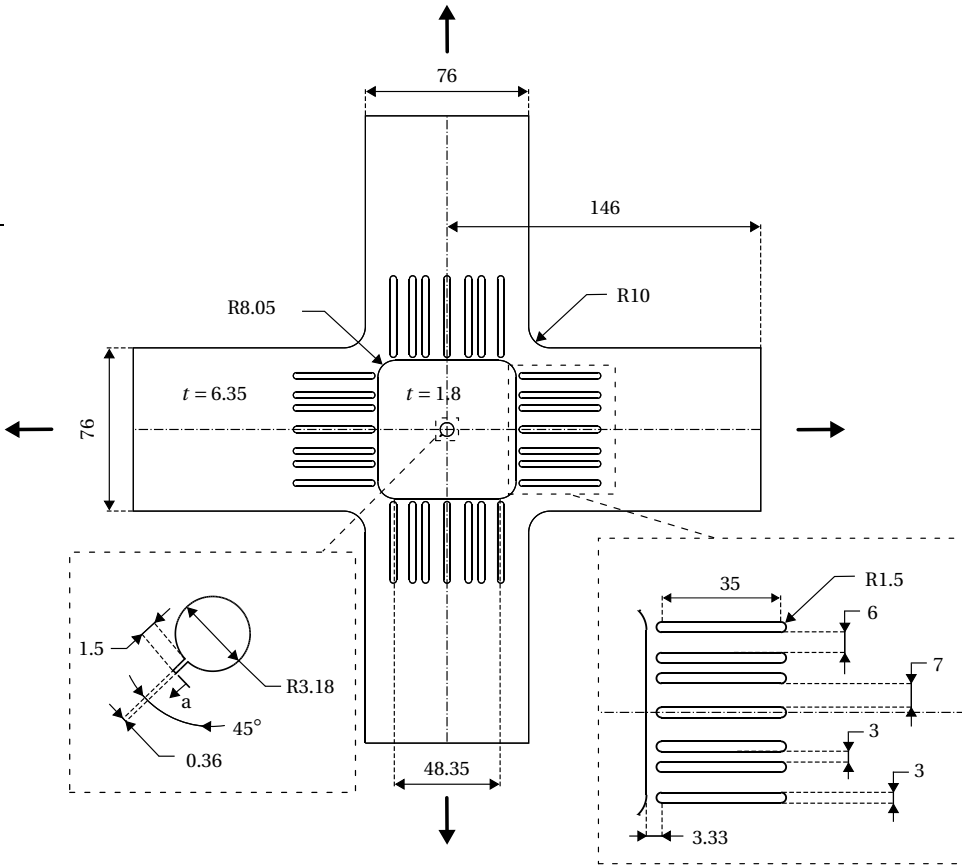


Figure 10: Geometry of cruciform specimen (Dimensions are in millimetres)

fore, the crack growth results are shown from a crack length of 2 mm to ensure that the numerical model is compared to the experiments for the fatigue crack propagation stage and excluding the fatigue initiation stage.

6.1.1. Elastic-plastic bulk material

The comparison of the crack path between the numerical model (Num), employing an elastic-plastic bulk material, and the experimental data (Exp) is shown in Fig. 12a. Only one crack path per loading condition is given in the articles containing the experimental data. The crack path for IP and OP90 show reasonable agreement. It is surprising that experimentally the crack path for OP45 does not lie between the crack paths for OP90 and IP. The simulations do not reproduce this.

Next, Fig. 12b shows the comparison of crack growth as a function of number of load cycles. Here, two lines are included from the numerical model. The dashed line is the result of using the original (orig) plastic Paris parameters previously calibrated on the

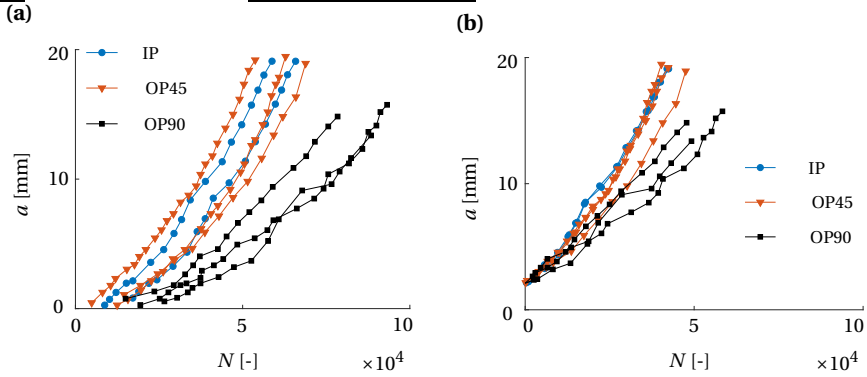


Figure 11: Experimental crack growth data [5, 52] (a) without adjustment and (b) taking 2 mm as a starting point for the fatigue cycle count.

CTS. It can be seen that the number of cycles required to reach a specific crack length is significantly over-predicted with these parameters. This could possibly be attributed to a difference in batch material or a difference in production process between the two specimens.

Here, increasing the Paris constant by 55% for the cruciform specimen to $c_p = 3.6 \times 10^{-7}$ leads to a good agreement for IP loading between the numerical model and the experiment. The newly calibrated Paris constant is used in the following simulations of different cases with the same geometry: OP45, OP90 and IP overload. Using this adjusted (adj) Paris constant for in-phase loading results in the solid line in Fig. 12b, which now shows there is good agreement. Note that re-calibration of the Paris parameters does not affect the crack path in the simulations, because the Paris equation is only used in post-processing to compute the number of cycles required per crack increment.

There is a relatively poor agreement between numerical model and experiment for OP45 as shown in Fig. 12c, which could be expected with the already observed mismatch in crack path. On the other hand, Fig. 12d shows a good agreement with the experiment for OP90.

6.1.2. Elastic bulk material

The same comparison of the numerical model with experiment has been performed considering an elastic bulk material. Here, the Paris parameters from Table 1 are used. The comparison in crack path is given in Fig. 13a. Again, IP and OP90 match relatively well with the experiments while OP45 does not.

Also for the elastic bulk material, using parameters calibrated on the compact tension specimen does not result in a good match in crack growth as function of number of cycles, which is shown by the dashed line in Fig. 13b. Again, in order for the in-phase loading case to agree with the experiment the Paris constant is increased. For the elastic bulk material the Paris constant is increased by 31% to $c_e = 8.88 \times 10^{-8}$. The solid line in

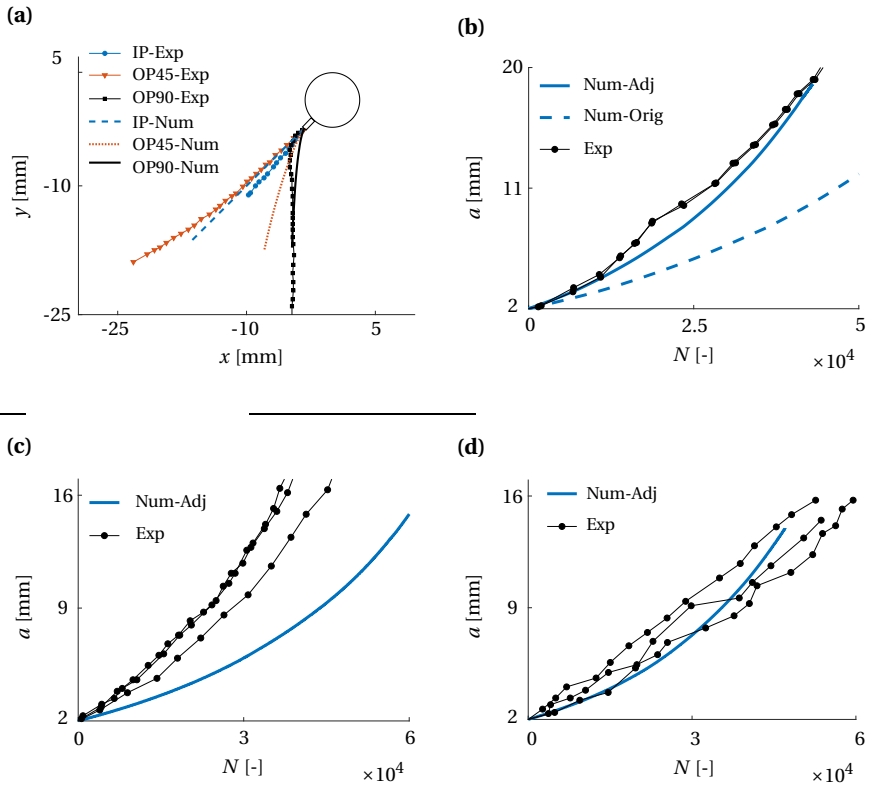


Figure 12: (a) The crack paths and the amount of fatigue cycles for (b) IP, (c) OP45 and (d) OP90 according to the numerical model (Num), using an elastic-plastic bulk material, and experiment (Exp).

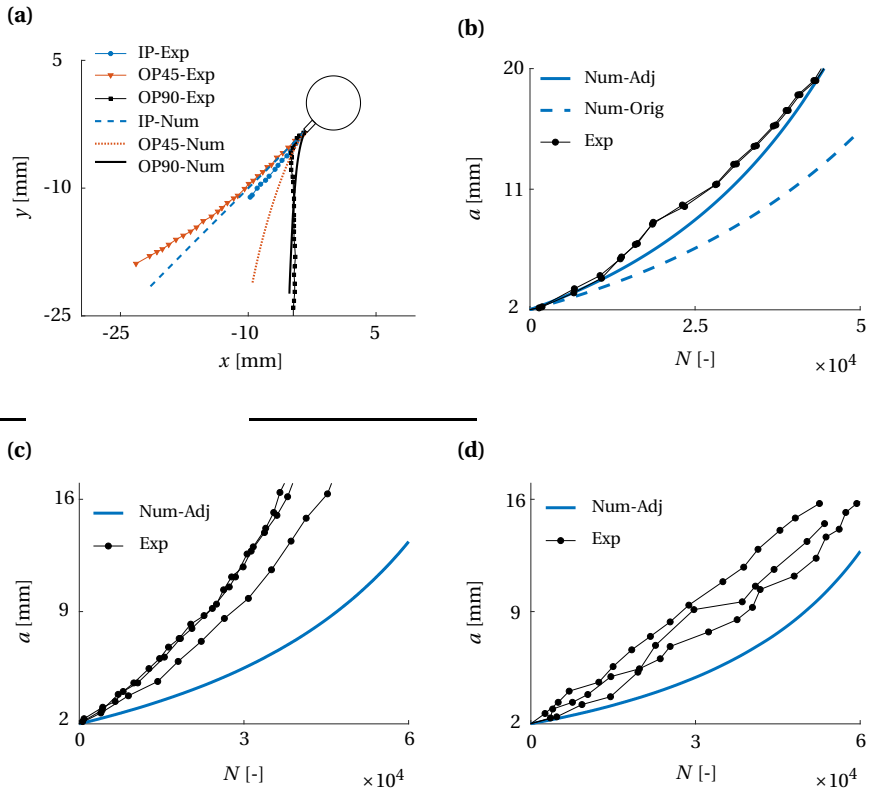


Figure 13: (a) The crack paths and the amount of fatigue cycles for (b) IP, (c) OP45 and (d) OP90 according to the numerical model (Num), using an elastic bulk material, and experiment (Exp).

Fig. 13b shows the cycles versus crack length for the adjusted Paris constant, which now follows the experiment.

The solid lines Figs. 13c and 13d show the crack growth behaviour using the adjusted Paris constant for OP45 and OP90, respectively. Interestingly, neither is in agreement with the experiment, while for the elastic-plastic bulk material OP90 did agree with the experiment. This indicates the need to include elastic-plastic material behaviour when considering out-of-phase loading.

Figure 14 shows the maximum and minimum ERR for the elastic-plastic and the elastic bulk material. It can be seen that the G^{\min} for the elastic-plastic bulk material is zero for all crack lengths due to plasticity induced crack closure. This is not the case for the elastic material, which could potentially explain why using an elastic bulk material in the numerical analyses cannot capture the correct crack growth rate for OP90.

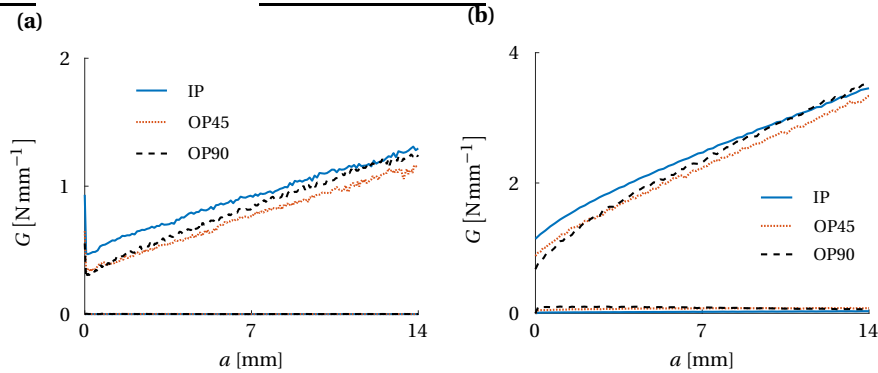


Figure 14: The minimum and maximum ERR versus crack length for (a) the elastic-plastic and (b) the elastic bulk material.

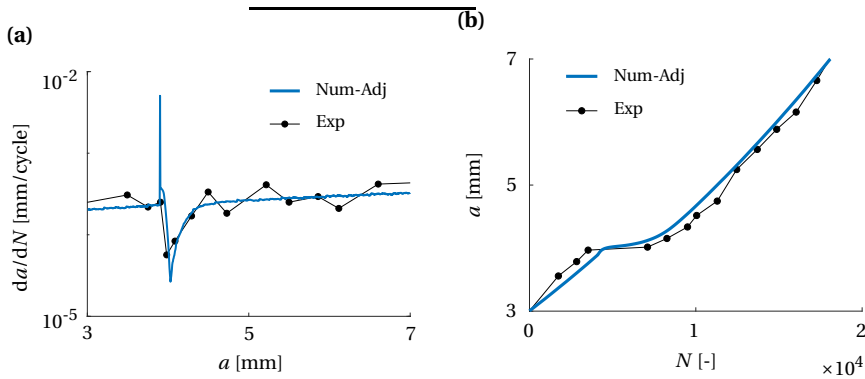


Figure 15: (a) The crack growth rate and (b) the amount of fatigue cycles according to the numerical model (Num), using an elastic-plastic bulk material and the adjusted Paris constant, and experiment.

6.2. Biaxial loading with a single overload

The experimental data for the bi-axial overloading example is taken from the same work by Datta et al. [52] from which also one of the constant amplitude in-phase loading experimental curves discussed before originated. Therefore, the adjusted Paris constant should also be valid for the overload case. The loading ratio is equal to 0.1 and the maximum applied load is equal to 15 kN, which is the same as in the constant amplitude case. The overload is introduced at a crack length of 3.9 mm and has an amplitude of 1.75 times the maximum applied load.

The comparison between experiment and the numerical model is given in Fig. 15. It can be seen that both the crack growth rate and the amount of cycles show good agreement. It is emphasized that accurately capturing the constant amplitude part as well as the retardation did not require recalibration of the strength parameter as determined for the thicker compact tension specimen.

7. Conclusions

This study discussed in detail the calibration and validation of a cohesive XFEM model for fatigue crack growth simulations in ductile materials based on the authors' earlier work [28]. It is shown that the cohesive stiffness does not influence the energy release rate for a given crack length. Furthermore, the fatigue behaviour is independent of the critical energy release rate. Contrary to most other cohesive zone models described in literature, this study provides a consistent procedure to calibrate all parameters involved. In total three parameters required calibration: the Paris constant, the Paris exponent and the tensile strength. Increasing the tensile strength results in a lower energy release rate for a given crack length. For every value of the tensile strength, the plastic Paris parameters can be calibrated to a constant amplitude cyclic loading test. After that, the correct set of tensile strength and Paris parameters is chosen such that it can correctly capture crack retardation in an overload experiment.

The calibrated parameters are subsequently used for in-phase and out-of-phase bi-axial loading problems on a cruciform specimen made of a ductile material, from which the experimental data originate from a different source in literature. In terms of crack path, in which the Paris parameters do not play a role, there was a good agreement with experiment for in-phase loading and 90° out-of-phase loading. However, the numerical model showed a deviation from the crack path in the experiment for 45° out-of-phase loading. Recalibrating the Paris constant, such that the numerical model agreed with the experiment for in-phase biaxial loading, resulted in a good agreement for 90° out-of-phase biaxial loading and biaxial loading with a single overload for experiments on the same geometry. It was not necessary to calibrate the strength parameter to accurately reproduce the retardation observed in the experiment.

The importance of including plasticity for fatigue crack growth was illustrated with numerical results obtained with the same cohesive zone model but then embedded in a linear elastic bulk material. With the elastic bulk material, no crack retardation after overloading is obtained. Moreover, parameters resulting in a good agreement with the experiment for in-phase biaxial loading do not result in a good agreement in out-of-phase biaxial loading or overloading. It is concluded that including elastic-plastic material behaviour is essential when numerically investigating fatigue crack growth under load conditions that deviate from most simple constant amplitude mode I cases.

Acknowledgments

This research is part of the EUROS program, which is supported by NWO domain Applied and Engineering Sciences and partly funded by the Dutch Ministry of Economic Affairs.

References

- [1] W. Elber, *Fatigue crack closure under cyclic tension*, Engineering Fracture Mechanics **2**, 37 (1970).
- [2] W. Elber, *The significance of fatigue crack closure*, in *Damage tolerance in aircraft structures* (ASTM International, 1971).
- [3] T. Zhao, J. Zhang, and Y. Jiang, *A study of fatigue crack growth of 7075-T651 aluminum alloy*, International Journal of Fatigue **30**, 1169 (2008).
- [4] J. Qian and A. Fatemi, *Mixed mode fatigue crack growth: A literature survey*, Engineering Fracture Mechanics **55**, 969 (1996).
- [5] R. Neerukatti, S. Datta, A. Chattopadhyay, N. Iyyer, and N. Phan, *Fatigue crack propagation under in-phase and out-of-phase biaxial loading*, Fatigue & Fracture of Engineering Materials & Structures **41**, 387 (2017).
- [6] B. Yang, S. Mall, and K. Ravi-Chandar, *A cohesive zone model for fatigue crack growth in quasibrittle materials*, International Journal of Solids and Structures **38**, 3927 (2001).
- [7] O. Nguyen, E. Repetto, M. Ortiz, and R. Radovitzky, *A cohesive model of fatigue crack growth*, International Journal of Fracture **110**, 351 (2001).
- [8] K. Roe and T. Siegmund, *An irreversible cohesive zone model for interface fatigue crack growth simulation*, Engineering Fracture Mechanics **70**, 209 (2003).
- [9] A. Ural, V. R. Krishnan, and K. D. Papoulia, *A cohesive zone model for fatigue crack growth allowing for crack retardation*, International Journal of Solids and Structures **46**, 2453 (2009).
- [10] H. Jiang, X. Gao, and T. Srivatsan, *Predicting the influence of overload and loading mode on fatigue crack growth: A numerical approach using irreversible cohesive elements*, Finite Elements in Analysis and Design **45**, 675 (2009).
- [11] S. Silitonga, J. Maljaars, F. Soetens, and H. Snijder, *Numerical simulation of fatigue crack growth rate and crack retardation due to an overload using a cohesive zone model*, in *11th International Fatigue Congress*, Advanced Materials Research, Vol. 891 (Trans Tech Publications, 2014) pp. 777–783.
- [12] T. Belytschko and T. Black, *Elastic crack growth in finite elements with minimal remeshing*, International Journal for Numerical Methods in Engineering **45**, 601 (1999).
- [13] N. Moës, J. Dolbow, and T. Belytschko, *A finite element method for crack growth without remeshing*, International Journal for Numerical Methods in Engineering **46**, 131 (1999).

- [14] I. Singh, B. Mishra, S. Bhattacharya, and R. Patil, *The numerical simulation of fatigue crack growth using extended finite element method*, International Journal of Fatigue **36**, 109 (2012).
- [15] H. Pathak, A. Singh, and I. Singh, *Fatigue crack growth simulations of 3-D problems using XFEM*, International Journal of Mechanical Sciences **76**, 112 (2013).
- [16] M. Kumar, S. Ahmad, I. Singh, A. Rao, J. Kumar, and V. Kumar, *Experimental and numerical studies to estimate fatigue crack growth behavior of Ni-based super alloy*, Theoretical and Applied Fracture Mechanics **96**, 604 (2018).
- [17] M. Kumar, I. Singh, and B. Mishra, *Fatigue crack growth simulations of plastically graded materials using XFEM and J-integral decomposition approach*, Engineering Fracture Mechanics **216**, 106470 (2019).
- [18] R. Plank and G. Kuhn, *Fatigue crack propagation under non-proportional mixed mode loading*, Engineering Fracture Mechanics **62**, 203 (1999).
- [19] E. Lee and R. Taylor, *Fatigue behavior of aluminum alloys under biaxial loading*, Engineering Fracture Mechanics **78**, 1555 (2011).
- [20] S. Mall and V. Perel, *Crack growth behavior under biaxial fatigue with phase difference*, International Journal of Fatigue **74**, 166 (2015).
- [21] D. Infante-García, G. Qian, H. Miguélez, and E. Giner, *Analysis of the effect of out-of-phase biaxial fatigue loads on crack paths in cruciform specimens using XFEM*, International Journal of Fatigue **123**, 87 (2019).
- [22] L. Voormeeren, F. van der Meer, J. Maljaars, and L. Sluys, *A new method for fatigue life prediction based on the thick level set approach*, Engineering Fracture Mechanics **182**, 449 (2017).
- [23] A. Hansbo and P. Hansbo, *An unfitted finite element method, based on nitsche's method, for elliptic interface problems*, Computer Methods in Applied Mechanics and Engineering **191**, 5537 (2002).
- [24] A. Hansbo and P. Hansbo, *A finite element method for the simulation of strong and weak discontinuities in solid mechanics*, Computer methods in applied mechanics and engineering **193**, 3523 (2004).
- [25] J. Mergheim, E. Kuhl, and P. Steinmann, *A finite element method for the computational modelling of cohesive cracks*, International Journal for Numerical Methods in Engineering **63**, 276 (2005).
- [26] J. Song, P. Areias, and T. Belytschko, *A method for dynamic crack and shear band propagation with phantom nodes*, International Journal for Numerical Methods in Engineering **67**, 868 (2006).
- [27] F. van der Meer and L. Sluys, *A phantom node formulation with mixed mode cohesive law for splitting in laminates*, International Journal of Fracture **158**, 107 (2009).

- [28] R. Dekker, F. van der Meer, J. Maljaars, and L. Sluys, *A cohesive x fem model for simulating fatigue crack growth under mixed-mode loading and overloading*, International Journal for Numerical Methods in Engineering **118**, 561 (2019).
- [29] N. Palle and J. Dantzig, *An adaptive mesh refinement scheme for solidification problems*, Metallurgical and Materials Transactions A **27**, 707 (1996).
- [30] D. Greaves and A. Borthwick, *Hierarchical tree-based finite element mesh generation*, International Journal for Numerical Methods in Engineering **45**, 447 (1999).
- [31] A. Tabarraei and N. Sukumar, *Adaptive computations on conforming quadtree meshes*, Finite Elements in Analysis and Design **41**, 686 (2005), the Sixteenth Annual Robert J. Melosh Competition.
- [32] J. Chaboche, *Constitutive equations for cyclic plasticity and cyclic viscoplasticity*, International Journal of Plasticity **5**, 247 (1989).
- [33] J. Chaboche, *On some modifications of kinematic hardening to improve the description of ratchetting effects*, International Journal of Plasticity **7**, 661 (1991).
- [34] G. Meschke and P. Dumstorff, *Energy-based modeling of cohesive and cohesionless cracks via X-FEM*, Computer Methods in Applied Mechanics and Engineering **196**, 2338 (2007).
- [35] G. Ruiz, A. Pandolfi, and M. Ortiz, *Three-dimensional cohesive modeling of dynamic mixed-mode fracture*, International Journal for Numerical Methods in Engineering **52**, 97 (2001).
- [36] B. Bak, A. Turon, E. Lindgaard, and E. Lund, *A simulation method for high-cycle fatigue-driven delamination using a cohesive zone model*, International Journal for Numerical Methods in Engineering **106**, 163 (2015).
- [37] P. Paris and F. Erdogan, *A critical analysis of crack propagation laws*, Journal of Basic Engineering **85**, 528 (1963).
- [38] F. Erdogan and G. C. Sih, *On the crack extension in plates under plane loading and transverse shear*, Journal of basic engineering **85**, 519 (1963).
- [39] G. Wells and L. Sluys, *A new method for modelling cohesive cracks using finite elements*, International Journal for Numerical Methods in Engineering **50**, 2667 (2001).
- [40] P. Harper and S. Hallett, *A fatigue degradation law for cohesive interface elements - development and application to composite materials*, International Journal of Fatigue **32**, 1774 (2010).
- [41] E. Iarve, K. Hoos, M. Braginsky, E. Zhou, and D. Mollenhauer, *Progressive failure simulation in laminated composites under fatigue loading by using discrete damage modeling*, Journal of Composite Materials **51**, 2143 (2017).
- [42] N. Moës and T. Belytschko, *Extended finite element method for cohesive crack growth*, Engineering Fracture Mechanics **69**, 813 (2002).

-
- [43] A. Gravouil, N. Moës, and T. Belytschko, *Non-planar 3D crack growth by the extended finite element and level sets - part II: Level set update*, International Journal for Numerical Methods in Engineering **53**, 2569 (2002).
- [44] M. Naderi, S. Hoseini, and M. Khonsari, *Probabilistic simulation of fatigue damage and life scatter of metallic components*, International Journal of Plasticity **43**, 101 (2013).
- [45] J. Davis, ed., *Metals handbook* (ASM International, 1998).
- [46] R. E. Zinkham, *Anisotropy and thickness effects in fracture of 7075-T6 and -T651 aluminium alloy*, Engineering Fracture Mechanics **1**, 275 (1968).
- [47] D. DuQuesnay, P. Underhill, and H. Britt, *Fatigue crack growth from corrosion damage in 7075-T6511 aluminium alloy under aircraft loading*, International Journal of Fatigue **25**, 371 (2003).
- [48] T. Anderson, *Fracture mechanics: Fundamentals and applications* (Taylor and Francis, 2005).
- [49] K. Sadananda, A. Vasudevan, R. Holtz, and E. Lee, *Analysis of overload effects and related phenomena*, International Journal of Fatigue **21**, S233 (1999).
- [50] D. Agius, C. Wallbrink, W. Hu, M. Kajtaz, C. H. Wang, and K. I. Kourousis, *On the utilisation of nonlinear plasticity models in military aircraft fatigue estimation: A preliminary comparison*, Aerospace Science and Technology **71**, 25 (2017).
- [51] D. Agius, M. Kajtaz, K. Kourousis, C. Wallbrink, C. Wang, W. Hu, and J. Silva, *Sensitivity and optimisation of the chaboche plasticity model parameters in strain-life fatigue predictions*, Materials & Design **118**, 107 (2017).
- [52] S. Datta, A. Chattopadhyay, N. Iyyer, and N. Phan, *Fatigue crack propagation under biaxial fatigue loading with single overloads*, International Journal of Fatigue **109**, 103 (2018).

4

A level set model for stress-dependent corrosion pit propagation

R. Dekker^a , F.P. van der Meer^a, J. Maljaars^{b,c}, L.J. Sluys^a

^a Faculty of Civil Engineering and Geosciences, Delft University of Technology, Delft, The Netherlands

^b Faculty of Built Environment, Eindhoven University of Technology, Eindhoven, The Netherlands

^c Structural reliability, TNO ,Delft, The Netherlands

ABSTRACT

A numerical model for corrosion pit propagation under mechanical loading is presented. The level set method is used for corrosion front tracking and also enables the domain to be split into a solid and a pit domain. In the pit the diffusion of atoms originating from the dissolution process occurring at the pit front is simulated. The model is capable of automatically capturing lacy cover formation due to the inclusion of activation control, diffusion control and passivation. In the solid static equilibrium is solved to obtain strains and stresses. A parameter, dependent on the signs of the plastic strain increment and the back stress, is introduced to define the influence of plasticity on the corrosion rate. The model is used to study pit growth under electrochemical and mechanical loading. Under activation control combined with an elastic material response, pits propagate faster under constant loading than under cyclic loading. When plastic deformation occurs, cyclic loading can significantly increase the pit growth rate. Increasing the cyclic load frequency results in faster propagation due to kinematic hardening. Under diffusion control, mechanical loading does not influence the pit growth rate, given that the salt layer leading to diffusion control remains intact.

1. Introduction

Numerous metal structures are exposed to corrosion while simultaneously being subjected to mechanical loading. For example, offshore wind turbine parks are becoming increasingly popular as a means of energy production without using valuable space on land. The disadvantage is that the foundations of these structures, i.e. the mono-pile or jacket structure, are exposed to a more corrosive environment compared to onshore wind turbines. Unfortunately, the effect of corrosion on the service lifetime is still relatively unknown, especially in the case of corrosion in combination with mechanical loading. Novel computer models that can simulate the combination of electrochemical and mechanical loading in metals could reduce this uncertainty, leading to more accurate lifetime predictions.

There are in general two major types of metal corrosion [1] in open-air. The first type is uniform corrosion in which there is a uniform loss in thickness over the surface exposed to the corrosive environment. The second type is local corrosion, which can occur in the form of pitting. Pitting corrosion is most common among stainless steels and aluminium alloys [2], but can also be found in non-stainless steels, for example in pipelines [3] and offshore structures [4]. Pitting corrosion has generally a significantly larger impact on the lifetime of a structure than uniform corrosion. Pits may grow rather quickly and create stress concentration sites from which mechanically assisted cracks can initiate. To make things worse, the speed of corrosion increases in the presence of mechanical stress [5]. An additional challenge is posed by the fact that it is not always straightforward to define the size of a pit, because a perforated cover, known as a lacy cover, might hide the true pit size [6]. Pitting corrosion can be defined by three different stages, namely, breakdown of the passive layer, metastable pit growth and stable pit growth, where reaching stage three, stable pit growth, is most disastrous regarding structural failure [2]. This study focusses on the computational modelling of the stable pit growth stage.

Different methods can be found in literature to model stable corrosion pit propagation. These are finite volume models [7, 8], models that use the finite element method combined with adaptive meshing [9–11], models using the eXtended Finite Element Method (XFEM) combined with the level set method [12–14], phase field models [15–18], peridynamic models [19] and cellular automata (CA) models [20, 21]. Only two of these models considered lacy cover formation [9, 19]. Furthermore, inclusion of the effect of a constant stress on the pit growth rate are included in a phase field model [18, 22] for an elastic material and an elastic-plastic material [16], and in a CA model [20] for an elastic-plastic material. Fatoba et al. [21] developed a CA model for corrosion that includes the effect of cyclic loading by using a cyclic stress-strain curve constructed from stabilized hysteresis loops. For both CA models, the effect of plastic strain on the corrosion process is taken into account by employing the Gutman equation [23] using the effective plastic strain as a variable to quantify the influence of plasticity on corrosion. However, a more general unified framework that can deal with pit growth under both constant and cyclic loading for an elastic-plastic material has not been found by the authors.

In this study the level set method [24] is used in combination with the finite element method in order to simulate corrosion pit propagation. It avoids the need of re-meshing

which was required in other methods [9–11]. Furthermore, the level set method enables the domain to be easily split into a pit domain and a solid domain. In each domain a different set of equations is solved. In this study it is shown that it is not required to use the full XFEM as was done in other studies that used the level set method [12, 13]. Instead, a simple modification in integration scheme suffices, keeping the number of degrees of freedom (DOFs) per node constant, which is more in line with the phantom node version of XFEM [25–27]. This approach ensures that the two domains can be considered separately and therefore, for example, no unnecessary diffusion equations are solved in the solid domain. Furthermore, the influence of stress and strain on the pit growth velocity is included, where an isotropic and kinematic hardening plasticity model is employed such that the effect of cyclic plastic strain on the pit growth rate can be captured. For this a separate plasticity parameter is introduced that does not grow indefinitely in a stabilized cyclic response, which is another novel contribution in this paper.

The paper starts by presenting the description of the multi-physics problem to be solved, followed by the treatment of the mechanical behaviour of the metal. Next, the corrosion behaviour is discussed, in which activation controlled corrosion, diffusion controlled corrosion and passivation are addressed. Also, the new state variable to indicate the state of plasticity is discussed. After that, the numerical framework is outlined with a description of the solution procedure. Finally, four numerical examples are given: a diffusion controlled pencil test, a study on the influence of the initial pit shape, a lacy cover formation problem and a study on the influence of mechanical loading on pit propagation.

2. Problem description

4

A corrosion pit as visualized in Fig. 1 is considered. The problem consists of two domains with a moving boundary, namely the pit and the solid. The pit domain consists of an electrolyte which has the ability to transfer electrons. The pit front moves into the solid due to anodic dissolution, which means that a metal atom, indicated with M , leaves the solid and enters the pit solution while disposing itself of electrons. At the same time a cathodic reaction occurs that consumes these electrons in which for example hydrogen anions are converted into hydrogen gas. In this study it is assumed that the cathodic reaction does not limit the rate of corrosion and thus only the anodic reaction is considered. Furthermore, a mechanical load is applied on the solid, resulting in stresses and strains, which can influence the pit growth rate.

The solid domain is the part in which the applied load is transferred. Here, static equilibrium should hold, which in the absence of any body forces, can be written as:

$$\nabla \cdot \sigma = 0 \quad (4.1)$$

where σ is the mechanical stress and ∇ the differential operator.

In the pit domain there is a diffusion of metal atoms that originate from the solid. The concentration of metal atoms is therefore largest near the pit front and smallest near the pit boundary, which is the outside environment (Fig. 1). The diffusion equation, in the

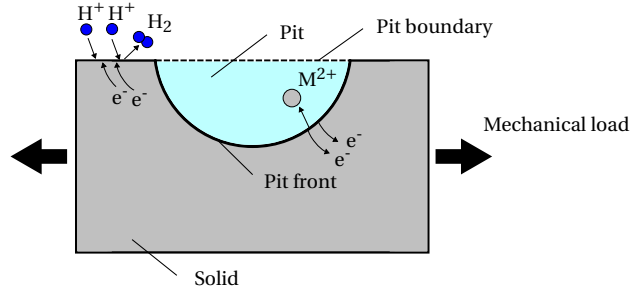


Figure 1: Schematic picture of the pit domain, the solid domain and the pit front representing the corrosion process of a metal M and the applied mechanical loading (arrows).

absence of any source, is defined as follows:

$$\frac{\partial c}{\partial t}(\mathbf{x}, t) + \nabla \cdot \mathbf{J}(\mathbf{x}, t) = 0 \quad (4.2)$$

in which c is the concentration of atoms/ions, \mathbf{J} is the flux of atoms, \mathbf{x} is the location in the domain and t is time. In this study, only the concentration of atoms of the metal itself is considered, however, inclusion of other species is possible as well [11, 28–30].

The pit front is not fixed in space, but propagates through the domain. The equilibrium between the flux of dissolved metal atoms and the velocity of the moving pit front is given by the Rankine-Hugoniot condition [7, 31]:

$$\{\mathbf{J}(\mathbf{x}, t) + [c_{\text{solid}} - c(\mathbf{x}, t)]\mathbf{V}(\mathbf{x}, t)\} \cdot \mathbf{n}(\mathbf{x}, t) = 0 \quad (4.3)$$

Here, \mathbf{V} is the front velocity, \mathbf{n} is the unit normal vector that is perpendicular to the front and c_{solid} is the concentration of atoms in the solid.

3. Mechanical behaviour

The mechanical load can be applied with a constant magnitude or in a cyclic fashion. Therefore, a plasticity model that includes both isotropic and kinematic hardening is used to capture plastic flow under cyclic loading. The elastic behaviour simply follows from Hooke's law with Young's modulus E and Poisson ratio ν .

The Von Mises criterion is used to describe the yield surface:

$$f_{\text{vm}} = \sqrt{\frac{2}{3}(\mathbf{s} - \boldsymbol{\beta}) : (\mathbf{s} - \boldsymbol{\beta})} - \sigma_y \quad (4.4)$$

where \mathbf{s} and $\boldsymbol{\beta}$ are the deviatoric stresses and deviatoric back stresses, respectively. The yield stress σ_y is defined with a non-linear isotropic hardening rule [32]:

$$\sigma_y = \sigma_0 + Q_\infty \left(1 - e^{-b\bar{\epsilon}_p}\right) \quad (4.5)$$

where σ_0 is the initial yield stress, Q_∞ the limit value for the yield stress increase and b is a measure for the rate of change of the yield surface. The increment in equivalent plastic strain $d\bar{\epsilon}_p$ is given as:

$$d\bar{\epsilon}_p = \sqrt{\frac{2}{3}} d\epsilon_p : d\epsilon_p \quad (4.6)$$

where $d\epsilon_p$ is the plastic strain increment. The kinematic hardening rule is given by [33]:

$$d\beta = \frac{2}{3} C d\epsilon_p - \gamma \beta d\bar{\epsilon}_p \quad (4.7)$$

where C is the linear and γ is the non-linear kinematic hardening coefficient.

4. Corrosion behaviour

A distinction between three different regimes can be made when looking at stable pitting corrosion. First, there is activation controlled corrosion in which the corrosion speed is given and serves as a boundary condition for the diffusion problem. The second regime occurs when a certain saturation concentration c_{sat} is reached on the inside of the pit front at which point a salt layer forms on the front. The speed of the corrosion process then depends on the speed with which the metal atoms diffuse away from the front surface and it is therefore called diffusion controlled corrosion. The third option is simply passivation, which means that the corrosion process has come to a halt. The three regimes, and how they use Eq. (4.3), are discussed next.

4

4.1. Activation control

In activation control the rate with which the pit grows depends on the rate of the corrosion reaction, which is defined by the anodic current density i_a . The Butler-Volmer equation or the Tafel equation can be used to compute the current density as function of the applied potential [7, 8, 12]. However, in this study the anodic current density is used as an input instead of the applied potential. It is assumed that the current density acts perpendicular to the front, which means that the following equation holds:

$$\mathbf{i}_a(\mathbf{x}, t) = \mathbf{n}(\mathbf{x}, t) i_a \quad (4.8)$$

The electric current at a dissolving electrode is proportional to the mass being dissolved per time instant as stated by Faraday's law:

$$\mathbf{i}_a(\mathbf{x}, t) = \mathbf{V}(\mathbf{x}, t) c_{\text{solid}} z F \quad (4.9)$$

where F is Faraday's number and z the number of electrons involved. For a given i_a this equation can be rewritten to obtain an expression for the front velocity:

$$\mathbf{V}(\mathbf{x}, t) = \frac{i_a \mathbf{n}(\mathbf{x}, t)}{c_{\text{solid}} z F} \quad (4.10)$$

It is assumed that movement of dissolved ions is diffusion dominated [34], which means that the flux is represented by Fick's law:

$$\mathbf{J}(\mathbf{x}, t) = -D\nabla c(\mathbf{x}, t) \quad (4.11)$$

where D is the diffusion coefficient of the metal in the electrolyte. Substituting Eq. (4.11) into Eq. (4.3) gives

$$\{-D\nabla c(\mathbf{x}, t) + [c_{\text{solid}} - c(\mathbf{x}, t)]\mathbf{V}(\mathbf{x}, t)\} \cdot \mathbf{n}(\mathbf{x}, t) = 0 \quad (4.12)$$

where the velocity \mathbf{V} is given by Eq. (4.10). Thus, in the case of activation control, the front condition acts as a mixed or Robin boundary condition which depends on a front velocity that is known *a priori*.

4.1.1. Mechanical stress-dependent corrosion rate

According to Gutman [23], the anodic current density of a pure metal is influenced by the amount of plastic strain \bar{p} and hydrostatic stress σ_H through the following relation:

$$i_a \rightarrow i_a \left(\frac{\bar{p}}{\epsilon_0} + 1 \right) \exp \left(\frac{|\sigma_H| V_m}{RT} \right) \quad (4.13)$$

where ϵ_0 is the initial yield strain, V_m is the molar volume of the solid metal, R is the universal gas constant and T the temperature. According to this equation, an increase in the amount of plasticity or an increase in the absolute value of the hydrostatic stress results in a faster corrosion rate. When considering a 1D dimensional case, \bar{p} is simply equal to the plastic strain. In a multi-dimensional case, under a constant or an increasing applied stress, the equivalent plastic strain $\bar{\epsilon}_p$ could substitute \bar{p} as in [20].

However, there is a problem in using $\bar{\epsilon}_p$ as indicator for the amount of plastic strain in the case of cyclic loading. According to Gutman, an increase in dislocation density and in dislocation pile up, accelerates the corrosion rate. Due to the combination of Eq. (4.6), which states that the equivalent plastic strain cannot decrease in value, and the presence of kinematic hardening, the equivalent plastic strain will keep on increasing whenever there is a plastic strain increment. This means that $\bar{\epsilon}_p$ increases in value even when the global cyclic response has stabilized. In reality, kinematic hardening under cyclic loading represents dislocations moving back and forth [35], meaning that the largest pile up can decrease when reversed loading starts. Therefore under cyclic loading, $\bar{\epsilon}_p$ from Eq. (4.6) is not a correct measure for dislocation pile up. Note that a previous numerical study on corrosion pit growth that only considered cyclic loading did not encounter this problem because stabilized plasticity relations were used [21], although the physical meaning of $\bar{\epsilon}_p$ in such equations is debatable.

To ensure the presented plasticity relations can still be used, a new parameter, defined as the equivalent dislocation strain $\bar{\epsilon}_d$, is introduced:

$$d\bar{\epsilon}_d = \int_0^{d\bar{\epsilon}_p} \text{sgn}(d\epsilon_p \cdot \beta) dx \quad (4.14)$$

The parameter $\bar{\epsilon}_d$ can, unlike $\bar{\epsilon}_p$, increase or decrease in magnitude. It decreases in value when the plastic strain increment acts in the opposite direction of the back stress, which could occur under cyclic loading. In the case of a monotonically increasing stress, $\bar{\epsilon}_d$ is equal to $\bar{\epsilon}_p$. It should be emphasized that the mechanical behaviour is still determined by using $\bar{\epsilon}_p$, and is therefore not affected by $\bar{\epsilon}_d$. The parameter $\bar{\epsilon}_d$ is only used in Eq. (4.13) as a substitute of \bar{p} in order to compute the increase in the anodic current density.

Figure 2 shows the evolution of $\bar{\epsilon}_d$ and $\bar{\epsilon}_p$ under monotonic and cyclic loading. For cyclic load the maximum value of both parameters for each loading cycle is plotted against the number of loading cycles. Under monotonic load the two plasticity measures remain exactly equal. However, there is a significant difference between the two when considering cyclic loading. $\bar{\epsilon}_p/\epsilon_0$ reaches values of over 300, while $\bar{\epsilon}_d/\epsilon_0$ reaches values of around 35 and remains relatively constant after 50 cycles, which is the desired characteristic behaviour for \bar{p} in Eq. (4.13) when the cyclic response stabilizes.

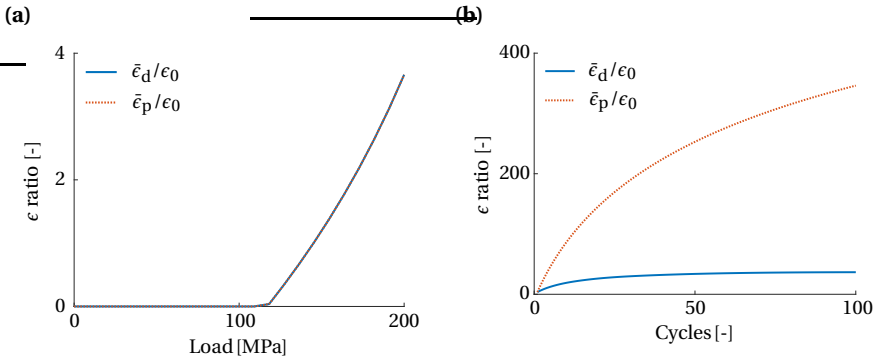


Figure 2: Development of $\bar{\epsilon}_d$ and $\bar{\epsilon}_p$ for a single element test under (a) a monotonic applied load, and (b) under cyclic loading with a maximum applied stress of 200 MPa and a load ratio of -1 . The material parameters can be found in Table 1.

4.2. Diffusion control

Diffusion control occurs once the saturation concentration c_{sat} is reached on the inside of the pit front, which leads to the formation of a salt layer. Due to this salt layer, the concentration on the inside of the pit front remains constant at c_{sat} . Therefore, this concentration is applied as a Dirichlet or essential boundary condition on the inside of the front, which means that it has been assumed that the salt layer has zero thickness. Consequently, Eq. (4.3) is no longer applied as a boundary condition, but is used to determine the front velocity once the concentration distribution has been computed:

$$\mathbf{V}(\mathbf{x}, t) = \frac{D\nabla c \cdot \mathbf{n}(\mathbf{x}, t)}{c_{\text{solid}} - c_{\text{sat}}} \quad (4.15)$$

Note that in this case the front velocity is no longer dependent on i_a and thus plastic strain and hydrostatic stress do not influence the front velocity.

4.3. Passivation

In this study, a simple passivation model has been used in which the corrosion process comes to a halt once the front concentration in the pit is smaller or equal to a passivation concentration c_{pas} [6]. In this case the front velocity is zero and Eq. (4.3) reduces to:

$$\mathbf{J}(\mathbf{x}, t) = \mathbf{0} \quad (4.16)$$

5. Numerical framework

The mechanically assisted pitting corrosion process is simulated by combining the finite element method with the level set method, which is visualized in Fig. 3. In the level set method a front is tracked implicitly by assigning every node a signed distance value ϕ , of which the magnitude is equal to the shortest distance between the node and the front. A positive value indicates that the node is present in the solid, while if the value is negative or equal to zero the node is located in the pit.

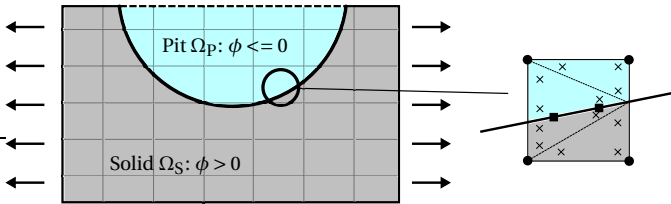


Figure 3: A corrosion pit under mechanical stress in a finite element and level set method numerical framework. Elements cut by the front are both present in the solid and the pit, but use different integration schemes depending on the domain.

The solid domain Ω_S and the pit domain Ω_P are constructed by taking elements located on respective sides of the front. However, some elements are cut by the front and are thus present in both the pit and the solid domain. This is solved by only integrating the area that is on the outside of the front ($\phi > 0$) for the solid domain and inside the front for the pit domain. The specific integration areas are created by triangular partitioning as shown in Fig. 3. The elements through which a section of the front is present, are called the front elements. The nodes of these front elements are defined as the front nodes. Furthermore, having the location of the front by means of the signed distance value, line elements can be introduced in the elements that are crossed by the front. These line elements are assigned front integration points, indicated with solid squares in Fig. 3, at which the regime of corrosion, the local front velocity, the stresses and the strains are determined.

The solution is computed by means of a staggered approach in which there is a total of seven different steps. The order of the steps are indicated in the flow diagram in Fig. 4. For corrosion without an applied mechanical stress, the mechanical problem step is simply skipped.

When considering cyclic mechanical loading, the solution procedure does not involve

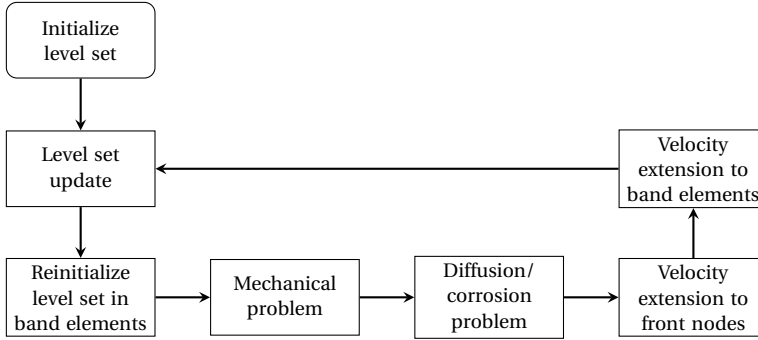


Figure 4: Flow diagram of the mechanically assisted pitting corrosion model

any additional step in the flow diagram. However, the time increment is now coupled to the load cycle frequency and thus the mechanical load increment. For example, the fatigue cycle period is 10 s for a fatigue cycle frequency of 0.1 Hz. When using 10 load steps per cycle for this given frequency, it means that the time increment per load step should be equal to 1 second. In the remainder of this section, the different parts of the numerical framework are discussed in more detail.

5.1. Level set update

It is required that the velocity at the nodes is known in order to update the level set. For the very first level set update, the velocity is simply zero. The level set is updated explicitly by means of the following equation:

$$\phi^{t+\Delta t} = \phi^t - V_n \Delta t \quad (4.17)$$

The time increment is defined by the Courant-Friedrichs-Lewy (CFL) condition to ensure stability of the solution [36]. In the case of cyclic loading, the time increment per load step should be lower than the CFL condition. If this is not the case, the number of load steps per cycle simply has to be increased.

At each level set update, the front moves outward. This means that after every update the old front lines are removed and new ones are introduced. Where necessary, concentration degrees of freedom are added on the nodes and displacement degrees of freedom removed. In addition, the integration areas created by triangulation are updated.

5.2. Level set reinitialization

Reinitialization of the level set is performed to ensure that the signed distance property remains satisfied at every node. This property is defined by the following relation, which is known as the Eikonal equation:

$$|\nabla \phi| - 1 = 0 \quad (4.18)$$

In this study, two different methods for reinitialization were considered. The first one uses the fast marching method [36] which is a time efficient algorithm. However, this method, without the use of a shadow or dual mesh, can only be employed for either a structured mesh or a mesh composed of linear triangular elements as done by van der Meer et al. [37].

The other method for reinitialization follows the procedure by Adams et al. [38], where the least square residual of Eq. (4.18) is minimized, followed by Picard linearisation and then transformed to a weak form. The method of using field equations for reinitialization can be used for any type of mesh. However, solving a system of equations is more expensive than using a fast marching algorithm. Fortunately, the computation time can be significantly reduced by only considering a band of elements around the pit front as is shown in Fig. 5. Additionally, it is generally not necessary to perform the reinitialization of the level set every time the level set is updated, but this can be done every five or ten steps, depending on the complexity of the front shape, to ensure that ϕ remains approximately equal to a signed distance function [36]. In this paper it is assumed that the signed distance values at the nodes belonging to front elements ϕ_{Front} are known and can therefore be used as Dirichlet boundary conditions. This simplifies the weak form significantly:

$$\int_{\Omega_\phi} \nabla \phi^m \cdot \nabla \psi \, d\Omega = \int_{\Omega_\phi} \nabla \psi \cdot \frac{\nabla \phi^{m-1}}{|\nabla \phi^{m-1}|} \, d\Omega \quad \text{with } \phi^m = \phi_{\text{Front}} \text{ on } \Omega_{\text{Front}} \quad (4.19)$$

where ψ is the test function, Ω_ϕ the domain of the band and Ω_{front} the domain of the front elements (Fig. 5). The superscript m indicates the unknown signed distance solution for the current iteration step and the superscript $m-1$ from the previous. Note that the size of the band depends on the reinitialization interval. The reinitialization equation is solved iteratively until the signed distance value is converged. The resulting system of equations has a discretized elemental reinitialization stiffness contribution that is given by:

$$\mathbf{K}_{\text{re}} = \int_{\Omega_\phi} \mathbf{B}^T \mathbf{B} \, d\Omega \quad (4.20)$$

where \mathbf{B} are the gradients of the shape functions \mathbf{N} which are used to discretize the test function and the state variable. The elemental reinitialization external vector contribution is defined as:

$$\mathbf{f}_{\text{re}} = \int_{\Omega_\phi} \mathbf{B}^T \frac{\mathbf{B}^T \phi^{m-1}}{|\mathbf{B}^T \phi^{m-1}|} \, d\Omega \quad (4.21)$$

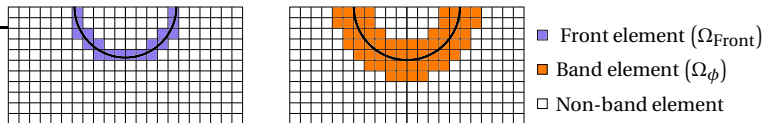


Figure 5: Front and band elements around the pit front

5.3. Mechanical problem

The mechanical problem solves the static equilibrium given in Eq. (4.1), of which the weak form is defined as:

$$\int_{\Omega_S} \sigma : \nabla \psi d\Omega = \int_S \tau \cdot \psi dS \quad (4.22)$$

with prescribed displacements or tractions τ on the domain boundary S_u or S_τ , respectively. This equation is solved only in the solid domain with the nodal displacements as unknowns. Due to the inclusion of plasticity the mechanical problem is solved with the Newton-Raphson method [39–41] which minimizes the difference between the internal force vector $\mathbf{f}_{\text{mech}}^{\text{int}}$ and the external force vector $\mathbf{f}_{\text{mech}}^{\text{ext}}$. The resulting system of equations consists of a discretized elemental stiffness contribution:

$$\mathbf{K}_{\text{Mech}} = \int_{\Omega_S} \mathbf{B}^T \mathbf{D}_{\text{stiff}} \mathbf{B} d\Omega \quad (4.23)$$

where $\mathbf{D}_{\text{stiff}}$ is the consistent tangent stiffness. The discretized elemental external vector contribution is defined as:

$$\mathbf{f}_{\text{Mech}}^{\text{ext}} = \int_{S_\tau} \mathbf{N}^T \tau dS \quad (4.24)$$

and the elemental internal vector contribution is given by:

$$\mathbf{f}_{\text{Mech}}^{\text{int}} = \int_{\Omega_S} \mathbf{B}^T \sigma d\Omega \quad (4.25)$$

4

In order for the corrosion problem to use the mechanical result, σ_H and $\bar{\epsilon}_d$ should be known at the front integration points. The value of these quantities can strongly depend on the mesh size. For example, decreasing the mesh size around a stress concentration site significantly increases the stress as well as the amount of plastic strain. Consequently, the corrosion speed up for a fine mesh is larger than for a coarser mesh. Therefore, a non-local approach is used to compute these quantities in order to avoid a mesh dependency through local plastic behaviour by introducing an extra length-scale [42, 43]. The non-local quantities are computed as the weighted average values from solid bulk integration points using the following weight function:

$$w = \frac{1}{(\pi r_w)^2} \exp\left(-\frac{l_w^2}{2r_w^2}\right) \quad (4.26)$$

where l_w is the distance between the bulk and front integration point, The length scale r_w defines both the search radius around a front integration point and the rate of decay of the weight function, and has generally a value of two to three times the element size.

Note that the bulk integration scheme within a front element changes once the front moves. In order to transfer the history data, the old integration points are first extrapolated to the nodes, followed by interpolation to the new integration points [41].

5.4. Diffusion/corrosion problem

As explained in Section 4, there are three regimes for corrosion, namely, activation control, diffusion control and passivation, where different points along the front can be in different regimes. The regime of corrosion is determined for each time step according to the following scheme:

1. Set all the front integration points to activation control except the ones that were passivated in the previous time step and are thus under passivation control. Include Eq. (4.13) when mechanical loading is considered.
2. Solve for the concentrations in the pit domain given the current configuration of control of each front integration point.
3. Check the front concentration c_{front} for each front integration point.
 - If $c_{\text{front}} \geq c_{\text{sat}}$ switch to diffusion control for the front integration point in consideration.
 - If $c_{\text{front}} \leq c_{\text{pas}}$ switch to passivation for the front integration point in consideration.
4. The final concentration solution is computed if the regime of corrosion is not changed for any of the front integration points in step 3. If not, go back to 2 and repeat the process.

Each corrosion regime results in different boundary conditions, which result in extra stiffness and external load vector terms. In activation control there is a Robin boundary condition, given in Eq. (4.12), which can be rewritten to:

$$-\mathbf{J} \cdot \mathbf{n} = c_{\text{solid}} V_n - c V_n \quad (4.27)$$

in which the following relation has been used:

$$\mathbf{V} = V_n \mathbf{n} \quad (4.28)$$

In diffusion control a Dirichlet boundary condition is applied at the pit front, which in this paper is done by using Nitsche's method for embedded surfaces [44]. In the case of passivation, no special action is required.

The weak form of the diffusion equation given in Eq. (4.2), extended with the Robin and Nitsche boundary conditions, is given by:

$$\begin{aligned} \int_{\Omega_p} \psi \frac{\partial c}{\partial t} d\Omega + \int_{\Omega_p} D \nabla c \cdot \nabla \psi d\Omega + \int_{S_A} c V_n \psi dS - \int_{S_D} D \psi \nabla c \cdot \mathbf{n} dS - \int_{S_D} D (c - c_{\text{sat}}) \nabla \psi \cdot \mathbf{n} dS \\ + \int_{S_D} \psi \alpha_{\text{diff}} (c - c_{\text{sat}}) dS = - \int_{S_J} (\mathbf{J} \cdot \mathbf{n}) \psi dS + \int_{S_A} c_{\text{solid}} V_n \psi dS \end{aligned} \quad (4.29)$$

with prescribed concentrations or prescribed flux as boundary conditions on S_c and S_J , respectively. Furthermore, S_A and S_D indicate the pit front sections with activation and

diffusion control, respectively, and α_{diff} is a stabilization parameter, which should be chosen sufficiently large.

In the case of implicit time integration, the discretized elemental stiffness contribution from domain Ω_p is given by:

$$\mathbf{K}_{\text{Diff}} = \frac{1}{\Delta t} \int_{\Omega_p} \mathbf{N}^T \mathbf{N} d\Omega + \int_{\Omega_p} \mathbf{B}^T D \mathbf{B} d\Omega \quad (4.30)$$

and the discretized element external vector contribution by:

$$\mathbf{f}_{\text{Diff}} = \frac{1}{\Delta t} \int_{\Omega_p} (\mathbf{N}^T \mathbf{N}) \mathbf{c}^{t-\Delta t} d\Omega - \int_{S_f} \mathbf{N}^T \mathbf{n}^T \mathbf{J} dS \quad (4.31)$$

where $\mathbf{c}^{t-\Delta t}$ is the concentration in the previous time step. The discretized Robin boundary elemental stiffness contribution is given by:

$$\mathbf{K}_{\text{Diff}}^{\text{Robin}} = \int_{S_A} \mathbf{N}^T \mathbf{N} V_n dS \quad (4.32)$$

and the Robin boundary external vector contribution is defined as:

$$\mathbf{f}_{\text{Diff}}^{\text{Robin}} = \int_{S_A} \mathbf{N}^T c_{\text{solid}} V_n dS \quad (4.33)$$

The discretized stiffness and external load vector contributions due to the Nitsche boundary are given by:

$$\mathbf{K}_{\text{Diff}}^{\text{Flux}} = - \int_{S_D} D \mathbf{N}^T \mathbf{n}^T \mathbf{B} + D \mathbf{B}^T \mathbf{n} \mathbf{N} dS \quad (4.34)$$

$$\mathbf{K}_{\text{Diff}}^{\text{Stab}} = \int_{S_D} \mathbf{N}^T \alpha_{\text{diff}} \mathbf{N} dS \quad (4.35)$$

$$\mathbf{f}_{\text{Diff}}^{\text{Flux}} = - \int_{S_D} D \mathbf{B}^T \mathbf{n} c_{\text{sat}} dS \quad (4.36)$$

$$\mathbf{f}_{\text{Diff}}^{\text{Stab}} = \int_{S_D} \alpha_{\text{diff}} \mathbf{N}^T c_{\text{sat}} dS \quad (4.37)$$

5.5. Velocity extension

For the velocity extension from the front to the nodes, the following equation should hold throughout the domain:

$$\nabla V_n \cdot \nabla \phi = 0 \quad (4.38)$$

As indicated in the flow diagram in Fig. 4, the velocity extension is done in two steps. First, the velocity from the front is extended to the front nodes, followed by the velocity extension from the front nodes to the rest of the band domain. The reason for this is that there is a degree of non-uniqueness in the extension from the front to the front nodes,

which is minimized with applying the appropriate boundary conditions. Therefore, before applying the extension to the rest of the domain, the velocity in the front nodes are checked to ensure that the velocity value lies within the velocity range of the adjacent front segments. If this is not the case, it is assigned the maximum or minimum front velocity of the adjacent segments.

For the velocity extension from the corrosion front to the front nodes, the penalty method is used to enforce the boundary conditions on the front. The weak form of Eq. (4.38) in combination with the penalty method becomes:

$$\int_{\Omega_{\text{int}}} (\nabla V_n \nabla \phi) (\nabla \psi \nabla \phi) d\Omega + \int_S \psi \alpha_{\text{vel}} (V_n - V_{\text{front}}) dS = 0 \quad (4.39)$$

where α_{vel} is the penalty parameter, which should be chosen sufficiently large, and V_{front} is the front velocity which can differ in value for each front integration point. Note that at this stage ϕ is a known quantity.

The discretized elemental contribution to the stiffness matrix and the external force vector belonging to velocity extension with the penalty method are given by:

$$\mathbf{K}_{\text{Vel}} = \int_{\Omega_{\text{int}}} \mathbf{B}^T \nabla \phi (\nabla \phi)^T \mathbf{B} d\Omega \quad (4.40)$$

$$\mathbf{K}_{\text{Vel}}^{\text{Pen}} = \int_S \mathbf{N}^T \alpha_{\text{vel}} \mathbf{N} dS \quad (4.41)$$

$$\mathbf{f}_{\text{Vel}}^{\text{Pen}} = \int_S \alpha_{\text{vel}} \mathbf{N}^T V_{\text{front}} dS \quad (4.42)$$

Due to the ability to have passivation, diffusion control and activation control at the same time at different front integration points, velocity jumps along the front may occur. The front velocity is therefore smeared out by adding a diffusive term to the velocity extension stiffness matrix to improve robustness [45]:

$$\mathbf{K}_{\text{vel}}^{\text{Smeared}} = \int_S \kappa h^2 \mathbf{B}^T \mathbf{s} \mathbf{s}^T \mathbf{B} dS \quad (4.43)$$

where \mathbf{s} is a unit vector perpendicular to \mathbf{n} , κ is the front stabilization parameter and h is the size of a typical element.

The same field equation is solved once more, but now on the band domain Ω_ϕ instead of just Ω_{int} and with the nodal velocities in Ω_{int} as Dirichlet boundary condition.

6. Numerical examples

Four different numerical examples are considered. First, a basic 1D pencil test is compared with an analytical model. Second, two different initial notches are investigated for different current densities in a 2D problem. Third, lacy cover formation is modelled for a 2D pit. All these cases do not involve an applied mechanical load. The fourth example

shows the behaviour of the numerical model when considering pit growth under various electrochemical and mechanical loading combinations. In all examples, the solid material is a 304L stainless steel, which has been chosen because of the available experimental data in literature. Although this material is not used in offshore wind turbines, the principles explained in this paper are not material dependent, only the material parameters itself. The model input parameters used throughout all of these examples are given in Table 1, where the values of c_{sat} and D belong to a temperature of 288.15 K. The mechanical material parameters are taken from Antunes et al. [46].

Table 1: Model parameters

c_{sol} [47]		c_{sat} [9]		D [9]	T	
$143 \times 10^{-6} \text{ mol/mm}^3$		$4.22 \times 10^{-6} \text{ mol/mm}^3$		$0.575 \times 10^{-3} \text{ mm}^2/\text{s}$	288.15 K	
R		F		z [6]	V_m [6]	E
$8.314 \text{ J K}^{-1} \text{ mol}^{-1}$		$96485.3 \text{ C mol}^{-1}$		2.19	$7049.24 \text{ mm}^3/\text{mol}$	200 GPa
ν	σ_0	ϵ_0	Q_∞	b	C	γ
0.29	117 MPa	0.585×10^{-3}	87 MPa	9	52.8 GPa	300

6.1. 1D pencil test

The specimen geometry and the boundary conditions used for the pencil are shown in Fig. 6a. Geometry and boundary conditions are formulated such that this is a 1D problem, but to test the present framework, it is modelled in 2D here. In this example, it is assumed that the pit front is moving solely under diffusion control, and therefore no value of i_A is required. A comparison in pit growth velocity between the numerical model and an analytical relation [7] is given in Fig. 6b. It shows that the model prediction and the analytical relation are equal. The mesh size was set to $2 \mu\text{m}$.

6.2. Initial pit shape

A benefit of the level set method is that it can deal with sharp fronts, as well as merging and branching without any special treatment. To illustrate this, two different initial pit shapes are considered: a sharp notch and a double circular pit. The pit boundary nodes along the free surface are assigned a concentration of zero as a Dirichlet boundary condition. Furthermore, the propagation of both initial shapes is studied for a current density of 1 mA/mm^2 as well as 10 mA/mm^2 in order to show the difference in shape evolution between activation and diffusion control. Note that in these analyses the possibility of

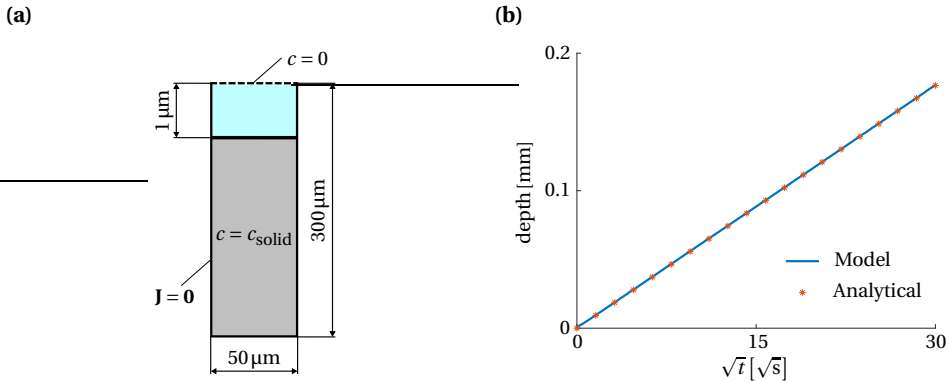


Figure 6: (a) 1D pencil test geometry and boundary conditions and (b) comparison of pit growth velocity between the numerical model and an analytical relation in the case of diffusion controlled corrosion.

passivation has been switched off. When there is both diffusion and activation control present, Eq. (4.43) has been used to avoid a velocity jump at the intersection of the two types of control. The specimen has a height of $200\ \mu\text{m}$ and a width of $400\ \mu\text{m}$. The mesh size was set to $2\ \mu\text{m}$.

Figure 7 shows the initial sharp notch, with a base of $20\ \mu\text{m}$ and a height of $50\ \mu\text{m}$, and its evolution under the two current densities. For the smaller current density, the corrosion process is under pure activation control, which is shown in Fig. 7b. This means the front velocity is constant along the front and thus the notch shape remains relatively constant. For the larger current density, of which the evolution of the shape is given in Fig. 7c, there is a combination of activation and diffusion control. The transition between the two regimes of corrosion is clearly visible through the overhang. Diffusion control is present along the bottom of the pit, at which the concentration is equal to c_{sat} , while the top of the pit, which is in closer contact with the pit boundary, is under activation control. The front velocity for the diffusion control part is largest near the transition point, because of the larger concentration gradients. This velocity is also larger than the activation control velocity, which is the source of the overhang.

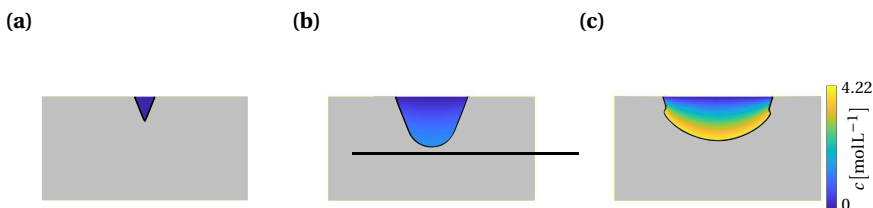


Figure 7: (a) Initial V notch and its shape evolution with atom concentration under (b) pure activation control ($i_a = 1\ \text{mA}/\text{mm}^2$) and (c) a combination of activation and diffusion control ($i_a = 10\ \text{mA}/\text{mm}^2$)

The same type of behaviour can be seen Figure 8, which shows the initial double pit shape, with radii $50\ \mu\text{m}$, and the evolution under the two current densities. For the

smaller current density there is again only activation control, which can be seen from Fig. 8b where c_{sat} is not reached at any point on the pit front. Furthermore, the line of merging is clearly visible because of the sharp tip. For the larger current density, there is again a combination of activation and diffusion control, as shown in Fig. 8c. The overhangs at the transition between the two regimes are not as pronounced as for the sharp notch because of the presence of curvature. The sharp tip at the merging line is smeared out because of diffusion control.

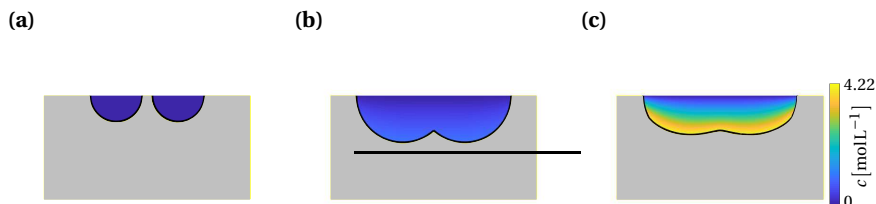


Figure 8: (a) Initial two pits and their shape evolution with atom concentration under (b) pure activation control ($i_a = 1 \text{ mA/mm}^2$) and (c) a combination of activation and diffusion control ($i_a = 10 \text{ mA/mm}^2$).

6.3. Lacy cover formation

The numerical model is compared against experimental data for a corrosion pit with lacy cover [6] in terms of width and depth. A 2D pit is considered with an initial radius R_{init} of $20 \mu\text{m}$ as visualized in Fig. 9a. The initial concentration of metal ions in the pit is equal to the saturation concentration. The pit boundary nodes are assigned a concentration of zero as a Dirichlet boundary condition. Note that these are only the nodes for which $\phi < 0$ holds. The anodic current density is equal to $i_A = 38 \text{ mA/mm}^2$. The specimen has a height of $240 \mu\text{m}$ and a width of $800 \mu\text{m}$. Only half of the domain of the pit is modelled. In order to accurately capture the formation of the lacy cover, the mesh resolution should be sufficiently small to reduce mesh sensitivity. An unstructured mesh was used with an element size of $0.5 \mu\text{m}$ at the top, which is where the cover forms, and $2 \mu\text{m}$ at the bottom of the geometry.

In the numerical model, a lacy cover is automatically formed when including all three different regimes of corrosion into the pit growth computation as is shown in Fig. 9b. The metal atom concentration near the upper part of the pit is lower than the passivation concentration, which means that at these points the front does not propagate. However, at some point deeper into the pit, the passivation criterion is not satisfied any longer. Consequently, the pit front propagates underneath the surface until it reaches the outside environment again and a little island of metal remains. This process is constantly repeated, which is the origin of the lacy cover as observed as a perforated surface layer seen in experiments [6].

In order to obtain a good agreement with the experiment, it was found that c_{pas} should be set equal to 3 mol L^{-1} , which falls within the range of 50 to 80 % of the saturation concentration as mentioned by Laycock and White [10]. A lower value for c_{pas} results

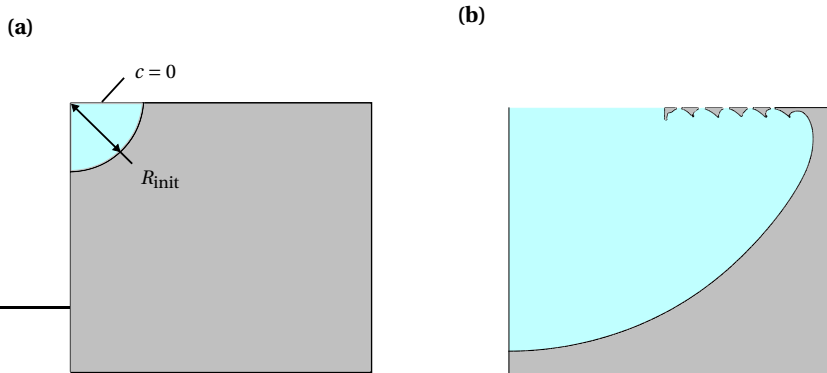


Figure 9: (a) Lacy cover specimen and (b) a zoomed in view of the automatic lacy cover formation..

in a pit width that is too large and a higher value in a too small size. Figure 10a shows the comparison between the numerical model and the experimental data. The largest distance from the centre line of the pit to a point in the pit that is in contact with the outside environment is defined as the width of the pit. Furthermore, Fig. 10b gives the comparison of the pit depth, which shows that there is a small dependency of the depth with respect to c_{pas} . A higher c_{pas} reduces the metal concentration gradient and therefore the pit propagation speed at the bottom of the pit.

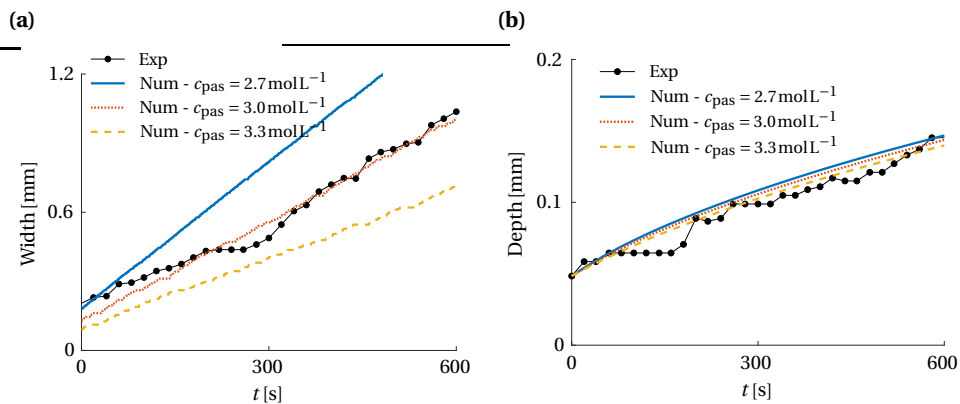


Figure 10: Comparison of (a) the width and (b) the depth of 2D pit numerical analyses (Num) with passivation for different c_{pas} against experiment (Exp).

6.4. Influence of mechanical load

The influence of mechanical loading on the pit growth behaviour is studied using the specimen given in Fig. 11 for which the condition of plane stress has been used. The specimen width and height are equal to $800 \mu\text{m}$ and $400 \mu\text{m}$, respectively. Furthermore, the initial pit radius is $50 \mu\text{m}$. The mesh size was set to $2 \mu\text{m}$ and the length scale r_w from Eq. (4.26) equal to $4 \mu\text{m}$. The dashed line, which indicates the presence of a notch,

shows the general evolution of the shape of a pit under mechanical loading having a circle as initial pit shape. The notch is formed at the bottom of the pit because it is subjected to the highest amount of stress and thus experiences the highest increase in front velocity. Due to this notch, there is an increase in stress concentration [48], which further accelerates the growth of the notch. Passivation is not considered in this study.

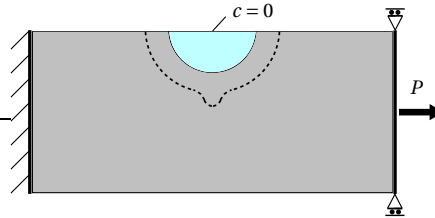


Figure 11: Mechanical stress assisted pit growth specimen. The dashed line indicates the evolution of the pit shape.

Figure 12a shows the pit depth and Fig. 12b the equivalent dislocation strain for simulations under a low current density of $i_A = 1 \text{ mA/mm}^2$ in the case without mechanical loading (NL), constant applied loading (Const) and cyclic loading (Cyclic) with a load ratio of -1 for different maximum loads and different cyclic load frequencies. The low (LL) and high (HL) maximum loads are equal to 7 N mm^{-1} and 18 N mm^{-1} , respectively. It can be seen that the pit without mechanical loading is growing slowest. For the low applied load, plasticity is not present. In this case, the pit grows faster under a constant applied loading as compared to cyclic loading, because the hydrostatic stress, which increases the corrosion speed according to Eq. (4.13), is always at its maximum, unlike under cyclic loading. Furthermore, for the low load there is no difference in pit growth for different load frequencies, because the percentage of time that is spent at a certain load is the same.

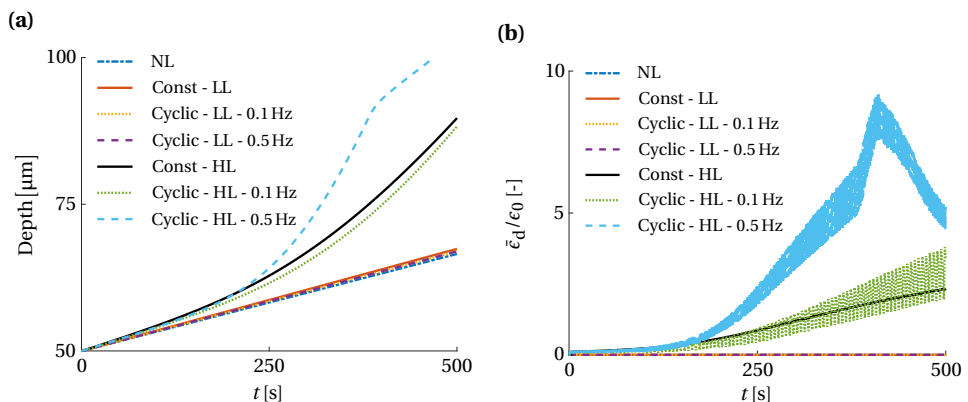


Figure 12: (a) Pit depth and (b) equivalent dislocation strain over time for $i_a = 1 \text{ mA/mm}^2$

This is different for the high maximum applied load, due to the presence of plasticity. The high frequency cyclic load case results in significantly faster pit growth compared to

the low frequency cyclic load case and the constant load case. This is due to the accumulation of the equivalent dislocation strain due to cyclic hardening. The effect becomes apparent after around 200 s, when a notch starts to develop (see Fig. 11) at the bottom of the pit which increases the stress concentration [48]. This increases the stress amplitude and therefore also the effect of kinematic hardening. Interestingly, under a constant load case the pit grows faster than under a cyclic load with a low frequency. In the case of the low frequency there is less time to be available for $\bar{\epsilon}_d$ to increase, because the material is already corroded before it can reach its potential maximum. However, the low frequency cyclic load case comes closer to the constant load case over time. This is explained again through the change in shape of the pit, the stress at the pit bottom increases and thus also the built up of $\bar{\epsilon}_d$.

Note that $\bar{\epsilon}_d$ is increasing and decreasing over time for the cyclic load cases according to its definition given in Eq. (4.14). Also, for the high frequency cyclic load there is a change in behaviour around 380 s, which is due to the switch from activation to diffusion control at the bottom of the notch. As could be seen in Section 6.2, diffusion control reduces the curvature of a pit. Consequently, a flatter pit means a smaller stress concentration and thus a decrease of $\bar{\epsilon}_d$ as the pit grows.

A comparison between the shape of the pit for the high maximum applied load cases and without mechanical load is given in Fig. 13. The pits under a mechanical load develop a notch at the pit bottom. It is not difficult to imagine that such notch is a precursor for crack initiation. Furthermore, it can be seen that for the high frequency cyclic load case the notch forming grows faster with time. The cause is again kinematic hardening, which leads to earlier notch forming, which results in a reduction in stress and therefore in corrosion rate at the rest of the pit front.

Finally, the simulations are repeated with a larger anodic current density of $i_A = 10 \text{ mA/mm}^2$. Figure 14 shows a comparison of the pit depth for the different load scenarios. For all simulations the bottom of the pit is under diffusion control, which implies that mechanical loading does not affect the pit growth rate at these locations and results are the same. However, it can be questioned whether this is realistic, because the salt layer, causing the diffusion control phenomenon, might break down in the case of mechanical loading. Upon break down, larger pit growth rates may be expected as the problem is no longer controlled by diffusion but by activation.

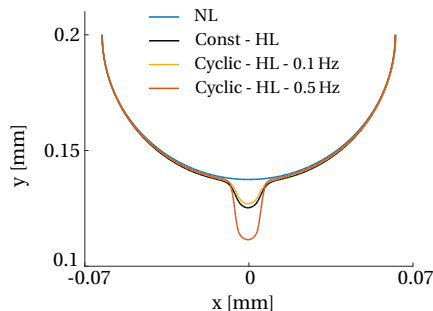


Figure 13: Shape of pit at $t = 350 \text{ s}$ for different load cases for $i_a = 1 \text{ mA/mm}^2$

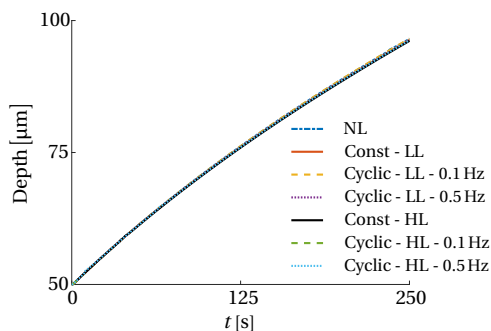


Figure 14: Pit depth over time for $i_a = 10 \text{ mA/mm}^2$

7. Conclusions

This study presented a numerical 2D model for corrosion pit propagation under mechanical loading. The level set method was used to track the pit front and to split the domain into a solid domain and a pit domain. The field equations used for the level set reinitialization as well as the velocity extension enable the model to be extended for the use of different mesh types and also 3D analyses.

In the pit domain the diffusion of the concentration of atoms is simulated. The atoms originate from the dissolution process occurring at the pit front. The equilibrium between the propagation velocity of the pit front and the flux through dissolution is defined by the Rankine-Hugoniot front condition. The implementation of the front conditions depends on the regime of corrosion, which can be activation control, diffusion control or passivation. These three regimes are required in order to simulate the formation of a lacy cover.

In the solid domain static equilibrium is solved to obtain the strains and stresses. Because the equivalent plastic strain grows indefinitely under cyclic loading, which is physically unrealistic, a new parameter called the equivalent dislocation strain, that depends on the signs of the plastic strain increment and the back stress, was introduced. The new state variable shows a better match with theoretical understanding of how dislocation pile-ups evolve under cyclic loading. However, it still needs to be validated quantitatively.

According to the implemented model a combination of activation control and an elastic material response, results in faster pit propagation under constant loading than under cyclic loading given the same maximum load. However, in the presence of plastic deformation, cyclic loading can significantly increase the pit growth rate. Furthermore, increasing the cyclic load frequency results in faster pit propagation as there are more cycles to build up plastic strain to kinematic hardening before the material is dissolved into the pit. In the case of diffusion control, mechanical loading does not influence the pit growth rate, provided that the salt layer leading to diffusion control remains intact.

Acknowledgements

This research is part of the EUROS program, which is supported by NWO domain Applied and Engineering Sciences and partly funded by the Ministry of Economic Affairs.

Data Availability Statement

The data that support the findings of this study are available from the corresponding author upon reasonable request.

References

- [1] E. McCafferty, *Introduction to corrosion science* (Springer Science & Business Media, 2010).
- [2] G. S. Frankel, *Pitting corrosion of metals: A review of the critical factors*, Journal of The Electrochemical Society **145**, 2186 (1998).
- [3] G. Zhang and Y. Cheng, *Localized corrosion of carbon steel in a CO₂-saturated oil-field formation water*, Electrochimica Acta **56**, 1676 (2011).
- [4] R. E. Melchers, *Pitting Corrosion of Mild Steel in Marine Immersion Environment—Part I: Maximum Pit Depth*, Corrosion **60**, 824 (2004).
- [5] Y. Kondo, *Prediction of fatigue crack initiation life based on pit growth*, Corrosion **45**, 7 (1989).
- [6] P. Ernst and R. Newman, *Pit growth studies in stainless steel foils. i. introduction and pit growth kinetics*, Corrosion Science **44**, 927 (2002).
- [7] S. Scheiner and C. Hellmich, *Stable pitting corrosion of stainless steel as diffusion-controlled dissolution process with a sharp moving electrode boundary*, Corrosion Science **49**, 319 (2007).
- [8] S. Scheiner and C. Hellmich, *Finite volume model for diffusion- and activation-controlled pitting corrosion of stainless steel*, Computer Methods in Applied Mechanics and Engineering **198**, 2898 (2009).
- [9] N. Laycock and R. Newman, *Temperature dependence of pitting potentials for austenitic stainless steels above their critical pitting temperature*, Corrosion Science **40**, 887 (1998).
- [10] N. Laycock and S. White, *Computer simulation of single pit propagation in stainless steel under potentiostatic control*, Journal of the Electrochemical Society **148**, B264 (2001).
- [11] S. Sarkar, J. E. Warner, and W. Aquino, *A numerical framework for the modeling of corrosive dissolution*, Corrosion Science **65**, 502 (2012).
- [12] R. Duddu, *Numerical modeling of corrosion pit propagation using the combined extended finite element and level set method*, Computational Mechanics **54**, 613 (2014).
- [13] A. S. Vagbharathi and S. Gopalakrishnan, *An extended finite-element model coupled with level set method for analysis of growth of corrosion pits in metallic structures*, Proceedings of the Royal Society A: Mathematical, Physical and Engineering Sciences **470** (2014).
- [14] R. Duddu, N. Kota, and S. M. Qidwai, *An Extended Finite Element Method Based Approach for Modeling Crevice and Pitting Corrosion*, Journal of Applied Mechanics **83** (2016), 081003.

-
- [15] W. Mai, S. Soghrati, and R. Buchheit, *A phase field model for simulating the pitting corrosion*, Corrosion Science **110**, 157 (2016).
- [16] W. Mai and S. Soghrati, *A phase field model for simulating the stress corrosion cracking initiated from pits*, Corrosion Science **125**, 87 (2017).
- [17] W. Mai and S. Soghrati, *New phase field model for simulating galvanic and pitting corrosion processes*, Electrochimica Acta **260**, 290 (2018).
- [18] C. Lin, H. Ruan, and S. Shi, *Phase field study of mechanico-electrochemical corrosion*, Electrochimica Acta **310**, 240 (2019).
- [19] S. Jafarzadeh, Z. Chen, J. Zhao, and F. Bobaru, *Pitting, lacy covers, and pit merger in stainless steel: 3d peridynamic models*, Corrosion Science **150**, 17 (2019).
- [20] H. Wang and E. Han, *Simulation of metastable corrosion pit development under mechanical stress*, Electrochimica Acta **90**, 128 (2013).
- [21] O. Fatoba, R. Leiva-Garcia, S. Lishchuk, N. Larrosa, and R. Akid, *Simulation of stress-assisted localised corrosion using a cellular automaton finite element approach*, Corrosion Science **137**, 83 (2018).
- [22] C. Lin and H. Ruan, *Multi-phase-field modeling of localized corrosion involving galvanic pitting and mechano-electrochemical coupling*, Corrosion Science **177** (2020).
- [23] E. M. Gutman, *Mechanochemistry of materials* (Cambridge Int Science Publishing, 1998).
- [24] S. Osher and J. Sethian, *Fronts propagating with curvature-dependent speed: Algorithms based on hamilton-jacobi formulations*, Journal of Computational Physics **79**, 12 (1988).
- [25] A. Hansbo and P. Hansbo, *An unfitted finite element method, based on nitsche's method, for elliptic interface problems*, Computer Methods in Applied Mechanics and Engineering **191**, 5537 (2002).
- [26] J. Mergheim, E. Kuhl, and P. Steinmann, *A finite element method for the computational modelling of cohesive cracks*, International Journal for Numerical Methods in Engineering **63**, 276 (2005).
- [27] F. van der Meer and L. Sluys, *A phantom node formulation with mixed mode cohesive law for splitting in laminates*, International Journal of Fracture **158**, 107 (2009).
- [28] S. Sharland, C. Jackson, and A. Diver, *A finite-element model of the propagation of corrosion crevices and pits*, Corrosion Science **29**, 1149 (1989).
- [29] S. Sarkar and W. Aquino, *Electroneutrality and ionic interactions in the modeling of mass transport in dilute electrochemical systems*, Electrochimica Acta **56**, 8969 (2011).

- [30] X. Sun and R. Duddu, *A sequential non-iterative approach for modeling multi-ionic species reactive transport during localized corrosion*, Finite Elements in Analysis and Design **166**, 103318 (2019).
- [31] M. Mainguy and O. Coussy, *Propagation fronts during calcium leaching and chloride penetration*, Journal of Engineering Mechanics **126**, 250 (2000).
- [32] J. Chaboche, *Constitutive equations for cyclic plasticity and cyclic viscoplasticity*, International Journal of Plasticity **5**, 247 (1989).
- [33] J. Chaboche, *On some modifications of kinematic hardening to improve the description of ratchetting effects*, International Journal of Plasticity **7**, 661 (1991).
- [34] S. Sharland and P. Tasker, *A mathematical model of crevice and pitting corrosion - I. The physical model*, Corrosion Science **28**, 603 (1988).
- [35] O. U. Colak, *Kinematic hardening rules for modeling uniaxial and multiaxial ratchetting*, Materials & Design **29**, 1575 (2008).
- [36] J. A. Sethian, *Level set methods and fast marching methods: evolving interfaces in computational geometry, fluid mechanics, computer vision, and materials science* (Cambridge university press, 1999).
- [37] F. van der Meer, N. Moës, and L. Sluys, *A level set model for delamination - modeling crack growth without cohesive zone or stress singularity*, Engineering Fracture Mechanics **79**, 191 (2012).
- [38] T. Adams, S. Giani, and W. M. Coombs, *A high-order elliptic pde based level set reinitialisation method using a discontinuous galerkin discretisation*, Journal of Computational Physics **379**, 373 (2019).
- [39] R. De Borst, M. Crisfield, J. Remmers, and C. Verhoosel, *Nonlinear finite element analysis of solids and structures* (John Wiley & Sons, 2012).
- [40] T. Belytschko, W. Liu, B. Moran, and K. Elkhodary, *Nonlinear finite elements for continua and structures* (John wiley & sons, 2013).
- [41] A. Khoei, *Extended finite element method: Theory and applications*, Extended Finite Element Method: Theory and Applications , 1 (2015).
- [42] G. Wells and L. Sluys, *A new method for modelling cohesive cracks using finite elements*, International Journal for Numerical Methods in Engineering **50**, 2667 (2001).
- [43] R. Dekker, F. van der Meer, J. Maljaars, and L. Sluys, *A cohesive XFEM model for simulating fatigue crack growth under mixed-mode loading and overloading*, International Journal for Numerical Methods in Engineering **118**, 561 (2019).
- [44] M. Haufeille, C. Annavarapu, and J. Dolbow, *Robust imposition of dirichlet boundary conditions on embedded surfaces*, International Journal for Numerical Methods in Engineering **90**, 40 (2012).

-
- [45] M. Latifi, F. van der Meer, and L. Sluys, *A level set model for simulating fatigue-driven delamination in composites*, *International Journal of Fatigue* **80**, 434 (2015).
- [46] F. Antunes, M. Ferreira, R. Branco, P. Prates, C. Gardin, and C. Sarrazin-Baudoux, *Fatigue crack growth versus plastic CTOD in the 304L stainless steel*, *Engineering Fracture Mechanics* **214**, 487 (2019).
- [47] G. T. Gaudet, W. T. Mo, T. A. Hatton, J. W. Tester, J. Tilly, H. S. Isaacs, and R. C. Newman, *Mass transfer and electrochemical kinetic interactions in localized pitting corrosion*, *AIChE Journal* **32**, 949 (1986).
- [48] M. Cerit, K. Genel, and S. Eksi, *Numerical investigation on stress concentration of corrosion pit*, *Engineering Failure Analysis* **16**, 2467 (2009).

5

A three dimensional level set model for stress-assisted pitting corrosion

R. Dekker^a , F.P. van der Meer^a, J. Maljaars^{b,c}, L.J. Sluys^a

^a Faculty of Civil Engineering and Geosciences, Delft University of Technology, Delft, The Netherlands

^b Faculty of Built Environment, Eindhoven University of Technology, Eindhoven, The Netherlands

^c Structural reliability, TNO ,Delft, The Netherlands

ABSTRACT

This study presents a 3D numerical model for stress-assisted pitting corrosion in metals. A level set model is combined with the finite element method to implicitly track the corrosion front by dividing the domain into a pit domain and a solid domain. In the pit domain the diffusion of metals ions, originating from the anodic corrosion process at the front, is modelled. In the solid domain the static equilibrium equation is solved in order to obtain the elastic, and plastic, strains and stresses. The numerical model is compared against stress-assisted pitting corrosion experiments in 3D under fatigue loading.

1. Introduction

Pitting corrosion in metals is a phenomenon that can be present in the inner sections of monopile foundations of offshore wind turbines [1]. In the past, pitting corrosion has been the cause of numerous disastrous failures in offshore structures [2]. Having numerical models that can more accurately predict pitting corrosion could mitigate the risk associated with pitting and therefore also reduce the total costs attached to pitting corrosion [3]. However, accurate simulation of pitting corrosion is challenging as it requires the interaction of different chemical processes on a domain with evolving boundaries. The development of reliable models is further complicated by the possible interaction between pitting corrosion and mechanical loading. This interaction can work both ways. On the one hand, an applied mechanical load can increase the pitting corrosion rate. On the other hand, corrosion pits act as stress concentration sites, which decreases the fatigue life time in the case of cyclic mechanical loading.

Considerable research has been done towards the development of two-dimensional (2D) numerical models for pitting corrosion. The most common methods for modelling pit growth involve phase field models [4–8], adaptive meshing techniques [9–11], finite volume models [12, 13], level set approaches [14, 15], cellular automata models [16, 17] and peridynamic models [18, 19]. Stress-corrosion cracking was modelled by Mai and Soghrati [5] and Jafarzadeh et al. [19], who incorporated the effect of an elastic mechanical stress on the pit growth rate. On top of that, Jafarzadeh et al. [19] not only developed a numerical model, but also performed an experiment suitable for 2D validation. The influence of both elastic and plastic mechanical behaviour on the pit growth rate was taken into account by Wang and Han [16], and Fatoba et al. [17], where the latter presented new experimental data for validation as well. However, all these 2D models for mechanically-assisted pit corrosion are only valid if both the corrosion and the mechanical behaviour can be simulated using a 2D plane or an axisymmetric model.

Recently, more studies also focus on numerical models for pitting corrosion in 3D. Among these, phase field [20, 21], peridynamics [22–25] and cellular automata models [26, 27] are most popular. Some of these models also included the effect of a mechanical stress on the pit growth rate, mainly to capture stress-corrosion cracking [21, 25]. However, none include the effect of plasticity on pitting corrosion and none consider corrosion under fatigue loading. Furthermore, only minor quantitative validation is performed with experimental data, which emphasizes the lack of proper benchmark tests for all these pitting corrosion models. The authors found only one study that contained a quantitative validation with a 3D experiment [17], although in that study the comparison was done against a 2D numerical model.

In recent work, the authors developed a 2D level set model combined with the finite element method to capture mechanical stress-assisted stable pitting corrosion in metals under constant and cyclic loading [28]. Here, the framework is extended to accommodate 3D analyses, which only required a modification of the triangulation process to tetrahedron partitioning. Furthermore, the model is compared against experiments performed by [17] in which pitting corrosion with and without mechanical loading is considered. The considered case involves uniaxial loading and a semi-spherical pit, the

combination of which cannot be modelled in 2D.

The paper starts by presenting the numerical framework used to solve the stress-assisted pitting corrosion problem. Next, the corrosion behaviour is discussed. After that, the mechanical problem together with the equations that describe the mechanical behaviour of the material are presented. In the next section, the numerical framework is shortly reviewed. Finally, three numerical examples are presented. Firstly, the numerical model is compared against an analytical relation for a 1D pencil test under diffusion controlled corrosion. Secondly, a comparison of a 3D pit is performed between the numerical model and experimental data. Finally, the numerical model is compared against experiments on 3D pit growth under flow with and without mechanical cyclic loading. The flow is not modelled explicitly, but it is assumed that the general effect of this flow can be captured by using an appropriate boundary condition.

2. Numerical framework

A schematic of the numerical method in which the finite element method is combined with the level set method in order to simulate the pitting corrosion process in the presence of a mechanical stress is given in Fig. 1. The framework captures the movement of the pit front in time as a result of anodic dissolution, which means that metal ions originating from the solid dissolve into the electrolyte in the pit. Simultaneously, a cathodic reaction is present where electrons are consumed, for example to form hydrogen gas out of hydrogen anions. It is assumed that the corrosion rate is only limited by the anodic reaction rate and not by the cathodic one. Therefore, the presented model only considers the anodic reaction. Additionally, the solid experiences mechanical stresses and strains due to an applied mechanical cyclic load, which can increase the anodic current density [29], and thereby possibly the corrosion speed.

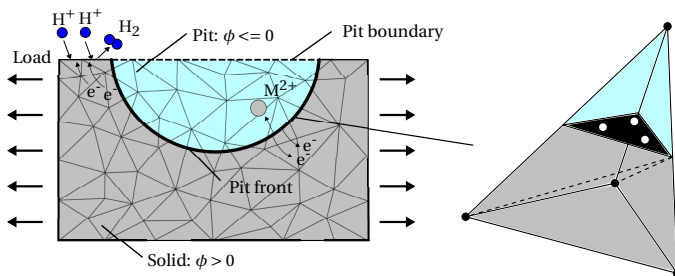


Figure 1: A specimen with a corrosion pit exposed to a mechanical load in a combined finite element and level set method framework. Elements cut by the pit front are both present in the solid and the pit, but use different integration schemes depending on the domain.

The moving pit front splits the numerical domain into a pit and a solid domain. The level set method is used to track the front implicitly by assigning each node a signed distance value ϕ with a magnitude equal to the shortest distance between the node and the front. The node is located in the pit domain if ϕ is negative or equal to zero, whereas it is located in the solid domain if ϕ is positive.

The solid domain and the pit domain consist of the elements located on respective side of the front. The elements that are cut by the front are located in both domains. However, for the solid domain only the volume above the front ($\phi > 0$) is integrated, while for the pit domain only the volume below. The specific integration volumes are developed by tetrahedral partitioning as visualized in Fig. 1 for a tetrahedron element, which shows one possible example on how an element could be split by the front. In this example, the volume part belonging to the pit domain is already a tetrahedron. However, the solid part is not, and is therefore split into two separate tetrahedrons by including an extra plane which requires inserting the two dashed lines. The elements cut by the pit front are called the front elements and their respective nodes the front nodes. The section of the front inside a single front element is represented by a surface element, indicated by the black surface, containing the front integration points, indicated by the white dots. The regime of corrosion, the stresses, the strains and the local front velocity are all computed at the front integration points.

A staggered approach consisting of several different processes is used to tackle the stress-assisted pitting corrosion problem. The flow diagram given in Fig. 2 shows the type and order of these processes. It starts by defining an initial pit front by means of initializing the level set, which means each node is given an initial signed distance value. Next, the level set update is performed, followed by the reinitialization process.

After that, an additional action, not present in the previous work [28], is introduced such that cycle jumps can be included when considering cyclic loading in order to improve the computational efficiency. Before going into the mechanical problem the applied load is defined. After that, the mechanical and the diffusion problems are solved. If the applied load is the final load step of a single load cycle, the average velocity at each front integration point over the cycle is computed. Otherwise, the load step is incremented and the process is repeated again. A consequence of this approach is that the time increment is only present in the level set update process, which means that the load step is disconnected from the time increment. Here, the time increment represents a certain amount of cycles, which depends on the loading frequency considered. Any possible loading frequency effects on the pit growth rate which arise when having the time and load connected are therefore not captured. An example of such an effect is cyclic hardening, which can be significantly smaller when considering cycle jumps. When no mechanical load is applied, the mechanical problem is simply skipped and there will be no check for end of load cycle after the corrosion problem.

After having computed the front velocities, which is a load cycle average velocity in the case of cyclic loading, the velocities are extended to the front nodes, followed by the rest of the domain. In the next sections, the different steps and processes are discussed in more detail.

3. Corrosion problem

Metal ions originating from the solid diffuse into the pit domain. The concentration of metal ions is largest near the pit front and smallest near the pit boundary, which is the

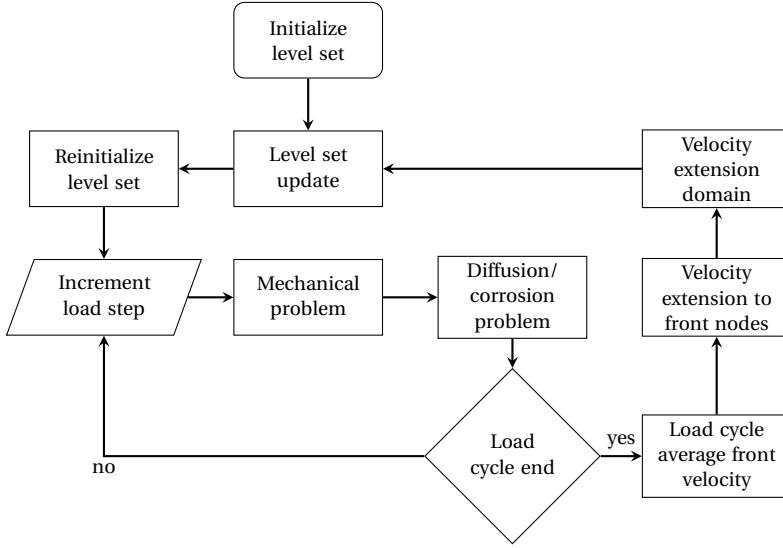


Figure 2: Flow diagram of the mechanical stress-assisted pitting corrosion model

outside environment (see Fig. 1). The diffusion equation, in the absence of any concentration source, is defined as follows:

$$\frac{\partial c}{\partial t}(\mathbf{x}, t) + \nabla \cdot \mathbf{J}(\mathbf{x}, t) = 0 \quad (5.1)$$

in which c is the concentration of atoms/ions, \mathbf{J} is the flux of atoms, \mathbf{x} is the location in the domain and t is the time. The rate of diffusion is generally significantly faster than the rate of dissolution [14]. As a result, steady state can be assumed, which means that $\frac{\partial c}{\partial t}(\mathbf{x}, t) = 0$. In this study, only the concentration of atoms of the metal itself is considered, however, inclusion of other species is possible as well [11, 30–32]. Furthermore, it is assumed that the dissolved ions only move under diffusion [33], which means the flux can be computed using Fick's law:

$$\mathbf{J}(\mathbf{x}, t) = -D\nabla c(\mathbf{x}, t) \quad (5.2)$$

in which D is the diffusion coefficient of the metal in the electrolyte.

As a consequence of the corrosion reaction, the pit front moves into the solid domain. The pit domain increases in size, while the size of the solid domain decreases. The equilibrium between the flux of dissolved metal atoms and the velocity of the propagation pit front follows the Rankine-Hugoniot condition [12, 34]:

$$\{-D\nabla c(\mathbf{x}, t) + [c_{\text{solid}} - c(\mathbf{x}, t)]\mathbf{V}(\mathbf{x}, t)\} \cdot \mathbf{n}(\mathbf{x}, t) = 0 \quad (5.3)$$

Here, the front velocity is indicated by \mathbf{V} , the unit normal vector perpendicular to the front by \mathbf{n} and the metal atom concentration in the solid by c_{solid} .

The process of stable pitting corrosion can be divided into three different regimes. It is possible that along the front of a single pit different regimes occur at the same time. In

the first regime, called activation controlled corrosion, the speed of corrosion is known *a priori* and acts as an input to the pit front boundary condition for the pit domain. In the second regime, called diffusion controlled corrosion, the speed of corrosion depends on the speed with which metal ions can diffuse away from the pit front. In the third regime, called passivation, the corrosion process simply stops, which behaviour is crucial for the phenomenon of lacy cover formation. In this study, only activation and diffusion controlled corrosion are considered. Passivation control and lacy cover formation is studied in [28].

3.1. Activation control

In pitting corrosion under activation control the front condition given in Eq. (5.3) acts as a mixed or Robin boundary condition which depends on a front velocity that is known *a priori*. The front velocity can be computed with the following equation:

$$\mathbf{V}(\mathbf{x}, t) = \frac{i_a \mathbf{n}(\mathbf{x}, t)}{c_{\text{solid}} z F} \quad (5.4)$$

where F indicates Faraday's number and z is the number of electrons involved. In this study, the anodic current density i_a is used as an input, although it also can be computed from the applied potential using the Butler-Volmer equation [12–14]. Furthermore, it is assumed that the current density only acts perpendicular to the pit front.

According to Gutman [29], the presence of a plastic strain \bar{p} and a hydrostatic stress σ_H increases the anodic current density of a metal according to the following equation:

$$i_a \rightarrow i_a \left(\frac{\bar{p}}{\epsilon_0} + 1 \right) \exp \left(\frac{|\sigma_H| V_m}{RT} \right) \quad (5.5)$$

where ϵ_0 is the initial yield strain, V_m the molar volume, R the universal gas constant and T the temperature. The equivalent plastic strain $\bar{\epsilon}_p$, given in Eq. (5.12), is commonly used as \bar{p} [16, 17]. However, it has the unrealistic ability to grow indefinitely under cyclic loading. Therefore, a new parameter for \bar{p} that does not show this indefinite growth was introduced by the authors [28], called the equivalent dislocation strain $\bar{\epsilon}_d$, which depends on the signs of the plastic strain increment $d\epsilon_p$ and the back stress β (see Eq. (5.13)):

$$d\bar{\epsilon}_d = \int_0^{d\bar{\epsilon}_p} \text{sgn}(d\epsilon_p \cdot \beta) d\bar{\epsilon}_p \quad (5.6)$$

3.2. Diffusion control

Activation controlled corrosion turns into diffusion controlled corrosion once the saturation concentration c_{sat} is reached on the inside of the pit front. At this point, a salt layer forms, preventing the concentration from exceeding c_{sat} . Under diffusion controlled corrosion, the saturation concentration is applied as Dirichlet boundary condition on the inside of the front. This means that the front condition given in Eq. (5.3) is no longer

applied as a boundary condition for the diffusion problem. Instead, the front condition is used to compute the now unknown velocity of the front after the concentrations throughout the pit domain have been determined:

$$V_n(\mathbf{x}, t) = \frac{D\nabla c \cdot \mathbf{n}}{c_{\text{solid}} - c_{\text{sat}}} \quad (5.7)$$

where $V_n = \mathbf{Vn}$ is the normal velocity of the front. Note that the front velocity is now independent of the anodic current density and therefore the plastic strain and the hydrostatic stress do not increase the front velocity any more.

3.3. Corrosion regime control

Activation and diffusion control can occur simultaneously along the pit front. The type of regime for each front integration point at each time step is determined according to the following scheme:

1. Set the regime of corrosion to activation control for each front integration point
 - Include the effect of mechanical loading
2. Compute the concentration distribution throughout the pit domain for the current corrosion regime configuration
3. Compute the concentration c_{front} at each front integration point
 - Switch the regime to diffusion control for the specific integration point when $c_{\text{front}} > c_{\text{sat}}$
4. The corrosion regime configuration has converged if there has not been any switch in regime in step 3 for any front integration point. The steps 2 and 3 should be repeated as long as there is no convergence in the configuration.

5

The Dirichlet boundary condition, required for diffusion control, is enforced using Nitsche's method for embedded surfaces [35]. Note that the front will have both Dirichlet and Robin boundary conditions when both diffusion and activation control are present.

4. Mechanical problem

The applied load is transferred through the solid domain, in which therefore static equilibrium should hold. In the absence of any body forces, the equilibrium equation used to compute the nodal displacements can be written as:

$$\nabla \cdot \sigma = 0 \quad (5.8)$$

where σ is the mechanical stress and ∇ the differential operator.

The values of σ_H and \bar{p} are required at the front integration points, such that the effect of the mechanical load on the pit growth rate can be included. These quantities are computed following a non-local approach by introducing an extra length-scale [36, 37]. This is done to avoid strong mesh dependencies through local plastic behaviour. The non-local quantities are computed by means of a weighted average of the stress and strain values from the solid bulk integration points. The respective weight function is given by:

$$w = \frac{1}{(\pi r_w)^2} \exp\left(-\frac{l_w^2}{2r_w^2}\right) \quad (5.9)$$

where l_w is the distance between the integration point of the solid and the front and r_w is the scale-length that also defines the search radius around a front integration point.

Note that the integration scheme of the elements containing a front section continuously change under a moving front. Therefore, it is important that all history data concerning plastic deformation are properly transferred from the old solid integration points to the new ones. This is done by first extrapolating the data from the old solid integration points to the nodes, after which an interpolation is performed to obtain the history data in the new integration points [38].

To correctly capture plastic flow under cyclic loading it is important that in addition to isotropic hardening, kinematic hardening is included in the model. The elastic material behaviour is modelled according to Hooke's law having a Young's modulus E and a Poisson ratio ν .

The yield surface f_{vm} is described by means of the Von Mises criterion:

$$f_{vm} = \sqrt{\frac{2}{3}(\mathbf{s} - \boldsymbol{\beta}) : (\mathbf{s} - \boldsymbol{\beta})} - \sigma_y \quad (5.10)$$

in which \mathbf{s} are the deviatoric stresses and $\boldsymbol{\beta}$ the back stresses. The evolution of the yield stress σ_y is defined by a non-linear isotropic hardening rule [39]:

$$\sigma_y = \sigma_0 + Q_\infty \left(1 - e^{-b\bar{\epsilon}_p}\right) \quad (5.11)$$

in which σ_0 , Q_∞ and b are the initial yield stress, the limit value for the yield stress increase and a measure for the rate of change of the yield surface, respectively. The equivalent plastic strain increment is defined as a function of the plastic strain increment:

$$d\bar{\epsilon}_p = \sqrt{\frac{2}{3}d\epsilon_p : d\epsilon_p} \quad (5.12)$$

The kinematic hardening rule is given by [40]:

$$d\boldsymbol{\beta} = \sum_{i=1}^3 \left(\frac{2}{3} C_i d\epsilon_p - \gamma_i \beta_i d\bar{\epsilon}_p \right) \quad (5.13)$$

where C_i and γ_i are the linear and the non-linear kinematic hardening coefficients.

5. Level set processes

In order for the level set method to work, the signed distance property should be met at each node. Furthermore, the velocity of the front is required to be known at the nodes such that the nodal signed distance values can be updated. The three different processes used by the level set method: reinitialization, velocity extension and level set update are discussed next.

5.1. Reinitialization

The signed distance property is ensured by reinitializing the signed distance value of every node such that it satisfies the Eikonal equation:

$$|\nabla\phi| - 1 = 0 \quad (5.14)$$

The reinitialization process follows the field equations procedure presented by Adams et al. [41] under the assumption that the signed distance values of the front nodes are known [28]. The advantage of a field equation is that it can be used for any type of element for any spatial dimension. The disadvantage of this method is its high demand in computation time. However, by reducing the reinitialization domain to a band of elements around the front, the computation time can be significantly reduced. The band elements, as indicated in Fig. 3, consist of the front elements plus extra elements from the solid domain which are within a certain distance from the front. Note that there is no need to include elements that are purely in the pit domain, because the pit front only moves outwards into the solid domain. Furthermore, it is not required to do the reinitialization step after every level set update. It can be performed every five or ten steps, depending on the complexity of the front geometry [42].

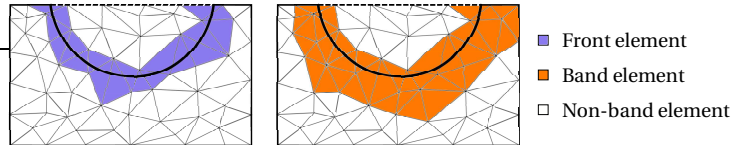


Figure 3: Front and band elements around the pit front

5.2. Velocity extension

The extension of the front velocity to the nodes can be performed with the following equation:

$$\nabla V_n \cdot \nabla\phi = 0 \quad (5.15)$$

As discussed in [28], the above equation is turned into a weak form and solved in the form of a field equation.

Figure 2 shows that the velocity extension is conducted in two separate steps. In the first step the velocity is extended from the front to the front nodes using Eq. (5.15), which is

done by using a penalty method to enforce the boundary conditions on the front [35]. In the second step, the velocity at the front nodes is extended to the rest of the band elements, using the same equation, but this time using the velocities at the front nodes as Dirichlet boundary conditions. The reason for separating the process into two steps is related to a certain degree of non-uniqueness in the extension of the velocity from the front to the front nodes. Before performing the second step, the velocity in the front nodes are assessed to ensure that its magnitude is within the velocity range of the adjacent pit front sections and is otherwise assigned the maximum or minimum front velocity of the adjacent sections.

5.3. Level set update

The level set update is performed for the nodes belonging to the band elements by means of the following relation:

$$\phi^{t+\Delta t} = \phi^t - V_n \Delta t \quad (5.16)$$

The magnitude of the time increment Δt is limited by the Courant-Friedrichs-Lewy (CFL) condition to ensure stability of the solution [42].

The pit front moves towards the solid domain for every level set update. Consequently, the front surface elements and the integration volumes should be replaced and, possibly, the nodes and elements originally present in the solid domain shift to the pit domain. The new pit nodes are assigned concentration degrees of freedom and are disposed of their displacement degrees of freedom.

6. Numerical examples

This section starts with a comparison between the numerical model and an analytical relation for the so-called 1D pencil test. After that, the model is compared against a set of experiments performed by Fatoba et al. [17], namely standard 3D pitting corrosion, 3D pitting corrosion with fluid flow, and stress-assisted 3D pitting corrosion under cyclic loading with fluid flow. The metal that is considered is an API X65 steel. The model input parameters used in all numerical examples are given in Table 1, where the values of c_{sat} and D belong to a temperature of 298.15 K. The saturation concentration was taken from [43]. The mechanical material parameters are taken from Pereira et al. [44], where only kinematic hardening is considered, which means that only the translation of the yield surface is captured and not the expansion. This means that Q_∞ and b from Eq. (5.11) are set to zero.

6.1. 1D pencil test

The geometry of the pencil test specimen and the boundary and initial conditions used in the analysis are given in Fig. 4a. The specimen is a cylinder with a flat corrosion front. The size of the tetrahedra mesh elements is equal to $2\ \mu\text{m}$. In this example only diffusion control is considered and no value for i_a is required. Furthermore, no mechanical load

is applied so that it can be compared to an analytical model. The pencil test is inherently a 1D problem, but it is modelled in 3D to verify the presented 3D model.

In Fig. 4b the pit growth velocity according to the numerical model is compared against an analytical relation [12]. It can be seen that the model results in the same pit growth rate as defined by the analytical relation. Furthermore, Fig. 5 shows the concentration distribution at 80, 480 and 880 seconds. It shows the expected concentration gradient in the pit.

Table 1: Model parameters and constants

c_{solid} [43]	c_{sat} [9]	D [9]	T	R		
143 molL^{-1}	4.54 molL^{-1}	$0.86 \times 10^{-3} \text{ mm}^2 \text{ s}^{-1}$	293.15 K	$8.314 \text{ JK}^{-1} \text{ mol}^{-1}$		
F	z	V_{m} [17]	E [44]	ν [44]	σ_0 [44]	
$96485.3 \text{ C mol}^{-1}$	2	$7049.24 \text{ mm}^3 \text{ mol}^{-1}$	211 GPa	0.3	475 MPa	
C_1 [44]	C_2 [44]	C_3 [44]	γ_1 [44]	γ_2 [44]	γ_3 [44]	r_w
$75 \times 10^3 \text{ MPa}$	$6 \times 10^3 \text{ MPa}$	50 MPa	900	35	2	80 μm

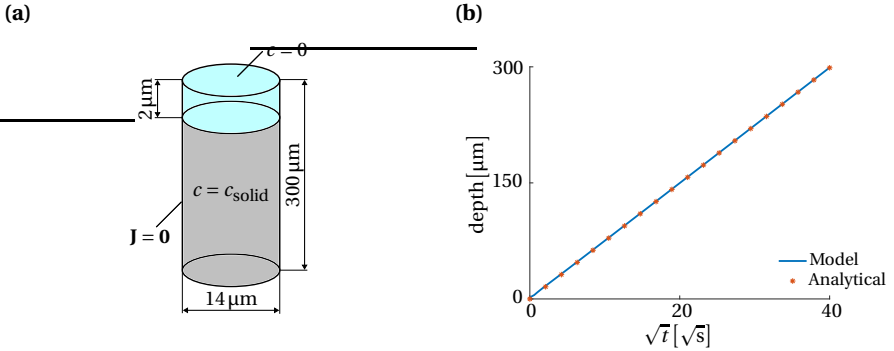


Figure 4: (a) 1D pencil test geometry and boundary conditions and (b) comparison of pit growth velocity between the numerical model and an analytical relation in the case of diffusion controlled corrosion.

6.2. 3D pitting corrosion

In the next numerical examples, the model is compared against experimental data taken from Fatoba et al. [17], who performed 3D pitting corrosion experiments. The geometry of the test specimen used in this paper to model the experiment is given in Fig. 6. While

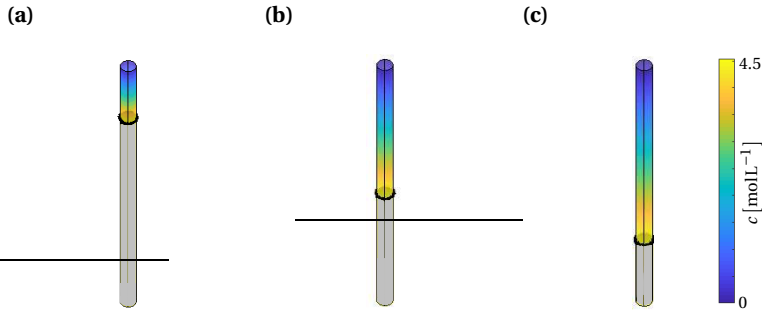


Figure 5: Pencil test concentration distribution at (a) 80, (b) 480 and (c) 880 seconds

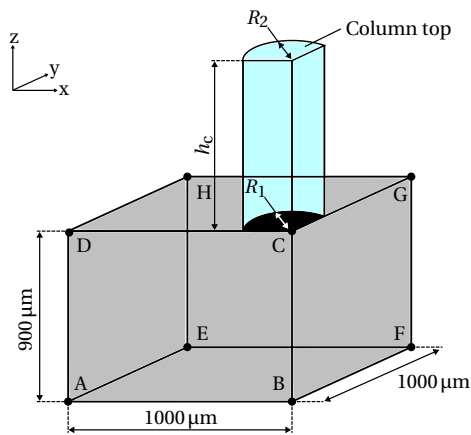


Figure 6: The 3D pitting corrosion geometry where the initial pit front is indicated by the black quarter circle located around node C.

the actual specimen is larger, only a portion of it is modelled to save computation time. For the same reason, only a quarter of the pit is considered. The geometry consists of a solid metal block with on top an electrolyte column that belongs to the pit domain. The initial pit front is a flat disk located where the electrolyte column touches the solid block, indicated by the black surface. Furthermore, depending on the experiment, the top radius R_2 and bottom radius R_1 of the column are not necessarily the same. The size of the tetrahedra mesh elements is equal to $35\ \mu\text{m}$. The length scale r_w from Eq. (5.9) is set to a value slightly larger than twice the element size.

Fatoba et al. [17] performed the corrosion experiments in three different settings, namely pit growth without fluid flow in the electrolyte column, pit growth with fluid flow and mechanically stress-dependent pit growth with fluid flow. Unfortunately, not all parameters regarding the geometry and the corrosion conditions are available. First of all, the height of the electrolyte column on top of the corrosion pit is unknown. Second, despite that the over-potential is known to be 1 V, the actual anodic current density is unknown. A literature search for the current density belonging to the presented over-

potential resulted in three different values. From [45] two values are obtained, namely $540 \mu\text{A mm}^{-2}$ and $300 \mu\text{A mm}^{-2}$, where the first quantity belongs to a specimen that has been immersed in the electrolyte for 24 hours and the second quantity to an immersion of one hour. A third current density value of $200 \mu\text{A mm}^{-2}$ is obtained from [46], but simulations with this value will not be shown here as they resulted in a significant under prediction of the pit growth rate compared to the experiments in the activation controlled phase of the pitting process. The bottom radius was given in [17] as $R_1 = 250 \mu\text{m}$.

6.2.1. No flow

In this experiment a pipette containing the electrolyte solution was placed on top of the metal specimen. Unfortunately, the type of pipette is unknown. Therefore, different pipette slopes $p_{\text{slope}} = \frac{R_2 - R_1}{h_c}$ are considered to determine its sensitivity. Three realistic slopes were used: 0.1, 0.15 and 0.2. Furthermore, no concentration boundary condition was applied at the top of the electrolyte column. This means that the metal ions entering the electrolyte cannot leave it, which leads to an increase in the overall ion concentration in the column. It was found that as long as the height of the specimen was sufficiently large, its actual value did not affect the results in the range of the experimental values. For this example, the column height was set to $8000 \mu\text{m}$. Also, an additional value for the bottom radius R_1 of $200 \mu\text{m}$ was used, because the exact dimensions of the droplet underneath the pipette is unknown.

The comparison between the numerical simulations with the experiment is presented in Fig. 7. It shows a total of four sub figures in which the pit depth and width for the two different current densities are plotted. Each graph has a total of six curves that follow from the numerical simulations. The dashed curves correspond to simulations with $R_1 = 200 \mu\text{m}$ and the solid ones to $R_1 = 250 \mu\text{m}$. Furthermore, the blue, red and yellow curves belong to a pipette of slope of 0.1, 0.15 and 0.2, respectively. It can be observed that initially, when the pit growth regime is activation control over the whole front, the growth rate is independent of the geometry size. However, the transition point from activation to diffusion control occurs later for larger p_{slope} . Furthermore, the sides of the pit convert earlier into diffusion control than the bottom of the pit, which is caused by the limited width of the electrolyte column. It can be concluded that an increase in p_{slope} , and therefore a faster increase in volume with respect to increasing distance from the solid surface, results in faster pit growth. This is caused by a combination of a longer activation control period and a higher concentration gradient under diffusion control for a given pit depth. Reducing the bottom radius slightly reduces the pit depth, which is also caused by a reduction in the concentration gradient. Finally, using a smaller initial radius results in a reduction in pit width.

Regarding the pit depth, it can be seen that the best agreement with experiments is obtained with a slope of 0.2 for a current density of $300 \mu\text{A mm}^{-2}$ and a slope of 0.15 for a current density of $540 \mu\text{A mm}^{-2}$, where the larger current density outperforms the smaller one significantly. Finally, the smaller bottom radius results in a better agreement with experiment with respect to the width of the specimen.

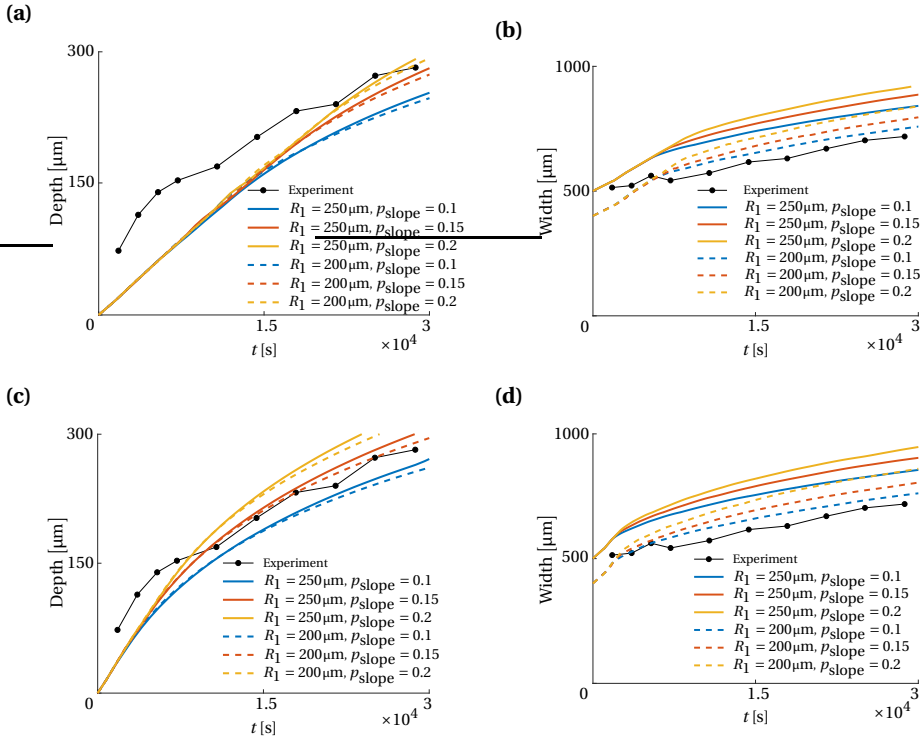


Figure 7: The (a) pit depth and (b) width for $i_a = 300 \mu\text{A mm}^{-2}$, and the (c) pit depth and (d) width for $i_a = 540 \mu\text{A mm}^{-2}$ for the no flow corrosion experiment.

6.2.2. Flow - with and without mechanical load

The experiments of corrosion pitting under fluid flow were done using a scanning droplet system [17]. The bottom and top radii are both equal to $250 \mu\text{m}$. Again, the quarter specimen shown in Fig. 6 is considered. Each current density has its own set of four different column heights h_c , which are chosen such that they result in a close agreement with the experimental data. The mechanical load is applied in the negative x direction at the plane AEHD. The plane BFGC is constrained in the x -direction, the plane ABCD in the y -direction and the node A in the z -direction. In these numerical examples, it is assumed that the fluid flow results in a continuous refreshment of the solution at the top of the column and is therefore modelled with a zero concentration boundary condition at the top. A potential improvement to the present model, and thus not included here, could be to add an extra step into the algorithm presented in Fig. 2, just before the diffusion problem block, in which the actual flow velocities inside the pit are computed [47].

For the mechanical stress-assisted experiments, a cyclic mechanical stress with a maximum value of 200 MPa , a load ratio of 0.1 (i.e. a minimum stress of 20 MPa) and loading frequency of 2 Hz was considered. The effect of loading frequency cannot be captured with the current implementation of the model as discussed in Section 2, because the

load and time increments are unrelated to improve computational efficiency. However, it should be noted that, because the cyclic load ratio is 0.1 and not for example -1, once the maximum applied load is reached at a given fixed pit depth, $\bar{\epsilon}_p$ remains constant irrespective of the amount of loading cycles because the equivalent plastic strain or back stress will not increase on the downward or upward branch. Consequently, the plasticity parameter introduced by the authors [28] will have the same value as $\bar{\epsilon}_p$. Therefore, \bar{p} from Eq. (5.5) could be set equal to $\bar{\epsilon}_p$ as was also done by Fatoba et al. [17]. The only frequency effect that is present in the experiments is the change in pit shape during a loading cycle. However, as the change in pit shape is negligible for a short time period, the error induced for jumping cycles or jumping in time should be minimal. This is emphasized by previous numerical analyses [28], where it was shown that there is no effect of loading frequency when there is no plasticity, which scenario is comparable to having a fixed amount of plasticity over a load cycle. In the numerical examples with an applied load, a fixed time increment of 30 seconds was used.

A comparison in terms of pit depth between the experiment and the numerical model for the loaded and non-loaded specimens for both current densities is presented in Fig. 8. Several relevant observations can be made. Firstly, the pit growth rate of the unloaded specimens is initially independent of the column height for a given current density. However, the height of the column does affect the transition point from activation to diffusion control. A smaller electrolyte column, keeping the zero boundary condition at the column top in mind, means that ions reach the top boundary faster and then leave the pit domain. Consequently, the specimens with a smaller initial electrolyte column reach complete diffusion control for a larger pit depth.

Secondly, for the numerical simulations the difference between the loaded and the non-loaded specimens is created in the initial phase of the pit growth process. This agrees well with the experiments. At this stage both setups are in activation control, which means the specimen exposed to a mechanical stress experiences an acceleration in pit growth rate. However, the loaded samples switch earlier to diffusion control than the ones without a load, which decreases the pit growth rate, reducing the final difference in pit depth between the loaded and the non-loaded cases. For the simulations with the mechanical loading, the column height hardly influences the point of this transition. The reason for this is that all loaded specimens experience plastic behaviour around the same point. As followed from Eq. (5.5), plastic strain strongly accelerates the pit growth rate, and forces the pit to go immediately into diffusion control. After this moment, as the pit is now completely in diffusion control, the mechanical load does no longer influence the corrosion speed. This emphasizes the validity of using cycle jumps for these examples, because the actual amount of plasticity does not matter, as the initial presence of it pushes the front at that location in diffusion control.

Thirdly, for the larger current density, the difference between the loaded and non-loaded simulation is smaller as compared to the smaller current density. The reason for this is that the larger current density pushes the whole pit into diffusion controlled corrosion much earlier than the smaller current density. Therefore, the mechanical load can only make a difference for a shorter period of time in the case of the larger current density.

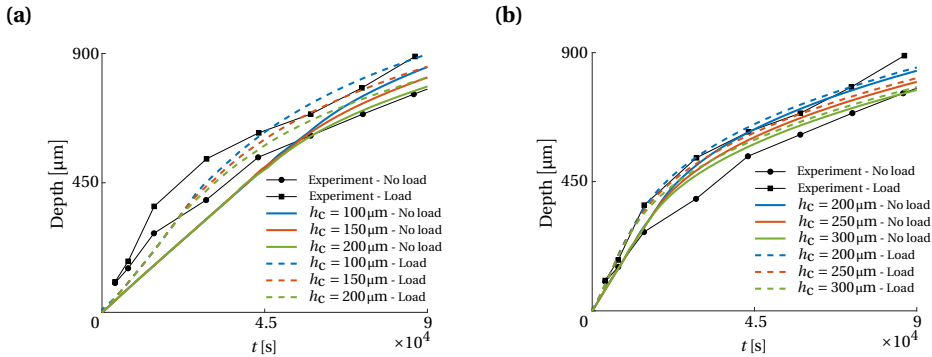


Figure 8: The pit depth with and without applied mechanical loading for (a) $i_a = 300 \mu\text{A mm}^{-2}$ and (b) $i_a = 540 \mu\text{A mm}^{-2}$.

Qualitatively, a good agreement between experiment and simulations is observed in terms of the shape of the curves and the effect of loading for both current densities. Quantitatively, it can be seen that using $540 \mu\text{A mm}^{-2}$ instead of $300 \mu\text{A mm}^{-2}$ results in a better agreement with both the loaded and non-loaded experiment. Particularly in the initial phase of the pit growth process the higher current density gives much better results. Although there is a reasonable agreement over the whole pit range when using a current density of $540 \mu\text{A mm}^{-2}$ and a height of $250 \mu\text{m}$, the difference between the numerical results of the loaded and non-loaded case for larger pit depths is significantly smaller in the simulation results than in the experimental observations.

The shape of the pit front and the concentration distribution for the loaded specimen with a column height equal to $250 \mu\text{m}$ at 20400 seconds under a current density of $540 \mu\text{A mm}^{-2}$ is shown Fig. 9. It can be seen that the whole pit front is constructed out of all the different elemental cross-sections. Furthermore, at this stage the pit is obviously completely in diffusion control, as the saturation concentration is reached along the whole pit front. The shape of the front at this stage is close to a quarter of a sphere and thus axisymmetric.

However, when investigating the shape of the pit at an earlier time, it can be seen that this is not the case. Figure 10 shows the pit depths map for the same specimen at 7200 and 20400 seconds. The maps also indicates by means of a read line a perfect quarter of a circle, which would be the shape in axisymmetric pit growth. It can be seen from the time point of 7200 seconds that initially the pit grows faster in the y -direction compared to the x -direction. Also, the depth of the pit is larger for a given y -coordinate compared to using the same value as x -coordinate. At this stage, a large section of the pit is still under activation control. On the other hand, as the pit front at 20400 is already completely under diffusion control, areas with larger spatial gradients are smoothed out, creating a shape that closely resembles axisymmetric pit growth.

The reason for the increased growth in the y -direction is caused by the stress distribution around the pit. The normal stress in the x -direction along the XZ and the YZ plane for the specimen at 7200 seconds is visualized in Fig. 11. The normal stress is largest around

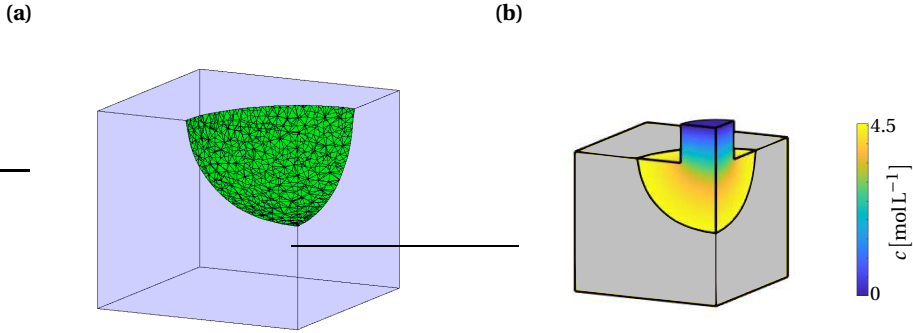


Figure 9: (a) The pit front shape and (b) the concentration distribution for a loaded specimen with a column height of $250\ \mu\text{m}$ at 20400 seconds under a current density of $540\ \mu\text{Amm}^{-2}$.

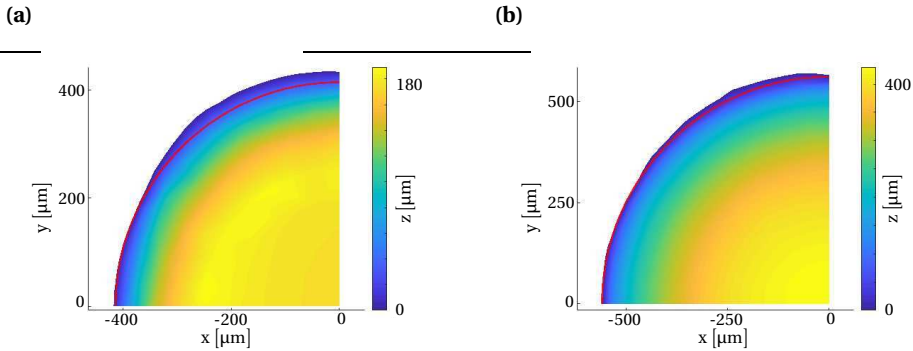


Figure 10: A pit depth map, excluding any mechanical deformation, at (a) 7200 and (b) 20400 seconds of the loaded specimen with a column height of $250\ \mu\text{m}$ under a current density of $540\ \mu\text{Amm}^{-2}$. The red line indicates a perfect quarter of a circle.

the outer edge of the pit in the YZ plane because the load is applied perpendicular to this plane. In the XZ plane, the maximum normal stress is only reached at the small bump at the bottom of the pit. Keeping Eq. (5.5) in mind, it is obvious that the pit grows fastest in the y -direction. Furthermore, the small bump is located on the side of the pit bottom because stress concentrations are largest near corners. These rounded corners are formed due to the initial flat disk shape of the pit, followed by an initial constant growth rate for the whole pit front.

At 20400 second the specimen is under diffusion control and therefore the pit growth rate no longer depends on the applied loading. However, as can be seen from Fig. 11, the normal stress is still largest on the YZ plane, and because the flat bottom has been transformed to that of an axisymmetric pit due to diffusion, the area of maximum stress has increased, creating more potential sites for the formation of cracks.

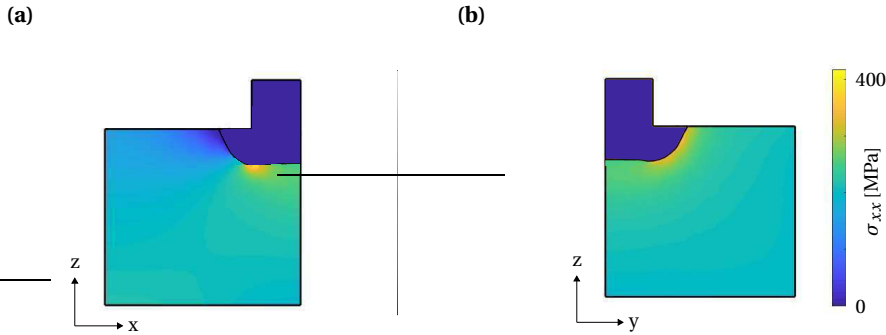


Figure 11: (a) The normal stress in the x-direction at the (a) XZ plane and (b) the YZ plane for a loaded specimen at maximum applied stress with a column height of $250\ \mu\text{m}$ at 7200 seconds under a current density of $540\ \mu\text{Amm}^{-2}$.

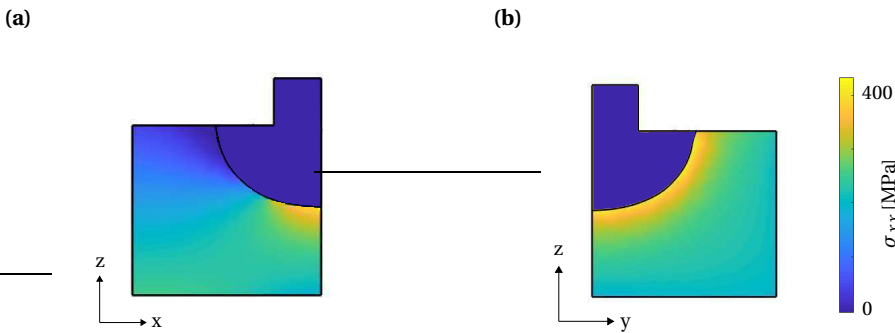


Figure 12: (a) The normal stress in the x-direction at the (a) XZ plane and (b) the YZ plane for a loaded specimen at maximum applied stress with a column height of $250\ \mu\text{m}$ at 20400 seconds under a current density of $540\ \mu\text{Amm}^{-2}$.

7. Conclusions

This study presents an extension to 3D of the pitting corrosion model developed by the authors in [28], where a level set model was combined with the finite element method to implicitly track the corrosion front that divides the domain in a pit domain and a solid domain. The extension was natural because of the use of field equations for the level set reinitialization and velocity extension. The only change the 3D process requires is a modification of the triangulation process to tetrahedron partitioning. Furthermore, a cycle jump approach has been added to improve the computational efficiency.

The diffusion of metal ions, coming from the anodic dissolution process occurring at the corrosion pit front, is solved in the pit domain. The relation between the velocity of this front and the dissolution flux is governed by the Rankine-Hugoniot front condition. This front condition acts as a mixed boundary condition in activation control where the front velocity is known *a priori*. Under diffusion control, the front condition is used to compute the velocity of the front afterwards. In the solid domain the strains and stresses are

computed using the static equilibrium equation. This accelerates the corrosion speed in the activation controlled regime following the Gutman equations.

The model is verified for a 1D pit growth setting and is compared against a set of three 3D experiments, which resulted in a reasonable agreement. The mechanical load delivered the expected increase in pit growth rate. However, there is a discrepancy between the experiment and the numerical model during the later stages of pit growth. In the experiment the difference between loaded and non-loaded specimens remains relatively constant. However, in the numerical model this difference decreases as both samples are under full diffusion control, in which there is no influence of the mechanical load on the pit growth rate. As the experiments had some unknown parameters, a sensitivity study was performed. It was shown that the height of the electrolyte column does not affect the transition point from activation to diffusion control at the bottom of the pit. This is caused by the big acceleration in corrosion speed created by plastic strain.

The difference in pit growth rate between a loaded and a non-loaded pit is made in the initial stage of the pit when it is still under activation control. Furthermore, the applied loading does not only accelerate the pit growth, but also pushes it to diffusion control in an earlier stage compared to a non-loaded pit. As a result, the difference in pit depth between both cases reduces until the corrosion regime of the whole pit front of the non-loaded specimen also turns into diffusion control. Although, the difference in transition point between loaded and non-loaded specimens is larger for smaller current densities, it turned out that they result into a larger difference in pit depth because it allows the mechanical load to influence the pit growth rate for a longer time before turning the regime into diffusion control.

Finally, note that the first 3D pit growth numerical example without flow could technically be modelled with an axisymmetric diffusion model. The same holds for the flow example without load, because of the mentioned flow assumption. However, an axisymmetric model can definitely not be used in the case of pit growth under mechanical stress, if the applied loading is axial. Such an applied loading causes the pit to deviate from its axisymmetric form by promoting increased pit growth on the plane perpendicular to the applied loading. However, once the pit front is fully under diffusion control, it will grow towards an axisymmetric shape. This means that the shape of a corrosion under mechanical stress can give an indication of the current corrosion regime.

It is envisioned that the proposed model can be used to further improve the understanding of mechanically-assisted corrosion fatigue and enhance the ability to make reliable predictions of the rate at which pitting corrosion develops under various conditions. Improved predictive ability can help in optimizing the design of offshore structures and in developing efficient inspection and maintenance schedules.

Acknowledgements

This research is part of the EUROS program, which is supported by NWO domain Applied and Engineering Sciences and partly funded by the Dutch Ministry of Economic Affairs.

Data Availability Statement

The data that support the findings of this study are available from the corresponding author upon reasonable request.

References

- [1] W. Khodabux, C. Liao, and F. Brennan, *Characterisation of pitting corrosion for inner section of offshore wind foundation using laser scanning*, *Ocean Engineering* **230**, 109079 (2021).
- [2] J. Bhandari, F. Khan, R. Abbassi, V. Garaniya, and R. Ojeda, *Modelling of pitting corrosion in marine and offshore steel structures – a technical review*, *Journal of Loss Prevention in the Process Industries* **37**, 39–62 (2015).
- [3] E. Shekari, F. Khan, and S. Ahmed, *Economic risk analysis of pitting corrosion in process facilities*, *International Journal of Pressure Vessels and Piping* **157**, 51 (2017).
- [4] W. Mai, S. Soghrati, and R. Buchheit, *A phase field model for simulating the pitting corrosion*, *Corrosion Science* **110**, 157 (2016).
- [5] W. Mai and S. Soghrati, *A phase field model for simulating the stress corrosion cracking initiated from pits*, *Corrosion Science* **125**, 87 (2017).
- [6] W. Mai and S. Soghrati, *New phase field model for simulating galvanic and pitting corrosion processes*, *Electrochimica Acta* **260**, 290 (2018).
- [7] T. Ansari, Z. Xiao, S. Hu, Y. Li, J. Luo, and S. Shi, *Phase-field model of pitting corrosion kinetics in metallic materials*, *npj Computational Materials* **4**, 38 (2018).
- [8] A. F. Chadwick, J. A. Stewart, R. A. Enrique, S. Du, and K. Thornton, *Numerical modeling of localized corrosion using phase-field and smoothed boundary methods*, *Journal of The Electrochemical Society* **165**, C633 (2018).
- [9] N. Laycock and R. Newman, *Temperature dependence of pitting potentials for austenitic stainless steels above their critical pitting temperature*, *Corrosion Science* **40**, 887 (1998).
- [10] N. Laycock and S. White, *Computer simulation of single pit propagation in stainless steel under potentiostatic control*, *Journal of the Electrochemical Society* **148**, B264 (2001).
- [11] S. Sarkar, J. E. Warner, and W. Aquino, *A numerical framework for the modeling of corrosive dissolution*, *Corrosion Science* **65**, 502 (2012).
- [12] S. Scheiner and C. Hellmich, *Stable pitting corrosion of stainless steel as diffusion-controlled dissolution process with a sharp moving electrode boundary*, *Corrosion Science* **49**, 319 (2007).
- [13] S. Scheiner and C. Hellmich, *Finite volume model for diffusion- and activation-controlled pitting corrosion of stainless steel*, *Computer Methods in Applied Mechanics and Engineering* **198**, 2898 (2009).
- [14] R. Duddu, *Numerical modeling of corrosion pit propagation using the combined extended finite element and level set method*, *Computational Mechanics* **54**, 613 (2014).

- [15] A. S. Vagbharathi and S. Gopalakrishnan, *An extended finite-element model coupled with level set method for analysis of growth of corrosion pits in metallic structures*, Proceedings of the Royal Society A: Mathematical, Physical and Engineering Sciences **470** (2014), 10.1098/rspa.2014.0001.
- [16] H. Wang and E. Han, *Simulation of metastable corrosion pit development under mechanical stress*, Electrochimica Acta **90**, 128 (2013).
- [17] O. Fatoba, R. Leiva-Garcia, S. Lishchuk, N. Larrosa, and R. Akid, *Simulation of stress-assisted localised corrosion using a cellular automaton finite element approach*, Corrosion Science **137**, 83 (2018).
- [18] D. De Meo and E. Oterkus, *Finite element implementation of a peridynamic pitting corrosion damage model*, Ocean Engineering **135**, 76 (2017).
- [19] S. Jafarzadeh, Z. Chen, S. Li, and F. Bobaru, *A peridynamic mechano-chemical damage model for stress-assisted corrosion*, Electrochimica Acta **323**, 134795 (2019).
- [20] C. Tsuyuki and Y. Yama Akinori, A. and Ogimoto, *Phase-field modeling for pH-dependent general and pitting corrosion of iron*, Scientific Reports **8**, 12777 (2018).
- [21] C. Lin, H. Ruan, and S. Shi, *Phase field study of mechanico-electrochemical corrosion*, Electrochimica Acta **310**, 240 (2019).
- [22] Z. Chen and F. Bobaru, *Peridynamic modeling of pitting corrosion damage*, Journal of the Mechanics and Physics of Solids **78**, 352 (2015).
- [23] S. Jafarzadeh, Z. Chen, J. Zhao, and F. Bobaru, *Pitting, lacy covers, and pit merger in stainless steel: 3D peridynamic models*, Corrosion Science **150**, 17 (2019).
- [24] S. Rokkam, M. Gunzburger, M. Brothers, N. Phan, and K. Goel, *A nonlocal peridynamics modeling approach for corrosion damage and crack propagation*, Theoretical and Applied Fracture Mechanics **101**, 373 (2019).
- [25] Z. Chen, S. Jafarzadeh, J. Zhao, and F. Bobaru, *A coupled mechano-chemical peridynamic model for pit-to-crack transition in stress-corrosion cracking*, Journal of the Mechanics and Physics of Solids **146**, 104203 (2021).
- [26] P. Van der Weeen, A. M. Zimer, E. C. Pereira, L. H. Mascaro, O. M. Bruno, and B. De Baets, *Modeling pitting corrosion by means of a 3D discrete stochastic model*, Corrosion Science **82**, 133 (2014).
- [27] C. Cui, R. Ma, A. Chen, Z. Pan, and H. Tian, *Experimental study and 3D cellular automata simulation of corrosion pits on Q345 steel surface under salt-spray environment*, Corrosion Science **154**, 80 (2019).
- [28] R. Dekker, F. P. van der Meer, J. Maljaars, and L. J. Sluys, *A level set model for stress-dependent corrosion pit propagation*, International Journal for Numerical Methods in Engineering **122**, 2057 (2021), <https://onlinelibrary.wiley.com/doi/pdf/10.1002/nme.6614> .

- [29] E. M. Gutman, *Mechanochemistry of materials* (Cambridge Int Science Publishing, 1998).
- [30] S. Sharland, C. Jackson, and A. Diver, *A finite-element model of the propagation of corrosion crevices and pits*, *Corrosion Science* **29**, 1149 (1989).
- [31] S. Sarkar and W. Aquino, *Electroneutrality and ionic interactions in the modeling of mass transport in dilute electrochemical systems*, *Electrochimica Acta* **56**, 8969 (2011).
- [32] X. Sun and R. Duddu, *A sequential non-iterative approach for modeling multi-ionic species reactive transport during localized corrosion*, *Finite Elements in Analysis and Design* **166**, 103318 (2019).
- [33] S. Sharland and P. Tasker, *A mathematical model of crevice and pitting corrosion - I. the physical model*, *Corrosion Science* **28**, 603 (1988).
- [34] M. Mainguy and O. Coussy, *Propagation fronts during calcium leaching and chloride penetration*, *Journal of Engineering Mechanics* **126**, 250 (2000).
- [35] M. Hautefeuille, C. Annavarapu, and J. Dolbow, *Robust imposition of dirichlet boundary conditions on embedded surfaces*, *International Journal for Numerical Methods in Engineering* **90**, 40 (2012).
- [36] G. Wells and L. Sluys, *A new method for modelling cohesive cracks using finite elements*, *International Journal for Numerical Methods in Engineering* **50**, 2667 (2001).
- [37] R. Dekker, F. van der Meer, J. Maljaars, and L. Sluys, *A cohesive XFEM model for simulating fatigue crack growth under mixed-mode loading and overloading*, *International Journal for Numerical Methods in Engineering* **118**, 561 (2019), <https://onlinelibrary.wiley.com/doi/pdf/10.1002/nme.6026> .
- [38] A. Khoei, *Extended finite element method: Theory and applications*, *Extended Finite Element Method: Theory and Applications* , 1 (2015).
- [39] J. Chaboche, *Constitutive equations for cyclic plasticity and cyclic viscoplasticity*, *International Journal of Plasticity* **5**, 247 (1989).
- [40] J. Chaboche, *On some modifications of kinematic hardening to improve the description of ratchetting effects*, *International Journal of Plasticity* **7**, 661 (1991).
- [41] T. Adams, S. Giani, and W. M. Coombs, *A high-order elliptic pde based level set reinitialisation method using a discontinuous galerkin discretisation*, *Journal of Computational Physics* **379**, 373 (2019).
- [42] J. A. Sethian, *Level set methods and fast marching methods: evolving interfaces in computational geometry, fluid mechanics, computer vision, and materials science* (Cambridge university press, 1999).
- [43] G. T. Gaudet, W. T. Mo, T. A. Hatton, J. W. Tester, J. Tilly, H. S. Isaacs, and R. C. Newman, *Mass transfer and electrochemical kinetic interactions in localized pitting corrosion*, *AIChE Journal* **32**, 949 (1986).

-
- [44] J. C. R. Pereira, A. M. P. de Jesus, A. A. Fernandes, and G. Varelis, *Monotonic, low-cycle fatigue, and ultralow-cycle fatigue behaviors of the X52, X60, and X65 piping steel grades*, Journal of Pressure Vessel Technology **138** (2016), 10.1115/1.4032277, 031403, https://asmedigitalcollection.asme.org/pressurevesseltech/article-pdf/138/3/031403/6319004/pvt_138_03_031403.pdf .
- [45] E.-S. M. Sherif, A. A. Almajid, K. A. Khalil, H. Junaedi, and F. Latief, *Electrochemical studies on the corrosion behavior of API X65 pipeline steel in chloride solutions*, International Journal Electrochemical Science **8**, 9360 (2013).
- [46] X. Wang, X. Tang, L. Wang, C. Wang, and W. Zhou, *Synergistic effect of stray current and stress on corrosion of API X65 steel*, Journal of Natural Gas Science and Engineering **21**, 474 (2014).
- [47] J. N. Harb and R. C. Alkire, *Transport and reaction during pitting corrosion of ni in 0.5m NaCl: II . flowing fluid*, Journal of The Electrochemical Society **138**, 3568 (1991).

6

Conclusions

The objective of this thesis was to develop numerical models that can accurately capture the physics related to two different damage processes. For the first damage process, crack growth under cyclic loading, it is important that the plastic deformation occurring around the crack tip is captured correctly as it plays a major role in properly modelling crack growth under an overload and out-of-phase mixed mode loading. Furthermore, the numerical method should be applicable even when the crack path is not known *a priori*. The second damage process that was considered is stress-assisted pitting corrosion. Here, the numerical model should be able to capture the effect of mechanical stress on the pit growth rate. Furthermore, the effect of different loading and corrosion conditions on the pit growth rate and the pit shape development should be studied as well. What follows next is a chapter-wise summary of the developed numerical models, and their corresponding results and conclusions.

In **Chapter 2** a new approach for fatigue crack propagation in ductile materials was presented. It relies on the separation between plasticity around the crack tip and fatigue crack growth at the crack tip such that the influence of plasticity on fatigue driving forces is predicted. The approach is built in a phantom-node framework enabling arbitrary crack growth direction. Furthermore, adaptive meshing using a quad-tree algorithm is applied to keep the simulations efficient. The fracture process zone ahead of the physical crack tip is modelled by means of cohesive tractions. Consequently, the numerical model keeps track of two different crack tips, being the physical crack tip and the fictitious or numerical crack tip. These two crack tips propagate according to different criteria. As a result, the size of the fracture process zone follow automatically from the simulation.

Two different models were used to compute the tractions in the fracture process zone, being a cohesive zone model and an interfacial thick level set model. The difference between the two is that for the cohesive zone model the damage follows from a given traction-separation law, while for the interfacial thick level set the damage profile over the fracture process zone is pre-defined. The two models result in different traction distributions over the FPZ and therefore, in the case of an elastic-plastic material, also a different distribution of plasticity. Consequently, the SIFs for the two models are not the same for a given crack length and both models require a different set of Paris parameters. Furthermore, it was observed that it is not straightforward to control the maximum cohesive traction, and thus the amount of plasticity, for the ITLS method.

Both models showed good agreement with a mode I analytical relation and a mixed-mode experiment. Furthermore, it was shown that the presented models can also capture the crack retardation phenomenon due to an overload when the J-integral is employed for the ERR extraction. However, extracting the ERR from the traction-separation law at the physical crack tip for the cohesive zone model only gives correct results in the case of constant amplitude loading, irrespective of using an elastic or an elastic-plastic material.

Chapter 3 discussed a calibration method for the cohesive XFEM model, presented in the previous chapter, in which a traction-separation law was used to compute the cohesive tractions. It was shown that the cohesive stiffness does not influence the energy

release rate for a given crack length. Also, the critical energy release does not influence the fatigue behaviour and is only important to define the transition to quasi-static crack growth. In total three parameters require calibration: the Paris constant, the Paris exponent and the tensile strength. An increase in the tensile strength results in a lower energy release rate for a given crack length due to an increased amount of plasticity in the bulk material around the fracture process zone. For each tensile strength value, the plastic Paris parameters can be calibrated to a constant amplitude cyclic loading test. After that, the correct set of tensile strength and Paris parameters was chosen such that it can correctly capture crack retardation in an overload experiment.

The calibrated parameters were subsequently used for in-phase and out-of-phase biaxial loading problems on a steel cruciform specimen, from which the experimental data originate from a different source in literature. In terms of crack path, in which the Paris parameters do not play a role, there was a good agreement with experiment for in-phase loading and 90° out-of-phase loading. However, the numerical model showed a deviation from the crack path in the experiment for 45° out-of-phase loading. Recalibrating the Paris constant, such that the numerical model agreed with the experiment for in-phase biaxial loading, resulted in a good agreement for 90° out-of-phase biaxial loading and biaxial loading with a single overload for experiments on the same geometry. It was not necessary to recalibrate the strength parameter to accurately reproduce the retardation observed in the experiment.

The importance of including plasticity in the bulk material for accurately capturing fatigue crack growth was illustrated with numerical results obtained with the same cohesive zone model but then embedded in a linear elastic bulk material. With the elastic bulk material no crack retardation after overloading is obtained. Moreover, parameters resulting in a good agreement with the experiment for in-phase biaxial loading did not result in a good agreement in out-of-phase biaxial loading. This means that including elastic-plastic material behaviour is essential when numerically investigating fatigue crack growth under load conditions that deviate from simple constant amplitude mode I cases.

In **Chapter 4** a 2D numerical model for corrosion pit propagation under mechanical loading was presented. It uses the level set method to track the pit front and to split the domain into a solid domain and a pit domain. Level set reinitialization as well as the velocity extension was performed using field equations, which enables the model to be extended for the use of different mesh types and also 3D analyses.

In the pit domain the diffusion of the concentration of atoms, which originate from the dissolution process occurring at the pit front, is simulated. The equilibrium between the propagation velocity of the pit front and the flux through dissolution is defined by the Rankine-Hugoniot front condition. The implementation of the front conditions depends on the regime of corrosion, which can be activation control, diffusion control or passivation. All three regimes are required in order to simulate the formation of a lacy cover.

In the solid domain static equilibrium is solved to obtain the strains and stresses. Because the equivalent plastic strain grows indefinitely under cyclic loading, which is physically unrealistic, a new parameter called the equivalent dislocation strain was introduced, which depends on the signs of the plastic strain increment and the back stress, was introduced. The new state variable shows a better match with theoretical understanding of how dislocation pile-ups evolve under cyclic loading. However, it still needs to be validated quantitatively.

According to the implemented model, a combination of activation control and an elastic material response, results in faster pit propagation under constant loading than under cyclic loading given the same maximum load. However, in the presence of plastic deformation, cyclic loading can significantly increase the pit growth rate. Furthermore, increasing the cyclic load frequency results in faster pit propagation as there are more cycles to build up plastic strain to kinematic hardening before the material is dissolved into the pit. In the case of diffusion control, mechanical loading does not influence the pit growth rate, provided that the salt layer leading to diffusion control remains intact.

In **Chapter 5** the pitting corrosion model is extended to three dimensions. The extension was natural because of the use of field equations for the level set reinitialization and velocity extension. The numerical model is compared against 3D pitting experiments with and without mechanical cyclic loading in which also a sensitivity study was performed because of the absence of some crucial input parameters.

The difference in pit growth rate between a loaded and a non-loaded pit is made in the initial stage of the pit when it is still under activation control. Furthermore, the applied loading does not only accelerate pit growth, but also pushes it to diffusion control earlier compared to a non-loaded pit. As a result, the difference in pit depth between both cases reduces until the corrosion front regime of the non-loaded specimen also turns to complete diffusion control. Although, the difference in transition point between loaded and non-loaded specimens is larger for smaller current densities, it turned out that they result in larger difference in pit depth because it allows the mechanical load to longer influence the pit growth rate before turning the regime to diffusion control.

Finally, it was found that under applied mechanical loading the pit starts to deviate from its axisymmetric form by promoting increased pit growth on the plane perpendicular to the load. However, once the pit front is fully under diffusion control, it will grow back to its axisymmetric shape.

1. Outlook

This thesis treated the two topics, fatigue crack growth and stress-assisted pitting corrosion as separate mechanisms. However, in reality, pitting corrosion creates stress concentration sites from which fatigue cracks may grow. Therefore, it is recommended to combine both models, such that the whole spectrum from the creation of a pit to final failure can be captured. A couple of steps are required in order to reach that point.

As a first step, the 2D fatigue crack growth model from Chapters 2 and 3 should be extended to 3D. Possibly a double level set approach could be implemented, in which the outward front is defined as the numerical front and the inward level set front as the physical one. The tractions present in the fracture process zone can be computed using a mixed-mode cohesive law that includes all three modes of fracture, namely opening, in-plane shear and out-of-plane shear. The numerical front could move again according to a critical stress criterion in the direction perpendicular to the maximum principle stress. The physical front could propagate according to a crack growth relation based on fracture mechanics, in which a method has to be defined in order to extract the appropriate energy release rate from the cohesive zone.

In order to connect the pitting corrosion model with the fatigue crack growth model an extra ingredient has to be included, namely the fatigue initiation step. This step should indicate where and when the fatigue macro crack starts. The fatigue initiation model is then competing with the pitting model in the sense that fatigue damaged material might be removed due to corrosion. However, at some point fatigue initiation damage will outrun the corrosion damage.

Next, the double level set model for 3D simulation can be used to combine pitting corrosion, fatigue initiation and crack propagation. Fatigue initiation damage is stored at the bulk integration points. The physical front moves forward due to anodic dissolution and, at locations where the fatigue initiation period has been exceeded, according to the Paris law. The speed of front is equal to the maximum of the two damage processes. The numerical front only moves forward due to the presence of a critical stress. In the absence of load or in the case of more intense growth due to pitting corrosion, the physical front simply pushes the numerical front along. One of the main challenges would be related to defining the pit domain, such that the opening volume created by a crack is included.

Finally, a couple of extensions could be added to the staggered approach presented in Chapters 4 and 5. Firstly, other species than just the main metal ions could be included in the corrosion problem, which means that also the cathodic reaction could be captured. Secondly, the staggered approach could be extended with a fluid flow model to compute the flow velocities inside the pit. Thirdly, as discussed in the introduction of this thesis, wind turbine structural elements are often built by means of welding, which causes a heat affected zone around the weld. The material properties of this zone are different from the base material. An extra initialization step in which the welding process is simulated could be added to potentially determine the residual stresses created by the joining process. The simulation could potentially also predict the creation of initial defects for which welds are notorious.

As a final note it would be beneficial for the whole community if bench mark tests would be performed for pitting corrosion with and without mechanical loads. Similar to Chapter 4, the load should either be a constant stress or a fatigue load, which then also could lead to stress corrosion crack and fatigue crack growth. The tests should be performed for several time stamps and they should cover a variety in corrosion and loading conditions. The data for each time stamp should consist of pit properties such as depth, width

and shape, the size of any possible fatigue cracks, and measurements that can indicate the severity of the fatigue initiation damage. Regarding the pit growth rate, it would be interesting to see if the loading frequencies effects shown in Chapter 4 also occur in real-life experiments.